Near and Mid-Infrared Observations of the Galactic Center
On the Nature of Diffuse Emission and Faint Compact Sources

INAUGURAL-DISSERTATION

zur
Erlangung des Doktorgrades
der Mathematisch-Naturwissenschaftlichen Fakultät
der Universität zu Köln

vorgelegt von

Nadeen Bassam Izzat Sabha
aus Amman, Jordanien

Köln, 2015

2

Berichterstatter: Prof. Dr. Andreas Eckart
                                               Prof. Dr. Peter Schneider

Tag der letzten mündlichen Prüfung: 5. Dezember 2014

ABSTRACT

The center of our Galaxy is made up of stars, stellar remnants, dust, molecular and ionized gas, with a supermassive black hole at its heart. This black hole is surrounded by a small cluster of high velocity stars, known as the S-stars. One aim of this thesis is to constrain the amount and nature of the stellar and dark mass associated with this cluster in the immediate vicinity of the black hole. I use near-infrared imaging to determine the K_s-band luminosity function of the S-star cluster members, and the distribution of the diffuse background emission and the stellar number density counts around the central black hole. This allows one to determine the stellar light and mass contribution expected from the faint members of the cluster. I then use post-Newtonian N-body techniques to investigate the effect of stellar perturbations on the motion of S2, as a means of detecting the number and masses of the perturbers. I find that the stellar mass derived from the K_s-band luminosity extrapolation is much smaller than the amount of mass that might be present considering the uncertainties in the orbital motion of the star S2. Also the amount of light from the fainter S-cluster members is below the amount of residual light at the position of the S-star cluster after removing the bright cluster members. If the distribution of stars and stellar remnants is peaked near the supermassive black hole, observed changes in the orbital elements of S2 can be used to constrain both their masses and numbers. Based on simulations of the cluster of high velocity stars, I find that at a wavelength of 2.2 μm, close to the confusion level for 8 m class telescopes, blend stars will occur. These line-of-sight clusterings will last for typically three years before they dissolve due to proper motions.

I also present the analysis of mid-infrared VISIR observations. Their field of views are centered on the major Galactic Center targets that we plan to observe with the MIRI instrument aboard the James Webb Space Telescope (JWST). The value of these new observations lies in the fact that they are the first and only data that cover a large field of view of the region with spatial resolutions better than Spitzer survey data. The spectral indices of the compact sources detected in our multi-band observations will aid in the identification of massive young stellar objects, and will allow the tracing of their spatial distribution and concentration. When combined with the current multi-wavelength surveys and future MIRI observations it will enable us to trace and draw a better picture of the past 8 Myr of cluster based star formation in the Galactic Center. Furthermore, I report

a curious convex-like mid-infrared feature at a distance of 0.68 pc (17″) from the position of the supermassive black hole. This feature resembles a stellar bow shock with a symmetry axis pointing toward the Center. I discuss the possible nature of this feature and the implications of its alignment with other dusty comet-like objects previously found inside the central parsec. All of these objects are remarkably aligned perpendicular to the plane of young mass-losing stars very close to the central SMBH. The lack of a larger number of similar objects in the field can be explained either by the short life span of massive stars and/or the intermittent nature of the responsible mechanism.

ZUSAMMENFASSUNG

Das Zentrum unserer Galaxie setzt sich aus Sternen, Sternüberresten, Staub, molekularem und ionisiertem Gas zusammen. In deren Mitte befindet sich ein supermassives schwarzes Loch. Dieses supermassive schwarze Loch ist unmittelbar von einer kleinen Anhäufung von Sternen mit hohen Geschwindigkeiten umgeben, den sogenannten S-Sternen. Der erste Teil dieser Arbeit ist es die stellare und die dunkle (nicht sichtbare) Masse dieses Haufens und ihre Eigenschaften näher zu bestimmen. Anhand von Nahinfrarotaufnahmen ermittele ich die K_s-Band Leuchtkraftfunktion der S-Sternhaufen Sterne, die Verteilung der diffusen Hintergrundemission und die Sternanzahldichte in der Umgebung des supermassiven schwarzen Lochs. Auf diese Weise kann man den Beitrag der lichtschwächeren Sterne zur Gesamtleuchtkraft und -masse abschätzen. Darüber hinaus untersuche ich mit Hilfe von post-Newtonschen N-Teilchen Simulationen die Störung der Bahnbewegung von Stern S2 durch andere S-Sterne, um die Anzahl und Masse der störenden Sterne zu bestimmen. Hierbei stelle ich fest, dass die stellare Masse basierend auf der Extrapolation der K_s-Band Leuchtkraft wesentlich kleiner ist als die Abweichungen der Bahnbewegung von S2 andeuten. Außerdem ist die Lichtmenge der lichtschwächeren S-Sterne geringer als die Restlichtmenge an der Stelle des S-Sternhaufens nach Abzug aller hellen S-Sterne. Unter der Annahme, dass die Verteilung der Sterne und Sternäberreste ihr Maximum in der Nähe des supermassiven schwarzen Lochs erreicht, kann man die Massen und die Anzahl der (störenden) Sterne anhand der beobachten Änderungen der Bahnparameter von S2 abschätzen. Meine Simulationen des Hochgeschwindigkeitssternhaufens zeigen, dass bei Beobachtungen bei einer Wellenlänge von 2.2 μm und nahe an der Konfusionsgrenze für Teleskope der 8 m-Klasse einzelne Sterne sich überdecken können. Diese Anhäufungen entlang der Sichtlinie hält für gewöhnlich 3 Jahre an bevor sie sich auf Grund ihrer Eigenbewegung der Sterne wieder auflösen.

Der zweite Teil meiner Arbeit behandelt die Analyse von Aufnahmen im mittleren Infrarot mit VISIR von Hauptbeobachtungsobjekten im Galaktischen Zentrum, die wir auch mit dem MIRI Instrument an Bord des JWST zu beobachten beabsichtigen. Diese Beobachtungen decken als erste und einzige ein großes Gesichtsfeld dieser Region mit einer höheren räumlichen Auflösung als die Spitzer Studie ab. Der Spektralindex der in unseren Multi-Band-Aufnahmen detektieren Punktquellen hilft bei der Identifizierung von massi-

ven jungen stellaren Objekten und derer räumlichen Verteilung und Anhäufung. Die Kombination von aktuellen Multi-Wellenlängen-Studien und zukünftigen MIRI Beobachtungen wird uns ein tieferes Verständnis der Sternentstehung der letzten 8 Millionen Jahren in Sternhaufen im Galaktischen Zentrum in ermöglichen.

Im Zuge meiner Analyse der Daten im mittleren Infrarot fiel mir eine ungewöhnliche, konvex-förmige Struktur in einer Entfernung von 0.68 pc (17") von der Position des supermassiven schwarzen Lochs auf. Diese Struktur ähnelt einer Bugstoßwelle eines Sterns und ihre Symmetrieachse weist in Richtung des supermassiven schwarzen Lochs im Zentrum. Ich erläutere die mögliche Natur dieser Erscheinung und die Bedeutung ihrer Orientierung in Bezug auf andere staubige, kometenartig geformte Objekte, die im zentralen Parsec bereits gefunden wurden. Bemerkenswerterweise zeigen all diese Objekte nahezu senkrecht auf die scheibenhafte Ansammlung junger, Masse-verlierender Sterne direkt um das supermassive schwarze Loch. Die geringe Zahl ähnlicher Objekte in dem Gebiet lässt sich durch die kurze Lebensspanne massiver Sterne und/oder das sporadische Auftreten des verantwortlichen Mechanismus erklären.

CONTENTS

1

GENERAL INTRODUCTION

In early September, 2014, Nature published an article that adds another detail to our understanding of our place in the Universe. Tully et al. (2014) study the distances and velocities of about 8000 galaxies. By removing the effect of cosmic expansion on these galaxies, they were able to derive a quantity called peculiar velocity that reflects gravitational perturbations. The resulting map showed that our galaxy the Milky Way (MW) is part of a supercluster they call "Laniakea", of which all the galaxies are moving inward within its boundary. Our location is in the outskirts of this supercluster close to another one called "Perseus-Pisces". Their findings shed light on the reason why our galaxy is moving at a rate of 600 km s^{-1} towards the constellation of Centaurus (Dressler et al., 1987).

Not only are we located in the outskirts of the local supercluster, but we are also in the outskirts of the Milky Way, a fact that makes studying the plethora of activity in the Galactic Center all the more difficult. I will begin this dissertation by giving an overview of our Galaxy and the Galactic Center environment, and follow this up with a brief description of the infrared observational techniques I utilize to study the Galactic Center, the subject of this thesis.

1.1   The Milky Way

The Milky Way is a barred spiral galaxy that harbors about 300 billion stars and has a diameter of ∼ 100 000 light years (see Fig. 1.1). It is viewed across the night sky as a faint band of light entwined with dark lanes. It is this grand appearance that inspired the name,
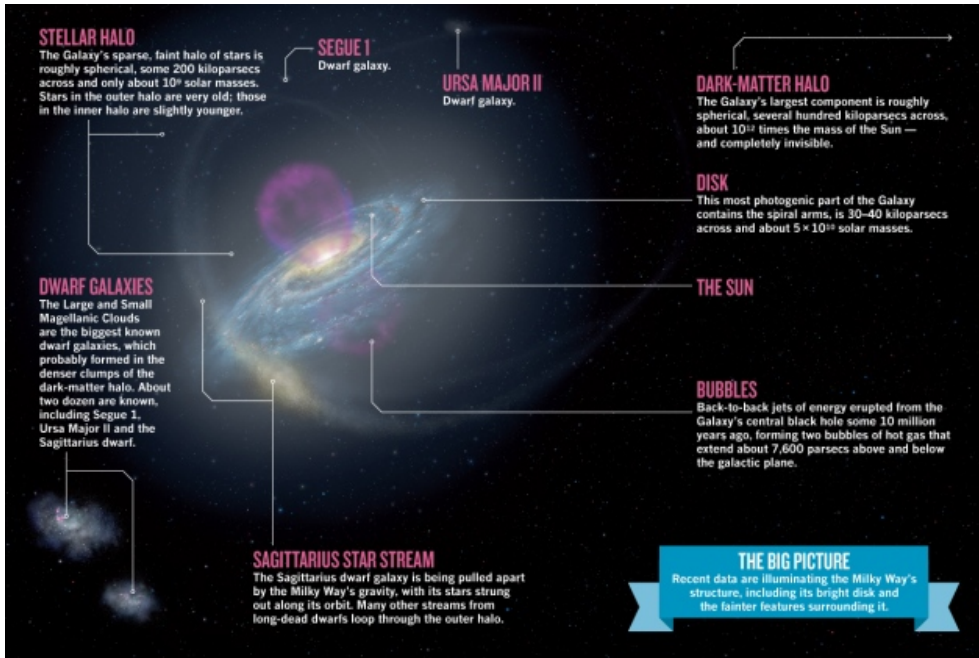
Figure 1.1: *Illustration of the Milky Way and its surroundings. Image credit:* Finkbeiner (2012) *Nature news feature.*

the Milky Way, since our ancestors variously described it as a river, as a path, as milk. In Arabic, it is called "Darb el-Ttabbanah" or "Darb el-Llabbaneh" which translates to either literally the Milky Way, or the Hay Way. The Hay Way comes from the similarities ancient Arabs noticed between fallen hay and the way the band appears in the sky. This band of light is our Galaxy seen edge-on due to the presence of our Solar System in one of the outer arms of the Galaxy.

Besides the considerable number of stars, the MW also contains nebulae, gas clouds, dust lanes and dark clouds. Like any other galaxy, a dark matter halo surrounds our own where astronomers inferred its existence since the 1970s through the gravitational influence it has on the rotation of the Galaxy. This halo has a spherical shape and a mass of about 1 trillion Suns and extends hundreds of thousands of light years or in another unit, hundreds of kiloparsecs, where 1 kpc ~ 3200 light year. There are also sub-halos of dark matter within the larger one. In addition to the dark matter, there are about two dozen dwarf galaxies that are believed to have been formed as a result of those dark-matter sub-halos pulling in gas which then form stars. Getting closer to the Galaxy itself, observations revealed the existence of faint streamers of stars that seem to trace the orbits of the dwarf galaxies as they were crossing the newly-formed Milky Way. One such streamer is illustrated in Fig.1.1. Surrounding the disk of the MW (up to about 100 kpc) a faint, diffuse

halo of stars can be seen. It has a mass of roughly 10^9 solar masses. Heavy element analysis shows that those stars located furthest from the MW are of older age than those closer to it. In fact, evidence points to there being two distinct halos where the outer one rotates against the Galaxy's rotation while the younger inner one rotates in the same direction (Carollo *et al.*, 2007).

The disk of the Galaxy is made of young massive blue stars, reddish HII regions (ionized clouds caused by young stars), young clusters and dust lanes and filaments, where star formation is taking place. This disk has a diameter of ≤30 kpc and a thickness of ~1 kpc. It is believed to have been formed as a result of the interaction between the infalling gas and the dwarf galaxies. As the matter grew in mass and movement around the center it flattened into a disk. The spiral arms visible today within that disk are thought to have been caused by density waves from the interactions between the stars and gas orbiting the center.

The Galaxy's center is located at about 8 kpc from the Solar System. It consists of a spherical distribution of old stars (~ billion years old) called the bulge, and weighs about 10^{10} Suns. These old stars appear red in comparison to the white/blue younger stars and star forming regions in the disk. Inside the bulge there is an indication for a weak bar (or triaxial bulge) about 3 kpc long. At the very heart of the stellar content of the bulge and the Galaxy lies a black hole with a mass of roughly 4 million solar masses. Though it is massive, Sagittarius A*, or shortly Sgr A*[1], lies on the lower limit of supermassive black holes (SMBHs) as some of these galactic black holes can reach billions of solar masses.

In 2012, a group of astronomers (Sohn *et al.*, 2012; van der Marel *et al.*, 2012a,b) were able to predict the future of the Milky Way. They measured the position and proper motion of the neighboring Andromeda galaxy and found that it is separated from our own by about 770 kpc. What they also found is that both galaxies are on a collision course (with a speed of 109 km s^{-1}) estimated to take place 6 billion years from now. The merging process will be gradual, over a billion years, where an elliptical galaxy will be born from the two spirals.

1.2 The Galactic Center

The Center of our Galaxy is made up of stars, stellar remnants, dust and molecular and ionized gas, with a supermassive black hole at its heart. These different components interact with each other and provide a very complex region of structures that have long motivated astronomers into developing new techniques and methods to better understand the phenomena and physical processes taking place there. The importance of studying our Galactic Center lies in it being the nearest galactic nucleus to us. It is located at about 8 kpc or ~ 28000 light years. The nearest center of a similar galaxy to the MW is Andromeda's (M31 or NGC 224), which is located at roughly 2.5 million light years from Earth.

---

[1]Sgr A* refers to the radio source believed to be associated with the supermassive black hole at the Center.
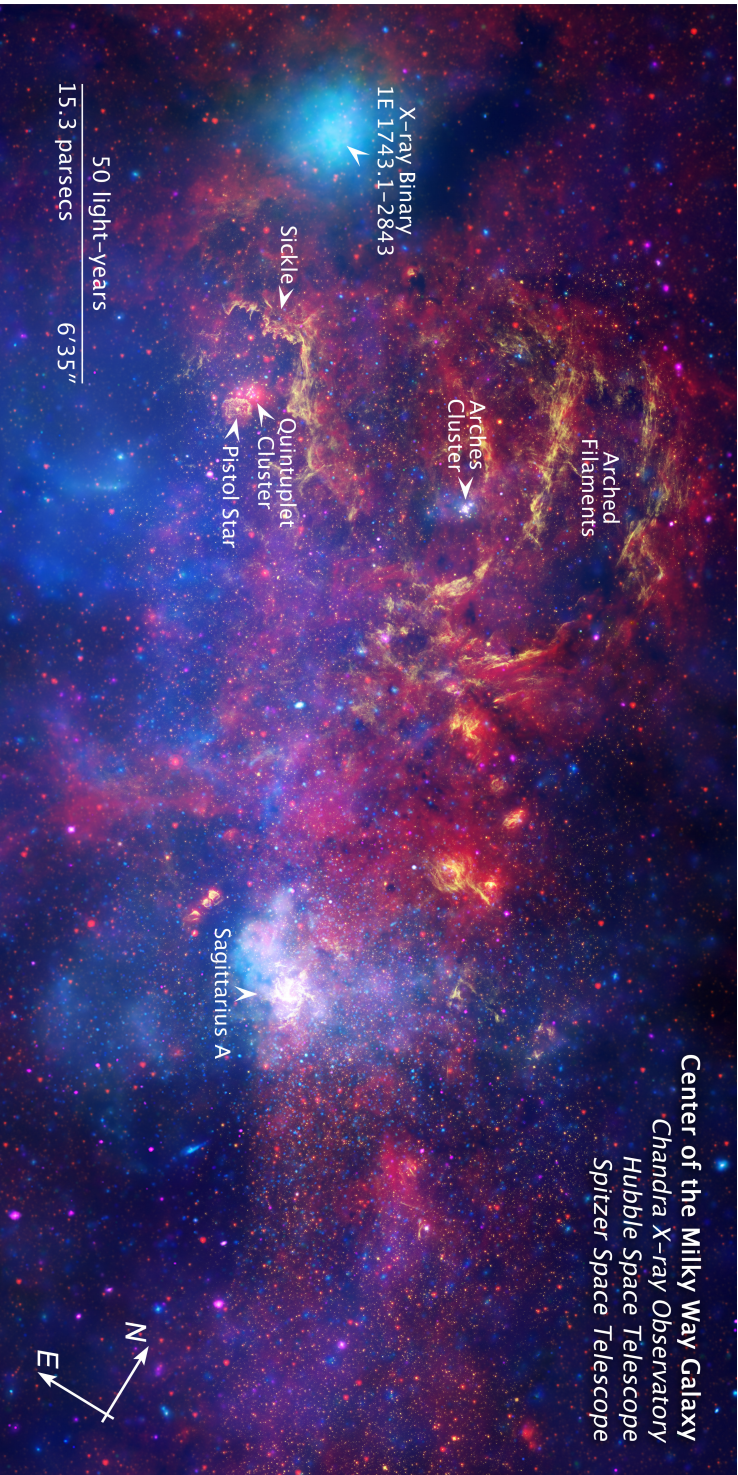
Figure 1.2: *Composite image of the central half of a degree of our Galaxy, provided by the Hubble Space Telescope, the Spitzer Space Telescope, and the Chandra X-ray Observatory. Image credit: NASA/JPL-Caltech/ESA/CXC/STScI.*

Watching the faint band of the MW on a clear night one notices the dark lanes (of dust) that prevent most of the visible light of the stars from reaching us. These dust lanes are particularly prominent when looking in the direction of the constellation Sagittarius, where the brightest region in our Galaxy, the Center, lies. However, switching to other wave bands one can peer through the dusty MW disk and see a completely different picture. The Center is bright in the radio, infrared and X-rays.

The nucleus of the MW spans about 100 pc (~300 light years). Figure 1.2 shows the Center with a composite image taken using three different telescopes at three different wavelengths, two in the infrared and one in the X-ray. The brightest spot in the image is the location of the core of the Galaxy, Sagittarius A complex. The infrared light (red) reveals the considerable number of stars hiding in visible light behind the thick veil of dust toward the Center. The radiation from these stars heats the nearby gas and dust and causes it to glow (yellow), such as the different-shaped filaments seen across the image. The arcs to the left of the mosaic are bright due to the nearby massive stellar clusters, the Quintuplet and Arches cluster, warming up the gas. The presence of massive stars is not exclusive to the stellar clusters but rather spread across the mosaic as shown by Wang *et al.* (2010) using the *Hubble Telescope* layer of the composite image of Fig. 1.2 (more details in Chapter 3). In fact, the complex gas structures seen in the mosaic are caused by the radiation and stellar winds of these massive stars. The X-ray view is quite different from the infrared one (blue and pink light). Here the higher energy emission is mostly originating from material being accreted into black holes and compact sources. The brightest region in the X-ray, Sagittarius A, is caused by diffuse gas heated to millions of degrees by outflows and winds from the SMBH, in addition to those from winds of giant stars and stellar explosions.

The Sagittarius A complex, a bright region in radio, is believed to trace matter orbiting the central black hole. One of the best images of the region is the long wavelength (~ 1 m) map of the Center shown in Fig. 1.3 from LaRosa *et al.* (2000). The image shows several supernova remnants and giant molecular clouds, such as Sgr B1 and B2. Also visible across are synchrotron emitting filaments. To get closer to the center and reveal more detailed structures, observing at shorter wavelengths with bigger telescopes becomes necessary. The largest feature that can be seen as we get closer to the Center is Sgr A East. This shell-like feature extends about $3'.5 \times 2'.5$ or 10.5×8 pc and its non-thermal emission is bright in the radio as well as in the X-ray. It is believed to be a supernova remnant (SNR), though its location extremely close to the Galactic nucleus has led some to believe that it might not be a simple SNR but something more powerful. A more recent claim is that the hypothesized supernova actually expanded into a region of lower density cleared out by the winds of massive stars (Yusef-Zadeh and Morris, 1987; Maeda *et al.*, 2002; Fryer *et al.*, 2006).

In projection, Sgr A East appears to enclose a three-armed structure called Sgr A West and a clumpy ring surrounding it. The clumpy molecular ring, known as the circumnuclear disk (CND) (Fig. 1.4) is estimated to have a mass of ~ 10^6 solar masses, consist-
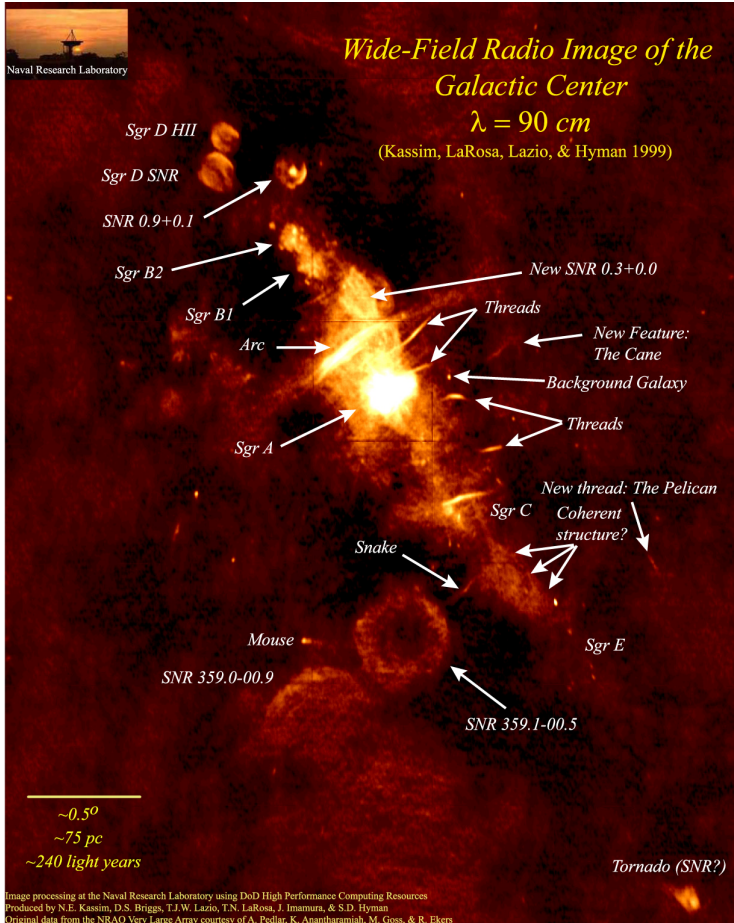
Figure 1.3: *A radio (90 cm) image of the GC region spanning a distance of 1000 light-years (∼ 300 pc). Image credit: NRAO/AUI and N.E. Kassim, Naval Research Laboratory.*

ing of several dense clouds of molecular gas (up to 10^7 cm^{-3} Guesten *et al.*, 1987; Jackson *et al.*, 1993; Wright *et al.*, 2001; Herrnstein and Ho, 2002) and warm (few 100 K) dust (Zylka *et al.*, 1995). The CND, with a radius between 1.5 and 7 pc, is believed to be orbiting the nucleus and fed by gas infall from dense molecular clouds further away from the Center. Sgr A West, also known as the "mini-spiral" can be seen in Fig. 1.4 as the three-armed structure of ionized gas and dust spanning over the central 3 pc. The emission is thermal in nature contrary to the one detected from Sgr A East. These structures are believed to be streamers of ionized matter (few tens of solar masses) on in-falling trajectories from the inner edge of the surrounding CND. This ionized gas appears to be orbiting the Center in a projected motion from east to west with a speed of about 100 km s^{-1} at a distance of ∼3 light years (Yusef-Zadeh *et al.*, 1998). Assuming a Keplerian rotation around the center,
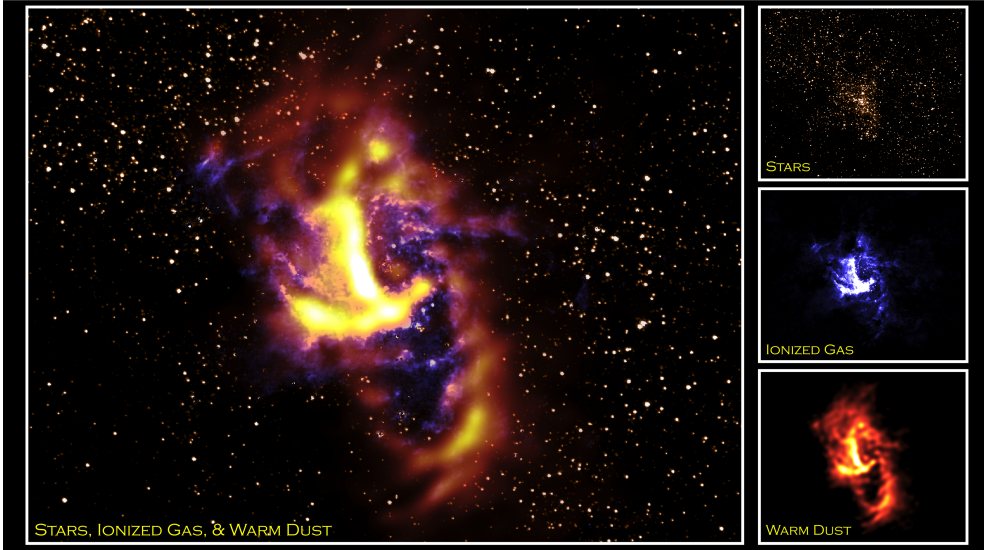
Figure 1.4: *Multi-wavelength image of the Galactic Center obtained by different telescopes. The infrared emission from stars by HST/NICMOS, ionized gas HST/NICMOS, and warm dust by SOFIA/FORCAST. The image covers the central 10 light years of the Galaxy. Image credit: Stars: NASA/HST/NICMOS; Ionized Gas: NASA/HST/NICMOS; Warm Dust: NASA/DLR/USRA/DSI/FORCAST Team/Lau* et al. *(2013).*

this corresponds to an enclosed mass of $\sim 3.5 \times 10^6 \, M_\odot$. This was the first indication for the presence of a dark mass at the center of the Galaxy. The in-falling gas also interacts with the intense winds originating from the stars located in and within the streamers and forms bow shock-like feature. These streamers are designated as the northern arm, eastern arm and the western arc. The three arms have been modeled as three bundles of Keplerian orbits around the SMBH by Zhao *et al.* (2009), while Irons *et al.* (2012) prefer a model of one-armed spiral density wave.

The nuclear stellar cluster (NSC) is what comes further in. Observations in the infrared have long shown the high density of stars at the heart of the Galaxy. However, tracing the orbits of individual stars, especially those closest to the densest region of the cluster, its center, only became possible with the aid of special techniques of Speckle imaging and the introduction of adaptive optics (AO) on 8–10 m class telescopes. Now we can reach resolutions as high as 40 mas in the near-infrared. The NSC population of stars includes mostly main sequence stars ($\sim 3 \, M_\odot$), super-giants, giants and Wolf-Rayet stars. The brightest are the IRS sources (see Fig. 1.5) such as IRS 7, 3, 13, 16 and the sources embedded in the northern arm of the mini-spiral, which can be seen as well in Fig. 1.5 through its dust emission at 3.8 μm. The cluster is dominated, as expected for a nuclear cluster, by old, late-type (red) giants, super-giants and asymptotic giant branch (AGB) stars. However, spectroscopic observations revealed that some of the bright stars are hot early-types
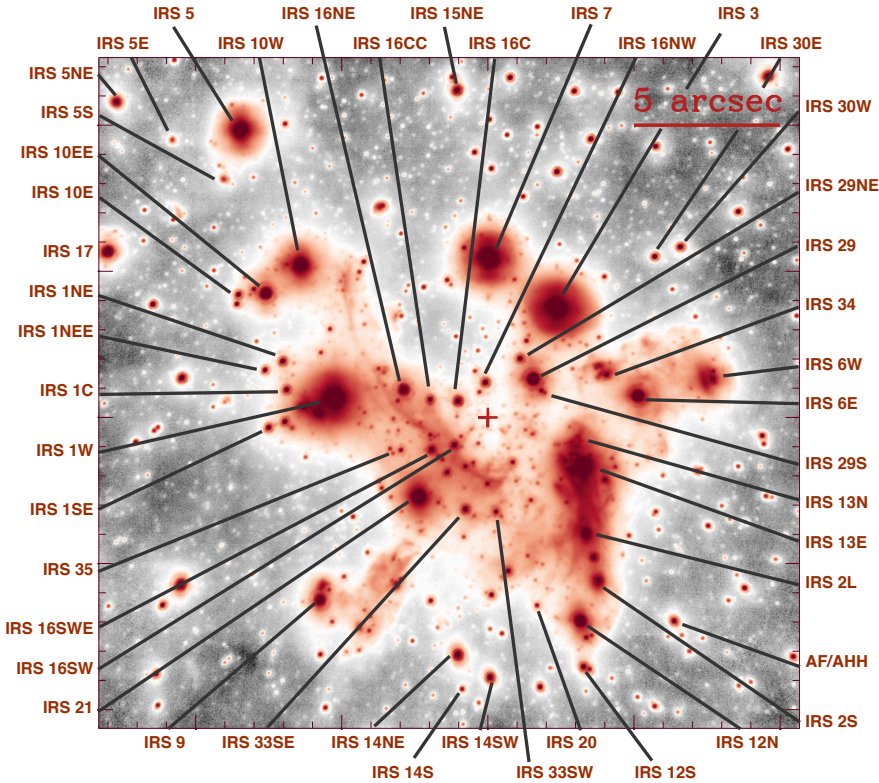
Figure 1.5: *L'-band (3.8 μm) mosaic of the Galactic Center stellar cluster obtained with VLT NaCo in 2012. Most sources are identified based on Viehmann et al. (2005). One arcsec translates to ~0.04 pc for an 8 kpc distance to the GC. The position of the supermassive black hole Sagittarius A* (Sgr A*) is marked by a cross. North is up and east is to the left.*

(Krabbe *et al.*, 1995; Genzel *et al.*, 1996; Paumard *et al.*, 2006; Tanner *et al.*, 2006). They are "HeI-stars" post main-sequence, blue super-giants and Wolf-Rayet (WR) stars with ages of 2–8 Myrs and zero age main-sequence stars (ZAMS) of masses 30–100 $M_\odot$ (Martins *et al.*, 2007).

The dusty and dense IRS 13 complex, just about 0.1 pc from the position of the central black hole, reveals a concentrated HII emission in addition to X-rays. IRS 13E is made of three O/WR stars and possibly, though this is highly debatable, an intermediate mass black

hole (IMBH). The fainter IRS 13N has long been discussed as to whether it is composed of young stellar objects (YSOs) (e.g. Mužić *et al.*, 2008) or simply dust concentrations (Fritz *et al.*, 2010). Recently, Jalali *et al.* (2014) using hydrodynamical simulations showed that strong orbital compression of clumps orbiting the SMBH on an eccentric orbit leads the gas densities to increase and overcome the tidal density of the black hole, thereby allowing stars to form that are similar to those speculated to be in the IRS 13N complex.

The "S-star cluster" (more details in Chapter 2) located in the central arcsecond, centered on the SMBH, is mainly made up of B-stars. A recently added member to the S-cluster is the fast moving cloud of gas and dust, G2, that is approaching the black hole on an eccentric orbit (Gillessen *et al.*, 2012). It is speculated that the cloud will disrupt upon its closest approach to the SMBH and lead to increased activity, starting in the X-ray band, that could span months to years. However, Eckart *et al.* (2013) argue that the object is most probably a compact dusty object (they refer to it as a dusty s-cluster object, DSO) with a star at its core. This composition will cause the amount of matter from the cloud that is accreted onto the black hole much lower that anticipated. Phifer *et al.* (2013) also prefers a hidden star scenario. Many ground-based and space telescopes have turned their attention to monitoring the activity of the galactic black hole, Sgr A*, in order to observe the disruption of the cloud live. Up to date, no increased activity of Sgr A* has been recorded besides the frequent modest flares across its observable spectrum. The increased monitoring of the central region, especially in the X-rays, led to the recent discovery of a pulsar only 0.12 pc (0.38 light years) from the black hole. The discovery came when a very bright flare was recorded by *Swift* in April, 2013 (Degenaar *et al.*, 2013; Kennea *et al.*, 2013) (see Fig. 1.6). Shortly afterwards, *NuSTAR X-ray telescope* confirmed the flaring object to be a magnetar with a spin rate of 3.76 seconds (Mori *et al.*, 2013) that is gradually slowing down due to the presence of a high magnetic field that causes the pulsar to radiate energy faster than it normally does. Eatough *et al.* (2013) infer from the pulsar's large Faraday rotation (the rotation of the plane of polarization of the emission in the presence of an external magnetic field) a dynamically important magnetic field near Sgr A*. They use the strength of its magnetic flux to explain the observed emission, from radio to X-ray wavelengths, from the black hole. Evidence of such dynamically important magnetic fields threading the accretion disks of extragalactic supermassive black holes have been reported recently by Zamaninasab *et al.* (2014).

1.3 Observations in the Infrared

William Herschel was the first to discover infrared (IR) radiation in 1800 when he measured thermal radiation beyond the red portion of the visible light, hence the name infrared. On the electromagnetic spectrum infrared radiation lies in the wavelength range of $\sim 1 - 1000 \, \mu$m (1 mm). In Astronomy the IR range is divided into subcategories of (i) near-infrared (NIR) (0.7–5 μm); (ii) mid-infrared (MIR) (5–30 μm); and (iii) far-infrared (FIR) (30 –1000 μm). The Earth's atmosphere only allows certain bands of radiation to pass through
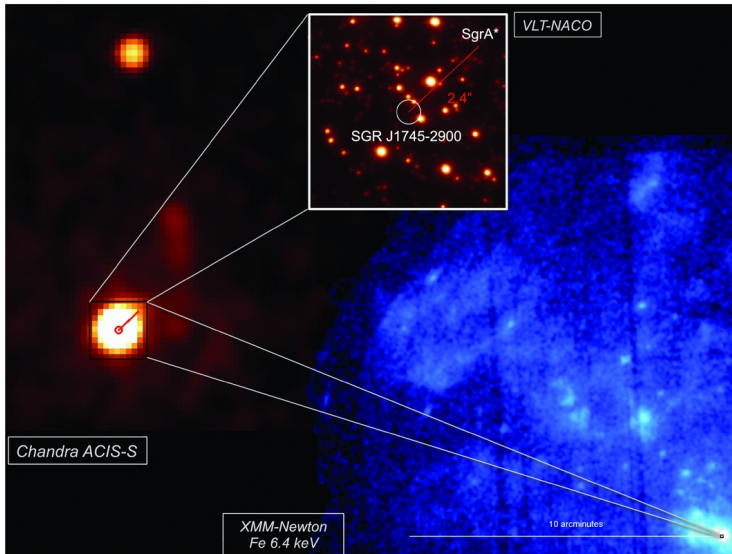
Figure 1.6: *Multiwavelength view of the field of SGR J1745-2900 and Sgr A*. The blue image shows the XMM-Newton 6.4 keV Galactic Center view (Ponti et al., 2013), and the black square is a $5'' \times 5''$ box around the position of the magnetar. The inset shows the first Chandra ACIS observation of the source. The VLT/NaCo image in the near-infrared is in K_S-band (Schödel et al., 2009). Image credit: Rea et al. (2013)*

to the surface; they are called the atmospheric windows. Atmospheric opacity is essential for sustaining life on Earth, as it blocks most high energy radiation like X-rays, gamma rays and most of the ultraviolet light. Visible light passes through in addition to lower energy radio waves. Infrared radiation, on the other hand, gets for the most part absorbed by water vapor and also carbon dioxide and oxygen molecules in the atmosphere, and only reaches us in a few narrow ranges (see Fig. 1.7). Infrared astronomy is the study of the Universe in the infrared regime. Star forming regions and cool stars with surface temperatures of a few thousand degrees, and other celestial objects are mostly suited to be studied in the IR. The most important atomic and molecular transitions occur in the infrared. These are essential to understand the physical conditions and processes in planetary atmospheres, interstellar clouds, and in distant galaxies. Also the dust present in the heart of galaxies and stellar clusters absorbs the optical and ultraviolet light and re-emits it at the longer IR wavelengths. Circumstellar dusty regions are also bright in the infrared. Almost anything embedded in dust can be peered through with infrared eyes. As a local example in our own Solar System, the zodiacal light is the radiation from the dust particles that were created by evaporating comets and colliding asteroids. Another important application to infrared astronomy is the study of the early Universe, as the visible and ultraviolet light emitted that early in time is now red-shifted and can be only observed in the infrared. The *NASA/ESA James Webb Space Telescope (JWST)* is especially designed to study that era.
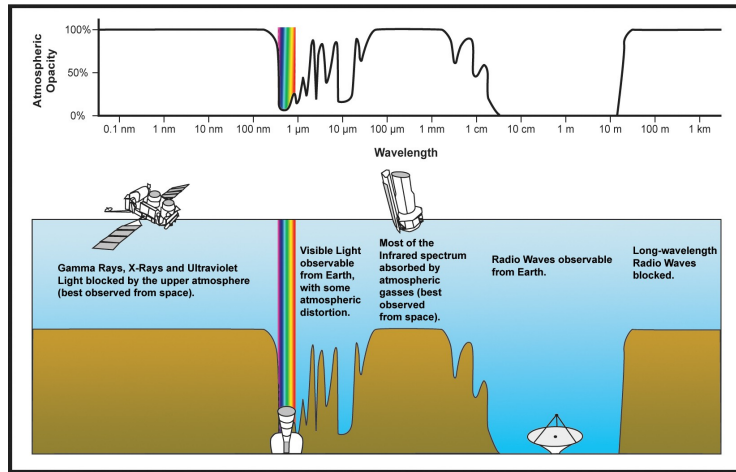
Figure 1.7: *Atmospheric electromagnetic transmittance or opacity. Image credit: NASA/JPL-Caltech*

Ground-based observations in the NIR started as early as the 1960s. It was not till the 70s that observations at longer wavelengths became possible with the aid of high-flying airplanes. The first space-borne infrared telescope, the *InfraRed Astronomical Satellite (IRAS)*, came into operation in 1983. The biggest problem with infrared astronomy is the emission from the atmosphere, which peaks at about 10 μm. Therefore, ground-based telescopes are placed on high mountains in dry regions where the emission from astronomical objects does not get absorbed completely by the presence of water vapor. For the mid to far-IR regimes the only way is to use rockets, balloons, aircraft and space telescopes as some bands get absorbed completely by the Earth's atmosphere.

Below I describe two of the techniques that are currently employed on ground-based telescopes to observe celestial objects in the near and mid-infrared. I am focusing on these two bands and, hence these two methods only, as they are the ones that will be addressed in this dissertation. The observations I use were taken using the European Southern Observatory Very Large Telescope (ESO VLT)[2]. The VLT is situated on top of Cerro Paranal at an altitude of 2635 m in the Chilean Atacama desert. The site is particularly suitable for optical and infrared observations as the Atacama desert is considered one of the driest places on Earth. The telescope is one of world's most advanced optical instruments, consisting of four Unit Telescopes (UTs; Antu, Kueyen, Melipal and Yepun) with primary mirros of 8.2 m diameter and four movable 1.8 m diameter Auxiliary Telescopes (ATs). The light of these individual telescopes can be combined to form a giant "interferometer" (VLTI) that can achieve resolutions up to 25 times finer than with the individual ones. The location of the VLT is most suitable to study the Center of our Galaxy as it is mostly visible from the southern hemisphere (see Fig. 1.8).

---

[2]http://www.eso.org/public/teles-instr/paranal/

Figure 1.8: *A panorama photo, taken by ESO Photo Ambassador Yuri Beletsky, that shows the view of the starry sky from the site of ESO's Very Large Telescope (VLT) at Cerro Paranal during the total lunar eclipse of 21 December 2010. Image credit: ESO/Y. Beletsky.*

I first start with the adaptive optics observing technique currently implemented on the VLT instrument NaCo. The Nasmyth Adaptive Optics System (NAOS) and the High-Resolution Near IR Camera (CONICA), in short NaCo, provides multimode, adaptive optics corrected observations in the range 1–5 μm[3].

Adaptive Optics in the Near Infrared

Atmospheric turbulence makes it rare for any telescope to reach its diffraction-limited resolution, which is determined by the diameter of its primary mirror and the observing wavelength ($1.22\lambda/D$). For example, the diffraction limit of the VLT at 2.2 μm is $0.057''$. Due to the presence of the atmosphere the equation becomes $\lambda/r_0 \sim 0.7''$, where another factor comes into play, the Fried parameter. The Fried parameter represents the strength of the turbulence and is dependent on the wavelength by $\lambda^{(6/5)}$, e.g. at 2.2 μm r_0 is about 60 cm. There is another important parameter for observations and that is the correlation or coherence time of the turbulence, τ_0. This parameter is related to r_0 and for a wind speed of 10 m s^{-1}, $\tau_0 \sim 60$ ms at 2.2 μm. The larger these two parameters are the more stable the atmospheric conditions. Luckily for observing the Center, Sagittarius constellation culminates at the Zenith during the southern winter, which happens to be the most suited in terms of the weather conditions.

To improve the telescope's resolution and bring it closer to its diffraction-limited value, a method called Adaptive Optics (AO) is employed to account for the atmospheric turbulence. AO does a real-time compensation to the wavefront of the observed astronomical sources by measuring these distortions on a known bright source called a guide star (GS). A wavefront sensor measures the distortions on the otherwise flat wavefront coming from the star where they are processed by a real-time computer and fed into a deformable mirror to correct for them (see Fig. 1.9). The image quality is determined by the Strehl Ratio

---

[3]The description and numbers mentioned are optimized for Paranal observing site of the VLT, and taken from NaCo manual: http://www.eso.org/sci/facilities/paranal/instruments/naco/doc/VLT-MAN-ESO-14200-2761_v94.pdf
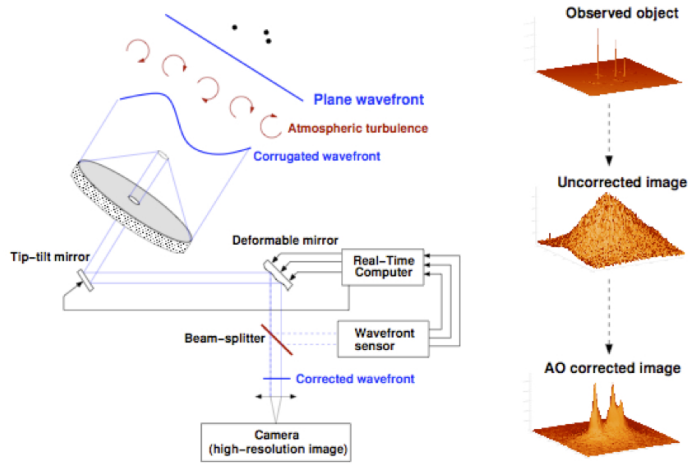
Figure 1.9: *Principle of adaptive optics system. Image credit: ESO NaCo user manual.*

(SR), which refers to the amount of light inside the diffraction-limited core compared to the total flux; i.e. the higher the ratio the better the image quality. For K_s-band observations the optimum achieved SR is ~ 50%, while for L' it can reach as high as 70%. For shorter wavelengths, J-band, the SR may only reach a few percent.

In general a good AO correction depends on the observing conditions characterized by the seeing ($\epsilon = 0.98 \lambda / r_0$ Fried, 1966), how bright the guide star is and its distance to the object of interest. The brighter and closer the GS is to the observing region the better the correction and the resulting point spread function (PSF) is closer to the diffraction limit. For example, observations of the central cluster utilize the presence of the NIR bright (K_s-band magnitude ~ 7) supergiant IRS 7, located about 5.6″ north of Sgr A*, as an AO guide star. Other fields of interest that do not have a nearby natural guide star can use the laser guide star (LGS)[4]. Adaptive optics works well with short-wavelength observations (shortward of 4.2 μm), while for longer wavelengths the additional components associated with the AO system introduce higher IR background and the deformable mirror brings background fluctuations that do not cancel correctly.

All IR observations have to be corrected for sky emission and for detector cosmetics. The sky background for $\lambda \leq 2.2\,\mu$m is caused by OH emission at an altitude of ~ 80 km and have to be sampled approximately every 2 hours of on-source observations. However, at longer wavelengths the thermal background of the atmosphere and telescope dominate

---

[4]LGS is an artificial source created by a Sodium Laser (589.5 nm) focused at 90 km altitude in the mesosphere. The atomic sodium present at that height produces an artificial star of visual magnitude of 11.

and this means that the sky has to be sampled more frequently as the time scale of the fluctuations is short. The detector cosmetics can be minimized by a method called *jitter*, which is done by taking several images offseted by a small value of the object of interest. This way the astronomical sources do not always lie on the same position of the detector array. This method can also be used to estimate the sky background for non-crowded fields. Crowded fields on the other hand need a separate sky observations of a nearby field relatively devoid of sources. For the crowded Galactic Center (GC) field this is achieved by observing a dark cloud located about $400''$ north and $713''$ west of the Center.

After the images reach the user, data reduction steps have to be applied to make them suitable for science investigation. These steps involve:

- sky-subtraction: subtracting the sky frame from the object frames.

- flat-fielding: dividing the object frame by a map of the pixel response of the detector array.

- correcting for dead or bad pixels: done by replacing the bad/dead pixels with interpolations from neighboring pixels.

Then the reduced images are shifted and stacked in a cube with a mean average to get a mosaic image of the celestial object of interest.

Chopping/Nodding Technique in the Mid Infrared

VISIR, the VLT spectrometer and imager for the mid-infrared, is the instrument used to obtain the MIR data I discuss in this thesis. It provides diffraction-limited imaging at high sensitivity in two MIR wavelength ranges: the N-band ($\approx 8 - 13\ \mu$m) and the Q-band (16.5 – 24.5 μm). It also offers a slit spectroscopy with a spectral resolution between 150 and 30000 km s^{-1}[5].

As the spatial resolution is either determined by the telescope's mirror size (solid line in Fig. 1.10 following the relation $1.22\lambda/D$) or the atmospheric seeing, one can derive the wavelength dependence of the seeing. This is done by the Roddier formula which approximates the seeing by studying the spatial coherence radius of the atmosphere in the telescope beam, $\propto \lambda^{-0.2}$ (see dot-dashed lines in Fig. 1.10). According to the figure, for visible seeing below $0.6''$ VISIR is already providing diffraction limited images. Ideally, MIR observations are better performed with space-borne telescopes since they would be above the atmosphere and avoid its bright thermal background. However, the spatial resolution
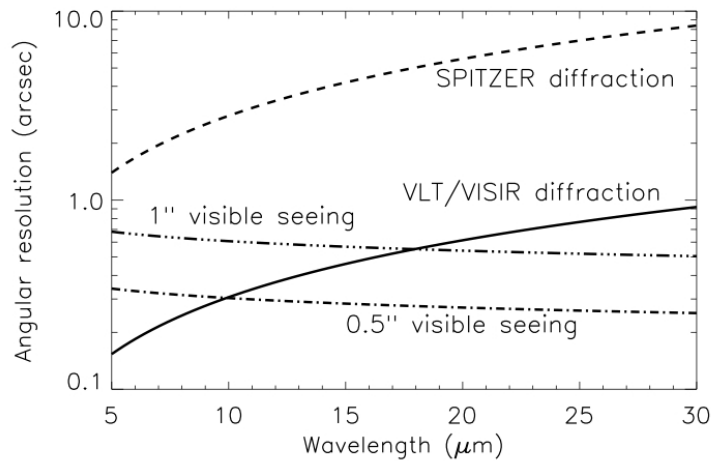

Figure 1.10: *VLT diffraction limit (solid line) versus seeing. The Roddier dependence is shown for two optical seeings (dashed-dot). Plotted for comparison is the Spitzer Space Telescope diffraction limits (dashed line). Image credit: ESO VISIR user manual.*

achieved by ground-based observatories are usually higher than those by space telescopes due to the limited-size mirrors of the latter. For instance, VISIR can reach diffraction-limited resolutions of ~ 0.3″ (FWHM) in the *N*-band, an order of magnitude better than what is reached by the *Spitzer Space Telescope (SST)* (see Fig. 1.10).

The two atmospheric windows, *N* and *Q* bands, in the MIR can be seen in Fig. 1.11. Reading the transmission curve, one can see that the *N*-band window is almost entirely transparent in certain ranges, unlike the *Q*-band which can on average be only 60% transparent. Outside these two windows, the rest of the thermal radiation gets absorbed before reaching the surface by mainly H_2O, CH_4, CO_2, CO, O_2, O_3 molecules. Besides absorbing the incoming infrared light, the atmosphere acts as a strong background emitter with a black-body curve at ~ 253 K. The telescope also emits thermal radiation, which for the VLT is at 283 K. For this reason, the VISIR detectors and the whole instrument are cooled to very low temperatures (few Kelvins for the detectors) to avoid internal background contamination.

To account for the MIR background of the sky and the telescope a method called chopping/nodding is implemented. It is a set of differential observations wherein the secondary mirror of the telescope is moved at a rate faster than the background fluctuations between two positions on the sky. The first is on-source and measures the astronomical source in addition to the background; the second position is referred to as off-source and measures the background alone. For VISIR at Paranal, observing in the *N*-band requires a chopping frequency of 0.25 Hz while for the *Q*-band 0.5 Hz. The chopping technique
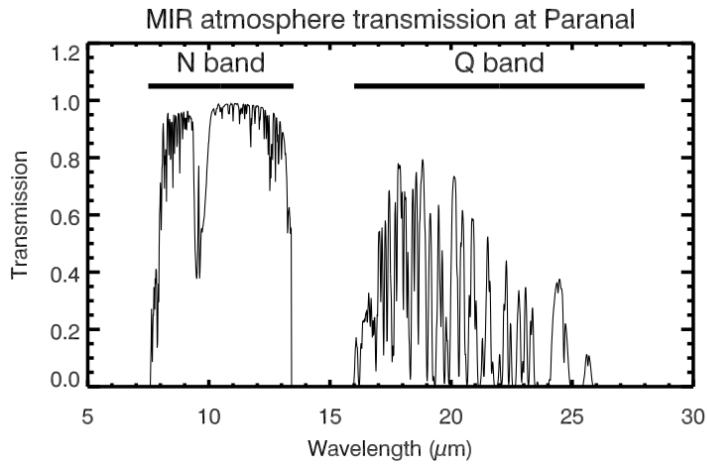
Figure 1.11: *MIR atmospheric transmission at Paranal site computed for an altitude of 2600 m and 1.5 mm of precipitable water vapor at zenith. Image credit: ESO VISIR user manual.*
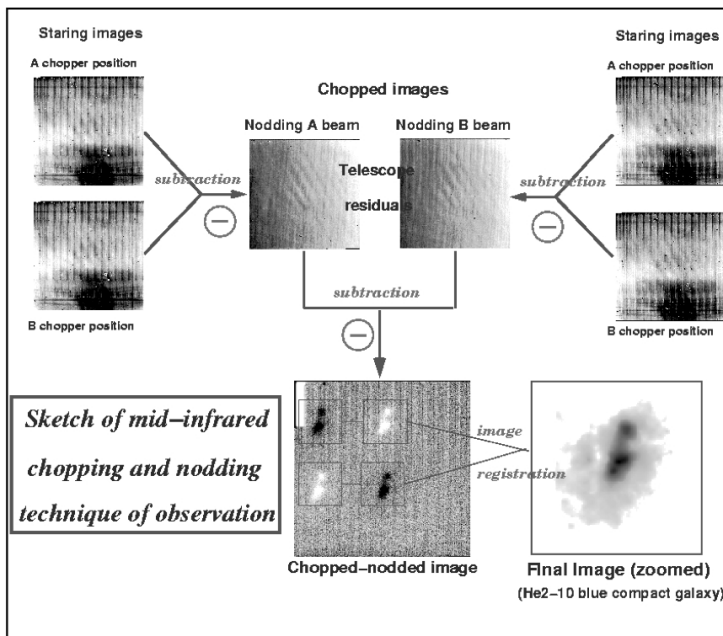
Figure 1.12: *Illustration of the chopping and nodding technique on observations of the blue compact galaxy He2-10. The galaxy only appears after chopping and nodding. Image credit: VISIR commissioning team, June 2004, from ESO VISIR user manual.*

accounts for the sky and telescope emission which is removed by subtracting the images taken at the two positions, i.e. on-source image - off-source image. However, changing the position of the secondary mirror introduces a residual background resulting from the optical path difference between the two chopper positions. This additional background is removed or mostly suppressed by nodding the whole telescope to an off-source position where again the same chopping cycle is repeated. This technique works well as this residual background varies on a time-scale longer than the sky background. After the images from the two nodding positions are subtracted from each other, the resulting product can contain 3–4 images of the source depending on the settings used for the chopping/nodding of the telescope, see Fig. 1.12 for an illustration of the technique.

The reduction of mid-IR data is similar to NIR data (see previous section 1.3). Besides the chopping and nodding corrections, bad or dead pixels have to be taken care of. According to the ESO VISIR data reduction guidelines, there is usually no flat fielding done during the reduction of MIR data as the background fluctuations at mid IR wavelengths are large.

1.4 Dissertation Outline

This dissertation deals with Galactic Center data taken at two wavelengths regimes, near and mid-infrared, which I present in two corresponding chapters. Each of these chapters will have its own abstract, introduction, data and results then the discussion and conclusions.

Chapter 2

Here I analyze NIR 2.2 μm images of the S-star cluster to study the diffuse emission surrounding the central black hole, Sgr A*. The chapter starts with a reference to the published works addressing the inner regions of the cluster in terms of stellar populations, distribution and dynamics. I then lay out the approach we follow to study the diffuse emission, and the attempt to explain it by a distribution of faint stars. The effect a dark mass of individual perturbers will have on the orbit of the star S2, around Sgr A*, is then explored. Finally, I simulate the line-of-sight clustering of below-the-detection-limit stars and how they can be mistaken as new faint sources. The chapter ends with a discussion and summary of the results and their implications.

Chapter 3

This chapter lists the MIR data I use to study the faint compact sources in and around the nuclear star cluster and Quintuplet cluster. First I give an introduction to the regions and the properties that make them suitable and interesting for such an investigation. The details of the data and the reduction process are given be-

fore highlighting the main results obtained for the two regions. I then conclude the chapter with a summary and an outlook for future work.

Chapter 4

An interesting source was found while analyzing the mid-infrared mosaics of the central cluster. This source is worth further investigation for its morphology and location. The morphology resembles a bow shock caused by the interaction of a supersonic wind from a star with the surrounding medium. The location is interesting for the chance alignment of our source with other previously studied bow shocks and features that are closer to the central black hole, and were found to be caused by an external wind blowing from its direction. This chapter highlights the discussion of the long-sought jet/outflow from the SMBH and also the combined stellar wind of the central cluster.

Chapter 5

I conclude the dissertation by highlighting its main results and discussing their implications, while laying the ground for follow-up studies.

THE NATURE OF DIFFUSE NIR EMISSION IN THE INNER ARCSECOND

Sgr A*, the supermassive black hole at the center of the Milky Way, is surrounded by a small cluster of high velocity stars, known as the S-stars. I aim to constrain the amount and nature of stellar and dark mass associated with the cluster in the immediate vicinity of the black hole. I use near-infrared imaging to determine the K_s-band luminosity function of the S-star cluster members, and the distribution of the diffuse background emission and the stellar number density counts around the central black hole. This allows us to determine the stellar light and mass contribution expected from the faint members of the cluster. We then use post-Newtonian N-body techniques to investigate the effect of stellar perturbations on the motion of S2, as a means of detecting the number and masses of the perturbers. I find that the stellar mass derived from the K_s-band luminosity extrapolation is much smaller than the amount of mass that might be present considering the uncertainties in the orbital motion of the star S2. Also the amount of light from the fainter S-cluster members is below the amount of residual light at the position of the S-star cluster after removing the bright cluster members. If the distribution of stars and stellar remnants is strongly enough peaked near Sgr A*, observed changes in the orbital elements of S2 can be used to constrain both their masses and numbers. Based on simulations of the cluster of high velocity stars I find that at a wavelength of 2.2 μm close to the confusion level for 8 m class telescopes blend stars will occur (preferentially near the position of Sgr A*) that last for typically 3 years before they dissolve due to proper motions.

2.1   Introduction

Using 8–10 m class telescopes, equipped with adaptive optics (AO) systems, at near-infrared (NIR) wavelengths has allowed us to identify and study the closest stars in the vicinity of the supermassive black hole (SMBH) at the center of our Milky Way. These stars, referred to as the S-star cluster, are located within the innermost arcsecond, orbiting the SMBH, Sagittarius A* (Sgr A*), on highly eccentric and inclined orbits. Up till now, the trajectories of about 20 stars have been precisely determined using NIR imaging and spectroscopy (Gillessen *et al.*, 2009b,a). This orbital information is used to determine the mass of the SMBH and can in principle be used to detect relativistic effects and/or the mass distribution of the central stellar cluster (Rubilar and Eckart, 2001; Zucker *et al.*, 2006; Mouawad *et al.*, 2005; Gillessen *et al.*, 2009b).

One of the brightest members of that cluster is the star S2. It has the shortest observed orbital period of ~15.9 years, and was the star used to precisely determine the enclosed dark mass, and infer the existence of a ~4 million solar mass SMBH, in our own Galactic Center (GC; Schödel *et al.*, 2002; Ghez *et al.*, 2003). The first spectroscopic studies of S2, by Ghez *et al.* (2003) and later Eisenhauer *et al.* (2005), revealed its rotational velocity to be that of an O8–B0 young dwarf, with a mass of 15 $M_\odot$ and an age of less than 10^6 yrs. Later, Martins *et al.* (2008) confined the spectral type of S2 to be a B0–2.5 V main-sequence star with a zero-age main-sequence (ZAMS) mass of 19.5 $M_\odot$. The fact that S2, along with most of the S-stars, is classified as typical solar neighborhood B2–9 V stars, indicates that they are young, with ages of 6–400 Myr (Eisenhauer *et al.*, 2005). The combination of their age and the proximity to Sgr A* presents a challenge to star formation theories. It is still unclear how the S-stars were formed. Being generated locally requires that their formation must have occurred through non-standard processes, like formation in at least one gaseous disk (Löckmann *et al.*, 2009) or via an eccentricity instability of stellar disks around SMBHs (Madigan *et al.*, 2009). Alternatively, if they formed outside the central star cluster, about 0.3 parsec core radius (e.g. Buchholz *et al.*, 2009; Schödel *et al.*, 2007), there are several models that describe how they may have been brought in (e.g. Hansen and Milosavljević, 2003; Kim *et al.*, 2004; Levin *et al.*, 2005; Fujii *et al.*, 2009, 2010; Merritt *et al.*, 2009; Gould and Quillen, 2003; Perets *et al.*, 2007, 2009). For a detailed description of these processes see Perets and Gualandris (2010).

Stellar dynamics predict the formation of a cusp of stars at the center of a relaxed stellar cluster around a SMBH. This is manifested by an increase in the three dimensional stellar density of old stars and remnants towards the center with power-law slopes of 1.5 to 1.75 (Bahcall and Wolf, 1976; Murphy *et al.*, 1991; Lightman and Shapiro, 1977; Alexander and Hopman, 2009).

The steep power-law slope of 1.75 is reached in the case of a spherically symmetric single mass stellar distribution in equilibrium. For a cluster with differing mass composi-
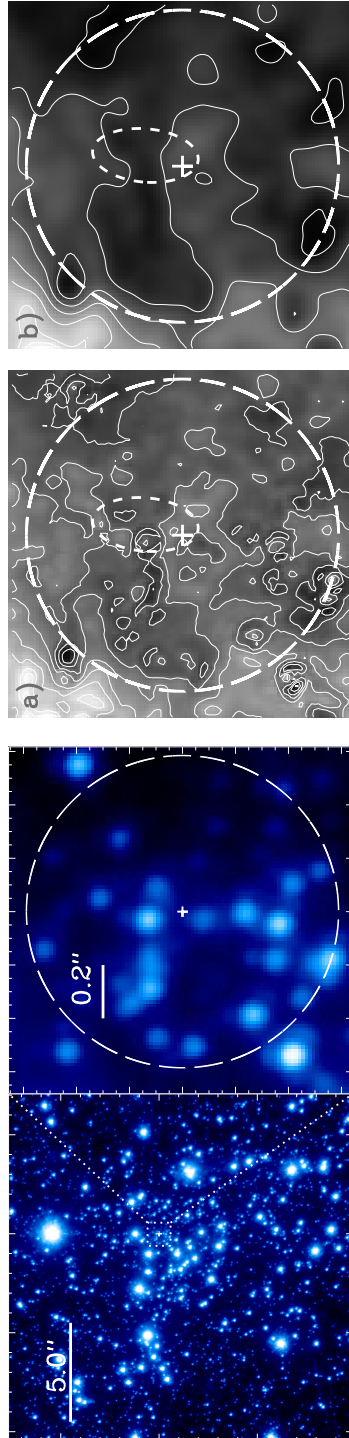
Figure 2.1: *Left: 17.5″ × 17.5″ NACO K_s-band mosaic of the central cluster zoomed in to the inner 1–2″ region around Sgr A*. The inner region is indicated by a dashed (white) circle. Right: **a)** Map of the diffuse background light within a circle of 0.69″ radius centered on the position of Sgr A*, shown here as a cross at the center. The projected orbit of the star S2 is over-plotted as an ellipse. **b)** The same map smoothed by convolution with a Gaussian beam of FWHM = 6 pixels. The contours levels are at 95%, 90%, 80%, 70%, 60%, 50%, 40%, 30%, 20% and 10% of the maximum flux value for each image.*

tion, mass segregation sets in, where the more massive stars sink towards the center, while the less massive ones remain less concentrated. This leads to the shallow density distribution of 1.5 (Bahcall and Wolf, 1977). Later numerical simulations and analytical models confirmed these results (Freitag *et al.*, 2006; Preto and Amaro-Seoane, 2010; Hopman and Alexander, 2006b). These steep density distributions were expected for the central cluster considering its age, which is comparable to the estimates of the two-body relaxation-time of 1–20 Gyr for the central parsec (Alexander, 2005; Merritt, 2010; Kocsis and Tremaine, 2011). However, observations of the projected stellar number density, which can be related to the three dimensional density distribution, revealed that the cluster's radial profile can be fitted by two power-law slopes. The slope for the whole cluster outside a radius of $\sim 6''$ (corresponding to 0.22 parsec) was found to be as steep as 1.8 ± 0.1, while inside the break radius the slope was shallower than expected and reached an exponent of 1.3 ± 0.1 (Genzel *et al.*, 2003; Schödel *et al.*, 2007). These findings motivated the need to derive the density profiles of the distinct stellar populations, given that recent star formation (6 Myr, Paumard *et al.*, 2006) at the GC gave birth to a large number of high-mass young stars that would be too young to reach an equilibrium state. Using adaptive optics and intermediate-band spectrophotometry Buchholz *et al.* (2009) found the distribution of late-type stars (K giants and later) to be very flat and even showing a decline towards the Center (for a radius of less that $6''$), while the early-type stars (B2 main-sequence and earlier) follow a steeper profile. Similar results were obtained later by Do *et al.* (2009) and Bartko *et al.* (2010).

These surprising findings required new models to explain the depletion in the number of late-type giants in the central few arcseconds around the SMBH. Such attempts involved Smooth Particle Hydrodynamics (SPH) and Monte Carlo simulations which tried to account for the under density of giants by means of collisions with other stars and stellar remnants (Dale *et al.*, 2009; Freitag, 2008). Another explanation could be the disturbance of the cusp of stars after experiencing a minor merger event or an in-spiraling of an intermediate-mass black hole (IMBH), which then would lead to deviations from equilibrium; hence causing a shallower power-law profile of the cusp (Baumgardt *et al.*, 2006). Merritt (2010) explains the observations by the evolution of a parsec-scale initial core model.

Mouawad *et al.* (2005) presented the first efforts to determine the amount of extended mass in the vicinity of the SMBH allowing for non-Keplerian orbits. Using positional and radial velocity data of the star S2, and leaving the position of Sgr A* as a free input parameter, they provide, for the first time, a rigid upper limit on the presence of a possible extended dark mass component around Sgr A*. Considering only the fraction of the cusp mass $M_{S2_{apo}}$ that may be within the apo-center of the S2 orbit, Mouawad *et al.* (2005) find $M_{S2_{apo}} / (M_{SMBH} + M_{S2_{apo}}) \leq 0.05$ as an upper limit. This number is consistent with more recent investigations of the problem (Gillessen *et al.*, 2009a). Due to mass segregation, a large extended mass in the immediate vicinity of Sgr A*, if present, is unlikely to be dominated in mass of sub-solar mass constituents. It could well be explained by a cluster of

high mass-to-light ratio (M/L) stellar remnants, which may form a stable configuration.

From the observational point of view, several attempts have been made recently to tackle the missing cusp problem. Sazonov *et al.* (2011) proposed that the detected $1''$ sized thermal X-ray emission close to Sgr A* (Baganoff *et al.*, 2001, 2003) can be explained by the tidal spin-ups of several thousand late-type main-sequence stars (MS). They use the *Chandra* X-ray data to infer an upper limit on the density of these low-mass main-sequence stars. Furthermore, using *Hubble* Space Telescope (HST) data, Yusef-Zadeh *et al.* (2012b) derived a stellar mass profile, from the diffuse light profile in the region $< 1''$ around Sgr A*, and by that they explained the diffuse light to be dominated by a cusp of faint K0 dwarfs.

Up to now, the true distribution of the Nuclear Star Cluster, especially the S-stars, is yet to be determined. No investigations have confirmed or ruled out the existence of a cusp of relaxed stars and stellar remnants around Sgr A*, as predicted by theory. An excellent dataset to investigate the stellar content of the central arcsecond around Sgr A* is the NIR K_s-band (2.2 μm) data (see Fig. 2.1) used in Sabha *et al.* (2010), hereafter NS10. In that case I subtracted the stellar light contribution to the flux density measured at the position of Sgr A*. The aim of this work is then to analyze the resulting image of the diffuse NIR background emission close to the SMBH. This emission is believed to trace the accumulative light of unresolved stars (Schödel *et al.*, 2007; Yusef-Zadeh *et al.*, 2012b). I explain the background light by extrapolating the K_s-band luminosity function (KLF) of the innermost (1–$2''$, corresponding to 0.05 parsecs for a distance of 8 kpc to the GC) members of the S-star cluster to fainter K_s-magnitudes. I compare the cumulative light and mass of these fainter stars to the limits imposed by observations. We then extend our analysis to explore the possible nature of this background light by testing its effect on the observed orbit of the star S2. Furthermore, I simulate the distribution of the unresolved faint stars ($K_s > 18$) and their combined light to produce line-of-sight clusterings that have a compact, close to stellar, appearance.

This chapter is structured as follows: Section 2.2 deals with a brief description of the observation and data reduction. I describe in Section 2.3 the method used and discuss the different observational limits employed to test our analysis. Exploring the possible contributors to the dark mass within the orbit of S2 is done in Section 2.4. In Section 2.5 I give the results obtained by simulating the distribution of faint stars and the possibility of producing line of sight clusterings that look like compact stellar objects. I summarize and discuss the implications of our results in Section 2.6. I adopt throughout this chapter $\Sigma(R) \propto R^{-\Gamma}$ as the definition for the projected density distribution of the background light, with R being the projected radius and Γ the corresponding power-law index.

2.2   Observations and Data Reduction

The near-infrared (NIR) observations have been conducted at the Very Large Telescope (VLT) of the European Southern Observatory (ESO) on Paranal, Chile. The data were obtained with YEPUN, using the adaptive optics (AO) module NAOS and the NIR camera/spectrometer CONICA (briefly "NaCo"). The data were taken in the K_s-band (2.2 μm) on the night of 23 September 2004, and is one of the best available where Sgr A* is in a quiet state. Basic NIR data reduction steps have been applied (see Sect. 1.3) to the individual frames and then they were combined to form a mosaic of the Center (see Fig. 2.1).

The flux densities were measured by aperture photometry with circular apertures of 66 mas radius. They were corrected for extinction, using A_{K_s} = 2.46 derived for the inner arcsecond from Schödel *et al.* (2010). Possible uncertainties in the extinction of a few tenths of a magnitude do not influence the general results obtained in this chapter. The flux density calibration was carried out using zero points for the corresponding camera setup and a comparison to known K_s-band flux densities of IRS16C, IRS16NE (from Schödel *et al.*, 2010; also Blum *et al.*, 1996) and to a number of the S-stars (Witzel *et al.*, 2012).

2.3   The Central Few Tenths of Parsecs

In NS10 I gave a stringent upper limit on the emission from the central black hole in the presence of the surrounding S-star cluster. For that purpose, three independent methods were used to remove or strongly suppress the flux density contributions of these stars, in the central ~ 2″, in order to measure the flux density at the position of Sgr A*. All three methods provided comparable results, and allowed a clear determination of the stellar light background at the center of the Milky Way, against which Sgr A* has to be detected. The three methods, linear extraction of the extended flux density, automatic and iterative point spread function (PSF) subtraction were carried out assuming that the extracted PSF in the central few arcseconds of the image is uniform. Investigations of larger images (e.g. Buchholz *et al.*, 2009) show that on scales of a few arcseconds the constant PSF assumption is valid, while for fields ≥ 10″ the PSF variations have to be taken into account.

Figure 2.2 is a map of the 51 stars adopted from the list in Table 3 of NS10. The stars are plotted relative to the position of Sgr A*. The surface number density of these detected stars, within a radial distance of about 0.5″ from Sgr A*, is 68 ± 8 arcsec^{-2}, with the uncertainty corresponding to the square-root of that value. This value agrees with the central number density of 60 ± 10 arcsec^{-2} given by Do *et al.* (2009). Extrapolating the KLF allows us to test if the observed diffuse light across the central S-star cluster, or the amount of unaccounted dark mass, can be explained by stars.
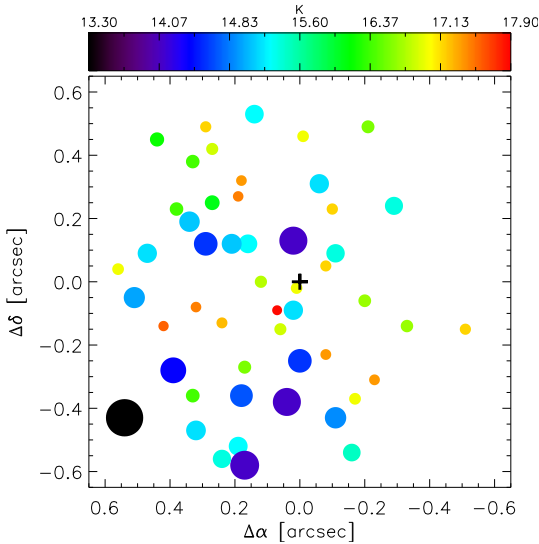
Figure 2.2: *Map of the 51 stars listed in Table 3 from NS10. The color of each star indicates its K_s-magnitude. The size of each symbol is proportional to the flux of the corresponding star. The position of Sgr A* is indicated by a cross at the center.*

KLF of the S-star Cluster

Figure 2.3 shows the KLF histogram derived for the stars detected in the central field, (Fig. 2.2). I improve the KLF derivation by choosing a fixed number of bins that allows for about 10 sources per bin while providing a sufficient number of points to allow for a clear linear fit. The Red Clump (RC)/Horizontal Branch (HB) stars, around $K_s \approx 14.5$, are in one bin, so the RC/HB bump is visible there (Schödel *et al.*, 2007). For estimating the uncertainty, I randomized the start of the first bin in an interval between $K_s = 13.0$ to 14.2 and repeated the histogram calculation 10^5 times. The number of sources in each bin was then determined by taking the average of all iterations and the uncertainties were subsequently derived from the standard deviation. I derive a least-square linear slope of $d \log(N)/d(K_s) = \alpha = 0.18 \pm 0.07$, which compares well with the KLF slope of 0.3 ± 0.1 derived in NS10 and also with the KLF slope of 0.21 ± 0.02 found for the inner field ($R < 6''$) by Buchholz *et al.* (2009). For the magnitudes up to $K_s = 17.50$ within the central $0.69''$ radius, I detect no significant deviation from a straight power-law. This implies that the completeness is high and can be compared to the ~70% value derived for $\mathrm{mag}_K = 17$ by Schödel *et al.* (2007) where the authors introduced artificial stars into their NIR image and attempted re-detecting them. However, for $K_s = 17.50$ to 18.25 the stellar counts drop quickly to about 20% of the value expected from the straight power-law line; hence the last K_s-bin is excluded from the linear fit.

Maíz Apellániz and Úbeda (2005) propose an alternative way of binning when dealing with stellar luminosity and initial mass functions (IMF). Their method is based on choosing variable sized bins with a constant number of stars in each bin. They find that variable sized binning introduces bias-free estimations that are independent from the number of
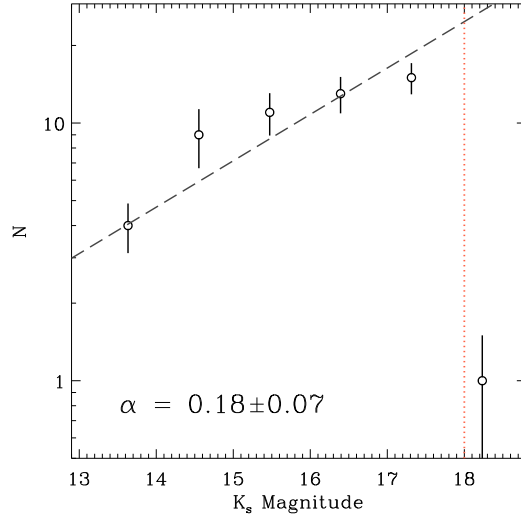
Figure 2.3: *KLF histogram of the stars detected in the central field, derived from the 23 September 2004 data. The dashed line indicates the linear fit of the KLF slope of $\alpha = 0.18 \pm 0.07$. The vertical dotted line (red) represents the current detection limit for faint K_s-magnitudes.*

stars per bin. Their method is applicable to small samples of stars. I apply their method to our KLF calculation and get $d(\log(N)/\delta K_s)/d(K_s) = 0.12 \pm 0.09$, consistent with the fixed sized binning method.

The Diffuse NIR Background

The methods I used in NS10 to correct for the flux density contribution of the stars in the central $2''$ have revealed a faint extended emission around Sgr A* (NS10 Figures 3b, 4b and 5). I detected ~ 1.3 mJy (obtained by correcting the ~ 2 mJy we quote in NS10 for the $A_{K_s} = 2.46$ I use here) at the center of the S-star cluster. With a radius of $1''$ (about twice the FWHM of the S-star cluster) for the Point Spread Function (PSF) used for the subtraction, we showed that a misplacement of the PSF for about only five stars, located within one FWHM of Sgr A*, would contribute significantly to the measured flux at the center. For a median brightness of about 1.3 mJy for these stars, a 1 pixel ~ 13 mas positional shift of each of these stars towards Sgr A* would be required to explain all the detected ~ 1.3 mJy at the center i.e. 0.26 mJy from each star. In Sabha *et al.* (2011) I showed that a displacement larger than a few tenths of a pixel would result in a clear and identifiable characteristic plus/minus pattern in the residual flux distribution along the shift direction. For a maximum positional uncertainty of 1 pixel, I showed that the independent shifts of the five stars can be approximated by a single star experiencing five shifts in a random walk pattern. This resulted in calculating a total maximum contribution of 0.26 mJy from all the five stars to the center, which translates to about 20–30% of the flux density. Thus, more than two thirds of the extended emission detected towards Sgr A* could be due to faint stars, at or beyond the completeness limit reached in the KLF, and associated with the ~ 0.5–$1''$ diameter S-star cluster.
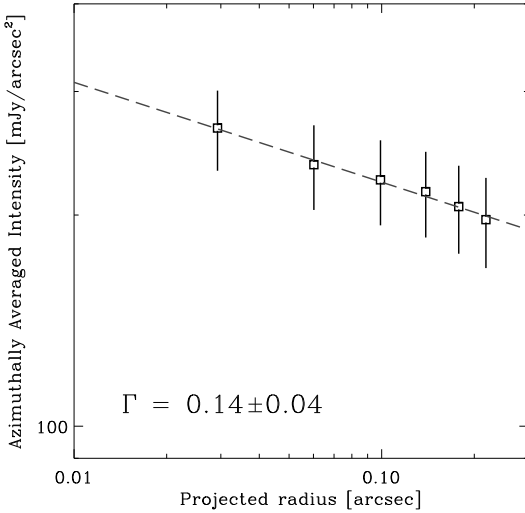
Figure 2.4: *Azimuthal average of the diffuse background emission as derived from manual PSF subtracted 23 September 2004 image. The squares (mean flux and 1σ uncertainty per pixel) have been calculated in annuli of 39.8 mas (3 pixels) width. The black dashed line marks a fit to the data points with an exponential decrease of 0.14.*

The diffuse background emission I detect (see Fig. 2.1a) could be compared to the projected distribution of stars $\Sigma(R) \propto R^{-\Gamma}$, with R being the projected radius. I found that the distribution of the azimuthally averaged residual diffuse background emission, centered on the position of Sgr A*, not to be uniform but in fact decreases gently as a function of radius (see Figure 7 in NS10) with a power-law index $\Gamma_{\mathrm{diffuse}} = 0.20 \pm 0.05$. In this investigation I re-calculate the azimuthally averaged background light from the iterative PSF subtracted image alone. The azimuthally averaged background light is plotted as a function of projected radius from Sgr A* in Fig. 2.4. In this new calculation I find the power-law index to have a value of $\Gamma_{\mathrm{diffuse}} = 0.14 \pm 0.07$. Both results are consistent with recent investigations concerning the distribution of number density counts of the stellar populations in the central arcseconds, derived from imaging VLT and Keck data. For the central few arcseconds Buchholz *et al.* (2009), Do *et al.* (2009) and Bartko *et al.* (2010) find a $\Gamma \sim 1.5 \pm 0.2$ for the young stars, but an even shallower distribution for the late-type (old) stars with $\Gamma \sim 0.2 \pm 0.1$. A detailed discussion concerning the different populations and their distribution is given in Genzel *et al.* (2003); Schödel *et al.* (2007); Buchholz *et al.* (2009); Do *et al.* (2009) and Bartko *et al.* (2010).

The small value I obtain for the projected diffuse light exponent $\Gamma_{\mathrm{diffuse}}$ and the high degree of completeness reached around $K_s = 17.5$, makes this data set well suited for analyzing the diffuse background light. Especially in investigating the role of much fainter stars, beyond the completeness limit, in the observed power-law behavior of the background.

Extrapolating the KLF of the S-star Cluster

Motivated by the power-law behavior of the diffuse background emission and assuming that the drop in the KLF counts at magnitude ~ 18 is caused only by the fact that we have reached the detection limit, I extrapolate the KLF to fainter magnitudes in order to investigate how these faint stars contribute to the background light. The true shape of the luminosity function for K_s-magnitudes below the completeness limit of ~ 17.5 has yet to be determined. Investigations into the IMF of the S-cluster have shown that it can be fitted with a standard Salpeter/Kroupa IMF of $dN/dm \propto m^{-2.3}$ and continuous star formation histories with moderate ages (below 60 Myr, Bartko *et al.*, 2010). Here, I estimate an upper limit on the stellar light by assuming that the KLF exhibits the same behavior observed for brighter magnitudes without suffering a break in the slope toward the fainter end.

I use the KLF slope obtained for the innermost central region, 0.18 ± 0.07 (Fig. 2.3) and extrapolate it over five magnitudes bins to $K_s \sim 25$. The K_s-magnitude bins between 18–25 (translating to stellar masses in the range of ~ 1.68 to 0.34 $M_\odot$) correspond to the brightness of the expected main-sequence stars (luminosity class V) which are likely to be present in the central cluster. However, I assume that due to mass segregation effects in the Galactic nucleus (Bahcall and Wolf, 1976; Alexander, 2005), driven by dynamical friction (Chandrasekhar, 1943) between stars, the heavier objects sink towards the center while the lighter objects move out. Their volume density will be significantly reduced and they may even be expelled from the very center. Freitag *et al.* (2006) show that the main-sequence stars begin to be expelled outward by the cusp of stellar-mass black holes (SBH) after a few Gyrs, just shorter than the presumed age of the stellar cluster at about 10 Gyrs. While the reservoir of lower mass stars may be replenished by the most recent - possibly still ongoing - star formation episode about 6 million years ago (Paumard *et al.*, 2006), I assume that stars well below the low mass limit of ~ 0.34 $M_\odot$ with K_s-band brightnesses around $K_s = 25$ are affected by depletion.

Figure 2.5 shows the KLF slope of $\alpha = 0.18$ and the upper limit imposed by the uncertainty in the fit ($\alpha = 0.25$) plotted as dashed and dash-dotted lines, respectively. The extrapolated K_s-bins are shown as hollow circles. I adopt a Monte Carlo approach for calculating the number of stars N from the KLF, taking into account the uncertainty in the slope. After 10^5 trials I find as a result for each bin, the median number N and median deviation dN.

Using the extrapolated K_s-magnitudes, the corresponding flux densities are calculated using the following relation

$$f_{\text{new star}} = f_{S2} \times 10^{-0.4 \, (K_{\text{new star}} - K_{S2})} \, , \tag{2.1}$$
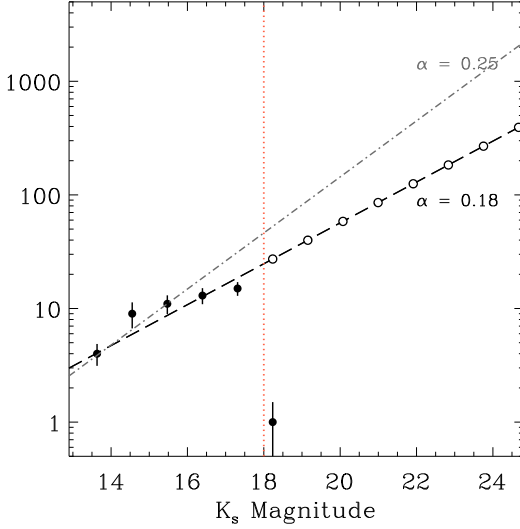
Figure 2.5: *Extrapolation of the KLF power-law fit. The KLF slope of α = 0.18 and the upper limit imposed by the uncertainty in the fit (α = 0.25) are plotted as dashed and dash-dotted lines, respectively. The black filled circles represent the data while the hollow circles represent new points based on the extrapolated KLF slope. The approximate location of the detection limit is indicated by the vertical dotted/red line.*

where $f_{\text{new star}}$ and $K_{\text{new star}}$ are the flux density and K_s-magnitude for each new star in the extrapolation. The flux and magnitude for the star S2 were adopted from NS10, Table 3, and corrected for the extinction value I use here (see § 2.2). The new values are $f_{S2} = 14.73$ mJy and $K_{S2} = 14.1$. The accumulative flux density for each K_s-bin f_{bin} is obtained via

$$f_{\text{bin}} = f_{\text{new star}} \times N_{\text{new star}}. \tag{2.2}$$

The number of stars per bin $N_{\text{new star}}$ is randomly picked from the interval between $[N_{\text{new star}} - dN_{\text{new star}}]$ and $[N_{\text{new star}} + dN_{\text{new star}}]$. In 10^5 trials the accumulative flux per bin and its uncertainty are determined as the median and median deviation of the randomly drawn fluxes f_{bin}. I then add up all the accumulative flux densities for all the new K_s-band bins and obtain the integrated brightness of the extrapolated part of the S-star cluster,

$$F_{\text{Extra Stars}} = \sum_{K_s \simeq 18}^{25} f_{\text{bin}} = (25.72 \pm 14.31) \quad \text{mJy}. \tag{2.3}$$

I assume that the faint, undetectable stars follow the distribution of the azimuthally averaged background light, as shown in Fig. 2.4. Thus, the light from the faint stars that I introduced in the 0.69″ radius region can be compared to the measured background light from our data for the same region. This is achieved by using the total flux density $F_{\text{Extra Stars}}$ to derive the peak light density ($I_{\text{Extra Stars}}$) that would be measured inside one resolution

Figure 2.6: *Relative azimuthally averaged light density, for the background light taken from the observations and the extra stellar light calculated from the extrapolation, plotted as a function of distance from Sgr A*. They are represented by a dotted line with circles (black) and dashed lines with squares (blue), respectively. The stellar light density is normalized to the peak light density of the background at the central resolution element. The upper limit of the extrapolated extra stellar light is shown as the blue dashed line with no symbols.*
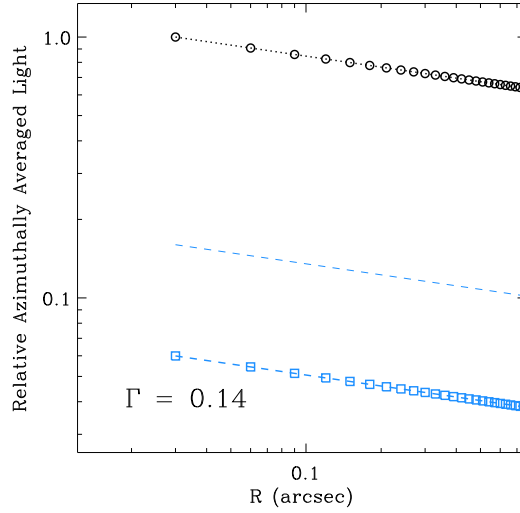
element of $0.033''$ radius centered on the position of Sgr A*, using the following relation:

$$F_{\text{Extra Stars}} \quad = \quad \int f(r,\phi) r \, dr \, d\phi$$

$$= \quad 2\pi I_{\text{Extra Stars}} \int_{0.033''}^{0.690''} r^{1-\Gamma} dr, \tag{2.4}$$

with $\Gamma = \Gamma_{\text{diffuse}} = 0.14$ (see § 2.3). The peak light density for the extra stars is then $I_{\text{Extra Stars}} = (15.24 \pm 8.48)$ mJy arcsec^{-2}. To compare the light caused by the extra stars with the measured background emission, I plot the stellar light density caused by my new stars with the azimuthally averaged measured light density of the background (Fig. 2.6). For illustration purposes I normalize the observed peak stellar light to the measured background value within the central resolution element, $I_{\text{Background}} = (254.30 \pm 58.45)$ mJy arcsec^{-2}. It is clear that the peak light introduced by the new faint stars, as calculated from the extrapolation of the 0.18 ± 0.07 KLF slope, is very small and below that of the background. The dotted line (black circles) represents the background light while the dashed line (blue squares) corresponds to the extra stellar light. The upper limit of the extrapolated extra stellar light contribution is presented as a dashed line with no symbols. The figure shows that the upper limit of the extrapolated light contribution of the S-star cluster is lower than 15% of the measured background light.

Observational Limits on the Stellar Light and Mass

My analysis shows that if there was a population of very faint stars, following the extrapolated K_s-band luminosity function and central cluster profile obtained for the brighter

stellar population (less than $K_s = 18$), the additional stellar light and mass lie well below the limits given by observational data. See following sections and Figs. 2.7 and 2.8.

Limits on the Stellar light

Following the previous calculations and the result displayed in Fig. 2.6, I perform the same analysis for a range of KLF slopes in order to test if the observed background light can be solely obtained by the emission of faint stars. The range of KLF slopes I use is based on the values and uncertainty estimates of the following published KLF slopes for the central 2″: 0.13 ± 0.02 (Buchholz *et al.*, 2009, early-type stars), 0.27 ± 0.03 (Buchholz *et al.*, 2009, late-type stars), 0.21 ± 0.02 (Buchholz *et al.*, 2009, all stars) and 0.30 ± 0.1 (NS10), in addition to the improved newly fitted slope of the KLF in this work 0.18 ± 0.07.

I extrapolate each KLF slope to a K_s-magnitude of $\simeq 25$. The peak light density ($I_{\text{Extra Stars}}$) is calculated using Eq. (2.4). The peak light density of the extra stars is plotted for the extrapolated KLF slopes in the range of 0.11 to 0.40 in Fig. 2.7 . The limit imposed by the peak light density of the measured background light (Fig. 2.1) is plotted as a horizontal dashed line (blue). In addition, the KLF slopes derived in this work and by NS10 and Buchholz *et al.* (2009) are plotted as purple, yellow and green data points, respectively. Figure 2.7 clearly shows that almost all of the KLF slopes result in a peak light density below the observed limit, except for very high slopes > 0.37 which are not in agreement with the observations.

Limits on the Stellar Mass

Using the same range of KLF slopes, I estimate the mass that would be introduced to the central region as a result of the KLF extrapolation. I obtain the stellar mass corresponding to the extrapolated K_s-bins by calculating their luminosity via

$$L_{K_s} = 10^{-0.4(M_{K_s} - M_{\odot K_s})} L_{\odot K_s},\qquad(2.5)$$

where, L_{K_s} and M_{K_s} are the luminosity of a star and its absolute magnitude in K_s-band, respectively. $L_{\odot K_s}$ & $M_{\odot K_s}$ are the K_s luminosity and absolute magnitude of the Sun. Then, the mass for each K_s magnitude is calculated using

$$m = (L_{K_s})^{(1/4)}\qquad(2.6)$$

from Duric (2004); Salaris and Cassisi (2005). For example, a K_s-magnitude around 20 corresponds to 1 $M_\odot$ main-sequence stars of F0V, G0V, K5V spectral types.

In Fig. 2.8 I show the estimated extra mass for all the KLF slopes in units of solar mass. The figure also shows, as dash-dotted/red line , the upper limit for an extended mass enclosed by the orbit of the star S2, calculated by Mouawad *et al.* (2005), where they use non-Keplerian fitting of the orbit to derive the upper limits, assuming that the composition of the dark mass is sources with $M/L \sim 2$. The dotted/gray line represents the tighter
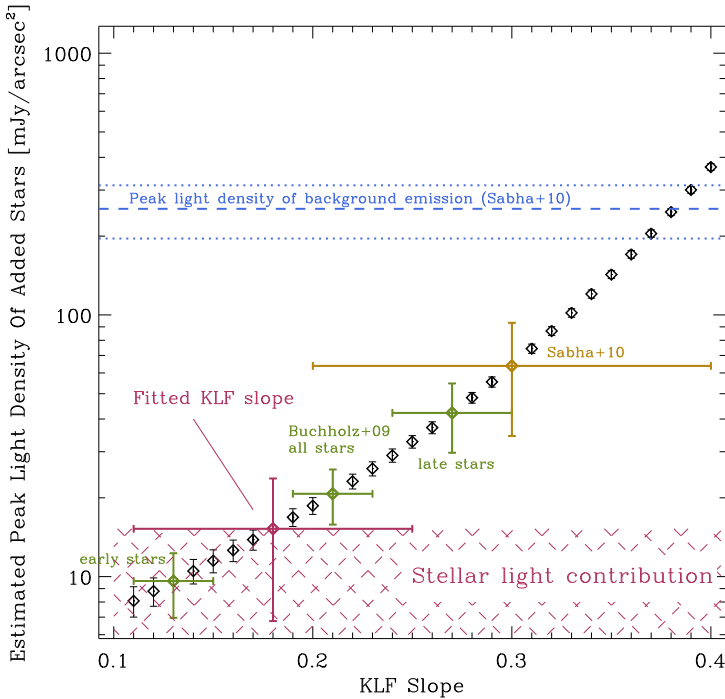
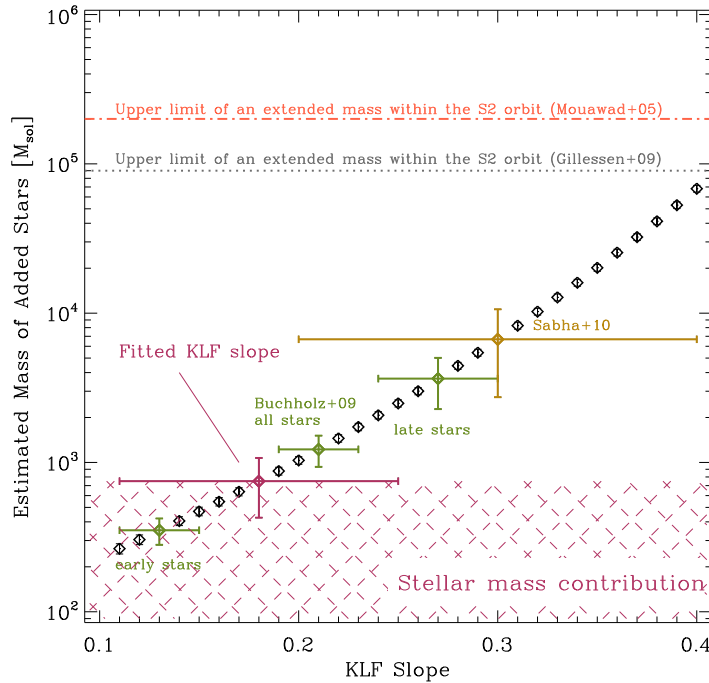**Figure 2.7:** *Estimated peak light density from stars derived from for different KLF slopes. Slopes of* Buchholz *et al.* *(2009) (for different stellar populations) are shown in green, NS10 in yellow and the KLF slope derived here, in § 2.3, in purple. A limit imposed by the measured peak light density from the measured background light is plotted as a horizontal dashed line (blue).*

upper limit obtained later by Gillessen *et al.* (2009a) who derive the mass using recent orbital parameters of S2. They assume that the extended mass consists of stellar black holes (Freitag *et al.*, 2006) with a mass of 10 $M_\odot$ using estimations from Timmes *et al.* (1996) and Alexander (2007). It can be concluded from the figure that the introduced stellar mass, within a radius of ~ 0.69″, lies well below the upper limits imposed by the S2 orbit with a semi-major axis of ~ 0.123″ (Gillessen *et al.*, 2009a). See Fig. 2.1 (right) for a comparison of the sizes of the two regions.

2.4   Dynamical Probes of the Distributed Mass

If the gravitational force near Sgr A* includes contributions from bodies other than the SMBH, the orbits of test stars, including S2, will deviate from Keplerian ellipses. These deviations can be used to constrain the amount of distributed mass near Sgr A* (Mouawad *et al.*, 2005; Gillessen *et al.*, 2009a). But they can also be used to constrain the "granularity" of the perturbing potential, since the nature and magnitude of the orbital deviations

Figure 2.8: *Estimated stellar mass from the added stars for different KLF slopes. Slopes of Buchholz* et al. *(2009) (for different stellar populations) are shown in green, NS10 in yellow and our fitted slope in purple. A limit imposed by the enclosed mass within the S2 orbit is plotted as horizontal dotted (gray) and dash-dotted (red) lines from Gillessen* et al. *(2009a) and Mouawad* et al. *(2005), respectively.*

depend both on the total mass of the perturbing stars, and on their individual masses.

Investigations of a single scattering event were explored by Gualandris *et al.* (2010) using high-accuracy N-body simulations and orbital fitting techniques. They found that an IMBH more massive than $10^3 \, M_\odot$, with a distance comparable to that of the S-stars, will cause perturbations of the orbit of S2 that can be observed after the next peribothron[1] passage of S2. Here we examine the effect many scatterers (i.e. smaller masses for the scatterers but shorter impact parameters) will have on the trajectory of the star S2 as it orbits. Around Sgr A*, the stars and scatterers are moving in a potential well that is dominated by the mass of the central SMBH. In this case the encounters are of a correlated nature and hence cannot be considered as random events.

An important deviation from Keplerian motion occurs as a result of relativistic correc-

---

[1]Peri- or apobothron is the term used for peri- or apoapsis for an elliptical orbit with a black hole present at the appropriate focus.

tions to the equations of motion, which to lowest order predict an advance of the argument of peribothron, ω, each orbital period of

$$(\Delta\omega)_{\mathrm{GR}} = \frac{6\pi G M_\bullet}{c^2 a(1 - e^2)}. \tag{2.7}$$

Setting $a = 5.0$ mpc and $e = 0.88$ for the semi-major axis and eccentricity of S2, respectively, and assuming $M_\bullet = 4.0 \times 10^6 \, M_\odot$,

$$(\Delta\omega)_{\mathrm{GR}} \approx 10.8'. \tag{2.8}$$

The relativistic precession is prograde, and leaves the orientation of the orbital plane unchanged.

The argument of peribothron also experiences an advance each period due to the spherically-symmetric component of the distributed mass. The amplitude of this "mass precession" is

$$(\Delta\omega)_{\mathrm{M}} = -2\pi G_{\mathrm{M}}(e, \gamma)\sqrt{1 - e^2}\left[\frac{M_\star(r < a)}{M_\bullet}\right]. \tag{2.9}$$

Here, $M_\star$ is the distributed mass within a radius $r = a$, and G_{M} is a dimensionless factor of order unity that depends on e and on the power-law index of the density, $\rho \propto r^{-\gamma}$ (Merritt, 2012). In the special case $\gamma = 2$,

$$G_{\mathrm{M}} = \left(1 + \sqrt{1 - e^2}\right)^{-1} \approx 0.68 \text{ for S2} \tag{2.10}$$

so that

$$(\Delta\omega)_{\mathrm{M}} \approx -1.0'\left[\frac{M_\star(r < a)}{10^3 \, \mathrm{M}_\odot}\right]. \tag{2.11}$$

Mass precession is retrograde, i.e., opposite in sense to the relativistic precession.

Since the contribution of relativity to the peribothron advance is determined uniquely by a and e, which are known, a measured $\Delta\omega$ can be used to constrain the mass enclosed within S2's orbit, by subtracting $(\Delta\omega)_{\mathrm{GR}}$ and comparing the result with Eq. (2.11). So far, this technique has yielded only upper limits on $M_\star$ of $\sim 10^{-2} M_\bullet$ (Gillessen *et al.*, 2009a).

The granularity of the distributed mass makes itself felt via the phenomenon of "resonant relaxation" (RR) (Rauch and Tremaine, 1996; Hopman and Alexander, 2006a). On the time scales of interest here, orbits near Sgr A* remain nearly fixed in their orientations, and the perturbing effect of each field star on the motion of a test star (e.g. S2) can be approximated as a torque that is fixed in time, and proportional to m, the mass of the field star. The net effect of the torques from N field stars is to change the angular momentum, **L**, of S2's orbit according to

$$\frac{|\Delta\mathbf{L}|}{L_c} \approx K\sqrt{N}\frac{m}{M_\bullet}\frac{\Delta t}{P} \tag{2.12}$$

where $L_c = \sqrt{GM_\bullet a}$ is the angular momentum of a circular orbit having the same semi-major axis as that of the test star. (Eq. 2.12 describes "coherent resonant relaxation"; on time scales much longer than orbital periods, "incoherent" resonant relaxation causes changes that increase as $\sim \sqrt{\Delta t}$.) The normalizing factor K is difficult to compute from first principles but should be of order unity (Eilon *et al.*, 2009). Changes in **L** imply changes in both the eccentricity, e, of S2's orbit, as well as changes in its orbital plane. The latter can be described in a coordinate-independent way via the angle $\Delta\theta$, where

$$\cos(\Delta\theta) = \frac{\mathbf{L}_1 \cdot \mathbf{L}_2}{L_1 L_2} \tag{2.13}$$

and $\{\mathbf{L}_1, \mathbf{L}_2\}$ are the values of **L** at two times separated by Δt. If we set Δt equal to the orbital period of the test star, the changes in its orbital elements due to RR are expected to be

$$|\Delta e|_{\mathrm{RR}} \quad \approx \quad K_e \sqrt{N} \frac{m}{M_\bullet}, \tag{2.14}$$

$$(\Delta\theta)_{\mathrm{RR}} \quad \approx \quad 2\pi K_t \sqrt{N} \frac{m}{M_\bullet}, \tag{2.15}$$

where N is the number of stars having a-values similar to, or less than, that of the test star and $\{K_e, K_t\}$ are constants which may depend on the properties of the field-star orbits.

Because the changes in S2's orbit due to RR scale differently with m and N than the changes due to the smoothly-distributed mass, both the number and mass of the perturbing objects within S2's orbit can in principle be independently constrained. For instance, one could determine $M_\star = mN$ from Eqs. (2.7) and (2.11) and a measured $\Delta\omega$, then compute $m\sqrt{N}$ by measuring changes in e or θ and comparing with Eqs. (2.14) or (2.15).

We tested the feasibility of this idea using numerical integrations. The models and methods were similar to those described in Merritt *et al.* (2010). The N field stars were selected from a density profile $n(r) \propto r^{-2}$, with semi-major axes extending to $a_{\max} = 8$ mpc. Initial conditions assumed isotropy in the velocity distribution. Two values for the field star masses were considered: $m = 10\ M_\odot$ and $m = 50\ M_\odot$. One of the N-body particles was assigned the observed mass and orbital elements of S2; this particle was begun at apobothron, and the integrations extended for one complete period of S2's orbit. Each of the N field-star orbits were integrated as well, and the integrator included the mutual forces between stars, as well as post-Newtonian corrections to the equations of motion. The quantities $\Delta\omega$, Δe etc. for the S2 particle were computed by applying standard formulae to $(\mathbf{r}, \mathbf{v})$ at the start and end of each integration. 100 random realizations of each initial model were integrated, allowing both the mean values of the changes, and their variance, to be computed.

Figures 2.9 and 2.10a show changes in ω for S2. The median change is well predicted by Eq. (2.11). However, there is a substantial variance. We identify at least two sources for this
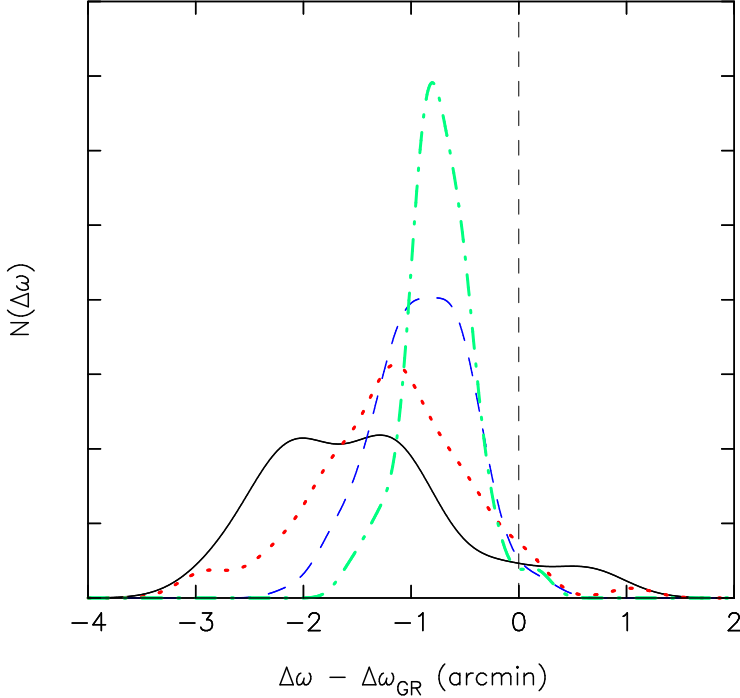
Figure 2.9: *Histograms of the predicted change in S2's argument of peribothron, ω, over the course one orbital period (~ 16 yr). The shift due to relativity, $(\Delta\omega)_{GR} \approx 11'$, has been subtracted from the total; what remains is due to Newtonian perturbations from the field stars. Each histogram was constructed from integrations of 100 random realizations of the same initial model, with field-star mass $m = 10\ M_\odot$, and four different values of the total number: $N = 200$ (solid/black); $N = 100$ (dotted/red); $N = 50$ (dashed/blue); and $N = 25$ (dot-dashed/green). The average value of the peribothron shift increases with increasing Nm, as predicted by Eq. (2.11). The reasons for the spread in $\Delta\omega$ values are discussed in the text.*

variance. (1) The number of stars inside S2's orbit differs from model to model by $\sim \sqrt{N}$, resulting in corresponding changes to the enclosed mass, and hence to the precession rate as given by Eq. (2.11). (2) When N is finite, the same torques that drive resonant relaxation also imply a change in the field star's rate of peribothron advance as compared with Eq. (2.11), which assumes no tangential forces. While the dispersion scales roughly as $\sqrt{N}$, as evident in Fig. 2.9, the fractional change in $\Delta\omega$ due to this effect scales as $\sim 1/\sqrt{N}$ (Merritt *et al.*, 2010). Additional variance might arise from close encounters between field stars and S2, and from the fact that the mass within S2's orbit is changing over the course of the integration due to the orbital motion of each field star.

Whereas the (average) value of $\Delta\omega$ depends only on the mass within S2's orbit, the changes in e and θ depend also on m, as shown in Figs. 2.10b and c. The lines in those
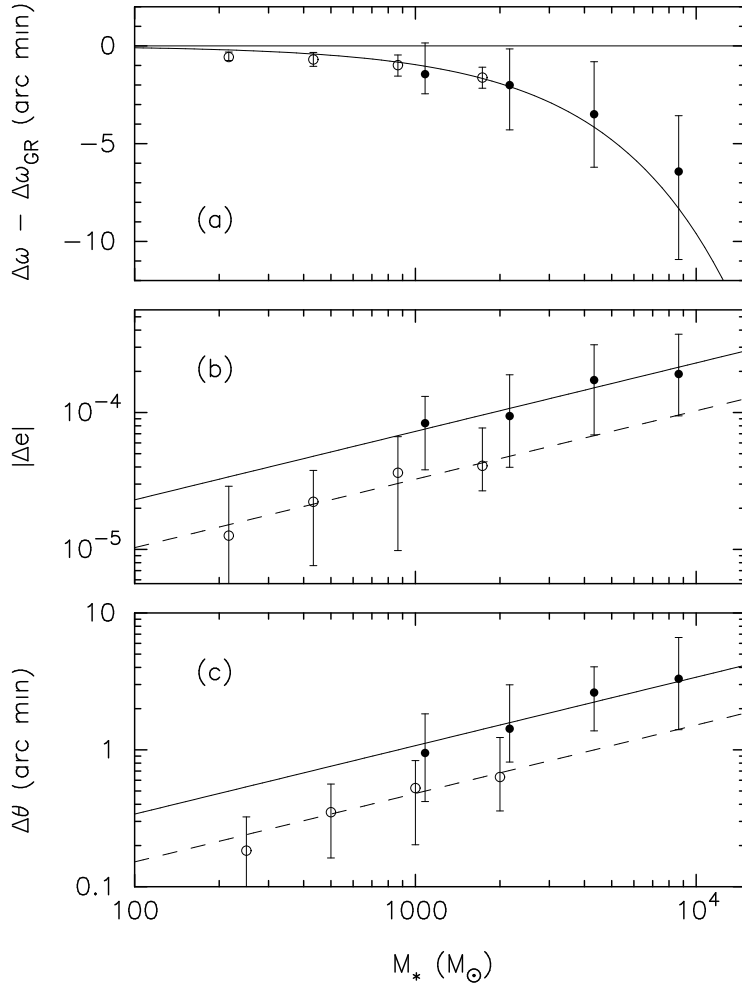
Figure 2.10: *Average values of the changes in ω, e and θ for S2 over one orbital period (∼ 16 yr) in the N-body integrations. Filled circles are from integrations with m = 50 $M_\odot$ and open circles are for m = 10 $M_\odot$; the number of field stars was N = {25, 50, 100, 200} for both values of m. The abscissa is the distributed mass within S2's apobothron, at r ≈ 9.4 mpc. In each frame, the points are median values from the 100 N-body integrations, and the error bars extend from the 20th to the 80th percentile of the distribution. **a**) Changes in the argument of peribothron. The contribution from relativity, Eq. (2.7), has been subtracted. The solid line is Eq. (2.11). **b**) Changes in the eccentricity. Solid and dashed lines are Eq. (2.14), with m = 50 $M_\odot$ and m = 10 $M_\odot$ respectively and with K_e = 1.4. **c**) The angle between initial and final values of **L** for S2. Solid and dashed lines are Eq. (2.15) with K_t = 1.0.*

figures are Eqs. (2.14) and (2.15), with

$$K_e = 1.4, \quad K_t = 1.0.$$

(We have defined N in Eqs. (2.14) and (2.15) as the number of field stars inside a radius of

9.4 mpc, the apobothron of S2.) For a given value of the enclosed mass, $M_\star = Nm$, Fig. 2.10 shows that the changes in e and θ indeed scale as $\sim 1/\sqrt{N}$ or as $\sim \sqrt{m}$, as predicted by Eqs. (2.14) and (2.15).

We can use these results to estimate the changes in ω, e and θ expected for S2, based on theoretical models of the distribution of stars and stellar remnants at the GC. In dynamically evolved models (Freitag et $al.$, 2006; Hopman and Alexander, 2006b), the total distributed mass within S2's apobothron, $r \approx 10$ mpc, is predicted to be $\sim$ a few times 10^3 $M_\odot$. About half of this mass is in the form of main-sequence stars and half in stellar-mass black holes, with a total number $N \approx 10^3$. When there are two mass groups, expressions like Eqs. (2.14) and (2.15) generalize to

$$|\Delta e|_{\text{RR}} \quad = \quad K_e \left[\frac{m_1 \sqrt{N_1} + m_2 \sqrt{N_2}}{M_\bullet} \right] \tag{2.16}$$

$$(\Delta \theta)_{\text{RR}} \quad = \quad 2\pi K_t \left[\frac{m_1 \sqrt{N_1} + m_2 \sqrt{N_2}}{M_\bullet} \right] \tag{2.17}$$

assuming

$$m_1 = 1\,\text{M}_\odot, \quad m_2 = 10\,\text{M}_\odot, \quad N_1 = 10^3, \quad N_2 = 150$$

(Hopman and Alexander, 2006b) we find

$$|\Delta e|_{\text{RR}} \quad \approx \quad 5.4 \times 10^{-5}, \tag{2.18}$$

$$(\Delta \theta)_{\text{RR}} \quad \approx \quad 0'.8, \tag{2.19}$$

$$(\Delta \omega)_{\text{M}} \quad \approx \quad -2.5'. \tag{2.20}$$

For obtaining the dispersion in the value of Eq. (2.20), we scaled the dispersion given in Fig. 2.10a for the single population case, $N = 50, m = 50$ $M_\odot$ of the same total extended mass, to the two populations case we are investigating here. The dispersion obtained from the simulations is $\sim 4'$. We scale it using the relation $\Delta \omega / \sqrt{N}$ in order to account for the SBH and MS populations, independently. The dispersion for the new configuration then becomes $\sim 1.43'$, lower than the single population case. This is attributed to the fact that the number of main-sequence stars is much larger than the stellar-mass black holes, hence they lower the dispersion in the total Newtonian peribothron shift $(\Delta \omega)_{\text{M}}$.

Considering a higher value for the enclosed mass $M_\star = 10^4$ $M_\odot$ while keeping the same mass scales and abundance ratios of the scattering objects,

$$m_1 = 1\,\text{M}_\odot, \quad m_2 = 10\,\text{M}_\odot, \quad N_1 = 4000, N_2 = 600$$

one gets changes of

$$|\Delta e|_{\text{RR}} \quad \approx \quad 1.1 \times 10^{-4}, \tag{2.21}$$

$$(\Delta\theta)_{\text{RR}} \quad \approx \quad 1.7', \tag{2.22}$$

$$(\Delta\omega)_{\text{M}} \quad \approx \quad -10'. \tag{2.23}$$

The dispersion in Eq. (2.23) can be compared, as we did before, to the case considered in the simulations ($N = 200, m = 50\ M_\odot$) by scaling the $\sim 8'$ dispersion (Fig. 2.10a) to become $\sim 2.86'$ for the two mass population.

Repeating the same analysis as before to the $M_\star = 10^5\ M_\odot$ gives the following numbers for the stellar black holes and low-mass stars

$$m_1 = 1\ \text{M}_\odot, \quad m_2 = 10\ \text{M}_\odot, N_1 = 40000, N_2 = 6000$$

that result in

$$|\Delta e|_{\text{RR}} \quad \approx \quad 3.4 \times 10^{-4}, \tag{2.24}$$

$$(\Delta\theta)_{\text{RR}} \quad \approx \quad 5.2', \tag{2.25}$$

$$(\Delta\omega)_{\text{M}} \quad \approx \quad -100'. \tag{2.26}$$

Similar to the above cases, the dispersion in Eq. (2.26) can be compared to the single mass case by scaling the $\sim 25.3'$ dispersion to become $\sim 9.1'$ for the two mass population. The $\sim 25.3'$ value is obtained by scaling with $\Delta\omega/\sqrt{N}$ from the value shown in Fig. 2.10a for the $10^4\ M_\odot$ extended mass.

We would like to stress that making a definite prediction about the N-dependence of the variance is beyond the scope of the current work. However, we have noted that in both cases considered in Fig. 2.10 the relative variance is of the order of unity or larger i.e. the dispersion is of the order of the Newtonian peribothron shift.

The positional uncertainty is currently of the order of 1 mas. For the highly eccentric orbit of S2 this implies that the accuracy with which the peribothron shift can be detected is of the order of 24′. As can be seen for the case of $M_\star = 10^5\ M_\odot$, the shifts are at the limit of the current instrumental capabilities if the total enclosed mass was entirely composed of massive perturbers. The shifts given in Eqs. (2.20) and (2.23) can be measured if the accuracy is improved by at least one order of magnitude using larger telescopes or interferometric methods in the NIR. However, considering the variances in the calculated shifts one would need to observe more than one stellar orbit in order to infer information on the population giving rise to the Newtonian peribothron shift. By comparison, the current uncertainty in S2's eccentricity is ~ 0.003, and uncertainties in the Delaunay angles

i and Ω describing its orbital plane are $\sim 50'$ (Gillessen *et al.*, 2009a). In both cases, an improvement of a factor ~ 50 would be required in order to detect the changes given in e and θ.

Dynamically-relaxed models of the GC have been criticized on the grounds that they predict a steeply-rising density of old stars inside ~ 1 pc, while the observations show a parsec-scale core (Buchholz *et al.*, 2009; Do *et al.*, 2009; Bartko *et al.*, 2010). Dynamically *un*relaxed models imply a much lower density near Sgr A* and an uncertain fraction of stellar-mass black holes (Merritt, 2010; Antonini *et al.*, 2012). The number of perturbers is so small in these models that their effect on the orbital elements of S2 would be undetectable for the foreseeable future, barring a lucky close encounter with S2.

In addition to the small amplitude of the perturbations, the potential difficulty in constraining N and m comes from the nonzero variance of the predicted changes (Fig. 2.10). The variance in $\Delta\omega$ scales as $\sim \Delta\omega/\sqrt{N}$ and would be small in the dynamically-relaxed models with $N \approx 10^3$. Another source of uncertainty comes from the dependence of the amplitude of $\Delta\omega$ on γ (Eq. 2.9), which is unknown. We do not have a good model for predicting the variances in $|\Delta e|$ and $\Delta\theta$, but Fig. 2.10 suggests that the fractional variance in these quantities is not a strong function of N or m, and that it is large enough to essentially obscure changes due to a factor ~ 5 change in m at fixed $M_\star$. On the other hand, considerably more information might be available than just Δe and $\Delta\theta$ for one star; for instance, the full time-dependence of $(\mathbf{r}, \mathbf{v})$ for a number of stars.

Fighting the Limits on the Power of Stellar Orbits

The results from the previous sub-sections clearly show that deriving the net-displacement for an ideal elliptical orbit for a single star will not be sufficient to put firm limits on both the total amount of extended mass and on the nature of the corresponding population. However, the situation may be improved if one studies the statistics of the time and position dependent deviations along a single star's orbit or instead uses the orbits of several stars.

Improving the Single Orbit Case

The actual uncertainty in projected right ascension or declination, $\sigma^2_{\text{position}}$, can be thought of as a combination of several contributions. Here $\sigma^2_{\text{apparent}}$ is the apparent positional variation due to the photo-center variations of the star while it is moving across the sea of fore- and background sources. The scattering process results in a variation of positions described by $\sigma^2_{\text{scattering}}$. Finally, systematic uncertainties due to establishing and applying an astrometric reference frame give a contribution of $\sigma^2_{\text{systematic}}$.

The value of $\sigma^2_{\text{position}}$ can be measured in comparison to the orbital fit. The value of $\sigma^2_{\text{apparent}}$ can be obtained experimentally by placing an artificial star into the imaging

frames at positions along the idealized orbit. A reliable estimate of $\sigma^2_{\mathrm{apparent}}$ is achieved by comparing the known positions at which the star has been placed and the positions measured in the image frames. As for the case of the systematic variations, they can be estimated by investigating sources that are significantly brighter or slower than the S-stars. Finally, the value that describes the scattering process, and therefore gives information on the masses of the scattering sources, can be obtained via

$$\sigma^2_{\mathrm{scattering}} = \sigma^2_{\mathrm{position}} - \sigma^2_{\mathrm{apparent}} - \sigma^2_{\mathrm{systematic}}. \tag{2.27}$$

Alternatively, $\sigma^2_{\mathrm{scattering}}$ could be measured directly by near-infrared interferometry with long baselines. Measuring the position of S2 interferometrically as a function of time with respect to bright reference objects could allow observing the effects of single scattering events. Here the assumption is that they happen infrequently enough such that one can build up sufficient signal to noise on the $\sigma_{\mathrm{scattering}}$ measurement provided that the uncertainties in the interferometric measuring process are sufficiently well known.

Improving by Using Several Stars

If scattering events contribute significantly to the uncertainties in the determination of the orbits, a number of stars may help to derive the physical properties of the medium through which the stars are moving. While the influence of the extended mass imposes a systematic variation of the orbits through the Newtonian peribothron shift, the variations due to scattering events will be random. This implies that for individual stars the effects may partially compensate or amplify each other. Averaging the results of N stars, that will then essentially sample the shape of the distributions shown in Fig. 2.9, may therefore result in an improvement proportional to $N^{-1/2}$ in the determination of the extended mass.

2.5 Simulating the Distribution of Fainter Stars

In NS10 I detected three stars that were either previously not identified at all (NS1 & NS2 stars, Figure 1 in NS10) or only allowed an unsatisfactory identification with previously known members of the cluster (S62, as pointed out in Dodds-Eden *et al.*, 2011). In addition we have the case of the star S3 which was identified in the K_{s}-band in the early epochs 1992 (Eckart and Genzel, 1996), 1995 (Ghez *et al.*, 1998) and lost after about 3 years in 1996/7 (Ghez *et al.*, 1998), 1998 (Genzel *et al.*, 2000). I investigate this phenomenon using my method of extrapolating the KLF in the inner 1–2 arcsec region, surrounding Sgr A*, to stars fainter than the faintest source ($K_{\mathrm{s}} = 17.31$) I detected in our 30 August and 23 September 2004 dataset, in which Sgr A* shows very low activity (NS10). In this section I describe the method I use to simulate the distribution of these faint stars, and the possible false detections that can be caused by the combined light of many stars appearing in projection to be very close to each other, such that they cannot be individually resolved with 8–10 m class telescopes.

The calculations were done by taking all the extra (extrapolated) faint stars in the K_s-magnitude interval of 18 to 25. The stars were then distributed in a 23×23 grid that corresponds to 529 cells. Each cell has the dimensions of $0.06'' \times 0.06''$, i.e. about one angular resolution element in K_s-band, this grid, therefore, simulates observations of the inner $1.38'' \times 1.38''$ projected region surrounding Sgr A*. I distributed the faint stars in the grid such that their radial profile centered on Sgr A* reproduces that of the stellar number density counts of the inner region of the central stellar cluster with a power-law index of $\Gamma = 0.30 \pm 0.05$ from Schödel *et al.* (2007). This way each cell has a specific number of stars that can be inserted into it, with the maximum number of stars being located in the central cell, i.e. the peak of the radial profile. My algorithm fills each cell with its specified number of stars by choosing them randomly from a pool of stars created from the extrapolated KLF. The pool is created such that for each K_s-magnitude bin above ~ 18, a number of stars N get their K_s-band magnitudes according to the KLF. From this pool of stars I then randomly pick objects to fill the cells of the grid such that they obey the power-law radial number density profile. Then, the fluxes of the stars in each individual cell are added up and compared to the value of 0.76 mJy which is the flux density of the faintest stellar source in our S-star cluster data, i.e. $K_s = 17.31$ (NS10).

I ran the simulation 10^4 times in order to get reliable statistical estimates for the brightnesses in each resolution cell. Hence I can estimate how likely it is to find strong apparent clusterings along the line of sight that are brighter than the faintest star I identified in the S-cluster (flux larger than 0.76 mJy).

Taking into account the uncertainties of the quantities that describe the central S-star cluster I repeat the simulation for a combination of three KLF slopes (0.11, 0.18 and 0.25), three radial profile power-law indices ($\Gamma = 0.19$, 0.30 and 0.35) and two K_s-magnitude cutoffs for the extrapolation, 21 and 25 (corresponding to 0.0258 and 0.0009 mJy, respectively). Here the brighter cutoff is very close to the brightness of the faintest stars that have been detected. The choice for the KLF slope satisfies the range of the power-law fit $\Gamma = 0.18 \pm 0.07$. The power-law indices were taken from Table 5 of Schödel *et al.* (2007) for the cusp radial profiles.

The results of the simulations are summarized in Table 2.1. Three different realizations of a cluster simulation as well as the average of 10^4 simulations are shown in Fig. 2.11. I find that for the measured KLF slope of 0.18, a measured power-law index of $\Gamma = 0.3$ and a faint K_s-magnitude cutoff I obtain a false star in about a quarter of all simulations. For steeper KLF and power-law slopes Γ I get this result in more than 70% of all cases independent of the cutoff magnitude.

In Table 2.2 I show the same statistics as in Table 2.1 but for the central cell in the grid, at the projected position of Sgr A*. Also given, in parentheses, is the number of stars in the central cell that gives rise to the detection of a false star at a distance of less than one
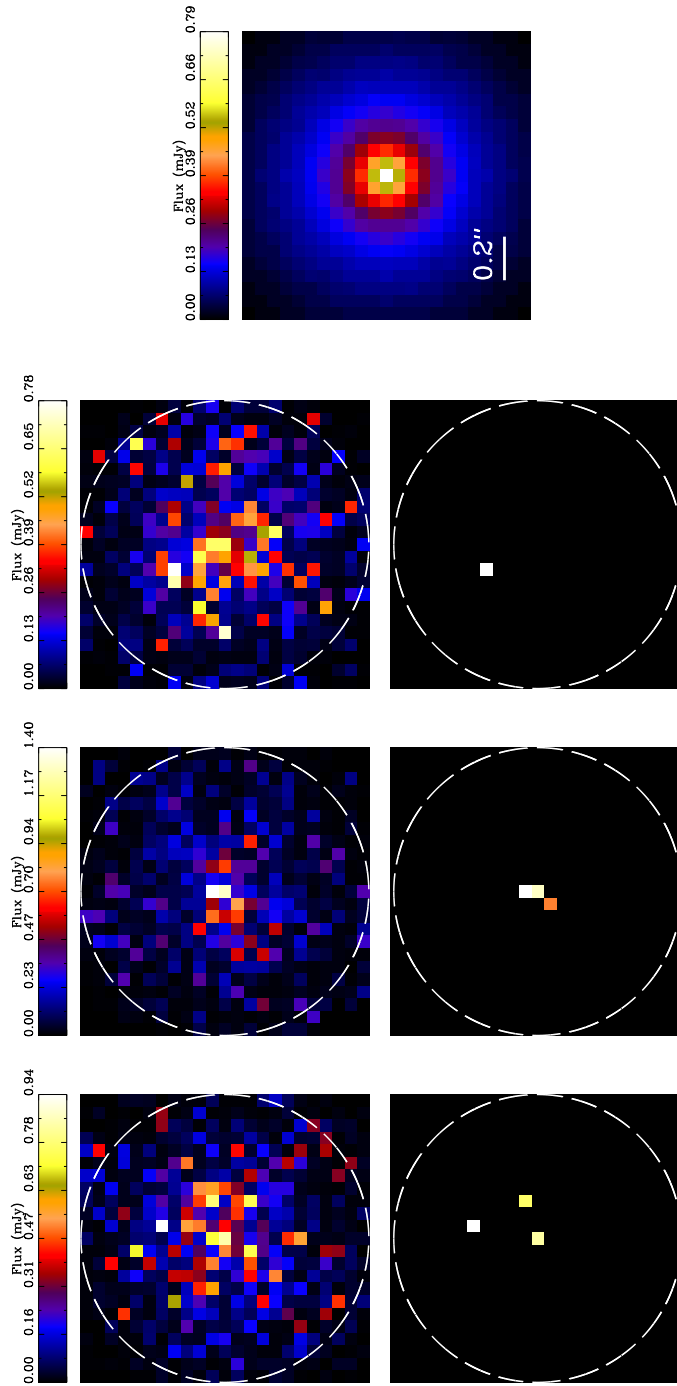
Figure 2.11: *Upper panel: Three different snapshots of the simulation for the 0.25 KLF slope, power-law index $\Gamma = 0.3$ and 24.67 K_s-magnitude cutoff. Lower panel: The same as upper but with only the detectable blend stars visible. Right: Average of all the 10^4 simulation snapshots for the same setup.*

Table 2.1: *Probabilities of detecting a false star (brighter than $K_s = 17.31$) in a $1.38'' \times 1.38''$ region.*

K_s-band magnitude cutoff	Power-law index		
	0.19	0.30	0.35
KLF slope = 0.11			
20.99	0.0000	0.1471	0.1500
24.67	0.0285	0.0292	0.0224
KLF slope = 0.18			
20.99	0.0848	0.1286	0.3016
24.67	0.2058	0.2426	0.2927
KLF slope = 0.25			
20.99	0.7776	0.7442	0.9085
24.67	0.9462	0.9725	0.9802

Table 2.2: *Probabilities of detecting a false star (brighter than $K_s = 17.31$) at the position of Sgr A*. The number of stars contributing to the detected flux of the false star is given in parentheses for each considered case.*

K_s-band magnitude cutoff	Power-law index		
	0.19	0.30	0.35
KLF slope = 0.11			
20.99	0.0000(2)	0.0752(4)	0.0757(4)
24.67	0.0094(6)	0.0103(6)	0.0099(6)
KLF slope = 0.18			
20.99	0.0423(4)	0.0438(4)	0.1181(5)
24.67	0.0345(15)	0.0591(18)	0.0821(20)
KLF slope = 0.25			
20.99	0.3120(8)	0.3149(8)	0.5448(10)
24.67	0.3223(59)	0.4756(70)	0.5291(74)

angular resolution element away from the line of sight to Sgr A*. I find that for a KLF slope of 0.25 I get a false star in 30% to 50% of all simulations, independent of the power-law

index Γ and the cutoff magnitude. This is consistent with the offsets found in different observational epochs of Sgr A* light curves (Witzel *et al.*, 2012; Dodds-Eden *et al.*, 2011). In this case the blend consists of 8 to 74 stars below the unresolved background in the S-star cluster region. For flatter KLF slopes (i.e. 0.11 and 0.18) I find that a blend star only occurs in less than about 10% of all cases, which appears to be well below the upper limit found from observations. For a KLF slope of $\alpha = 0.25$ and a number density power-law index of Γ around 0.3 the total number of stars in the simulated S-star cluster is a few 1000. This is consistent with the number of main-sequence stars assumed by Freitag *et al.* (2006).

I repeat the same simulations as explained above but for a grid of $0.075''$ cell size. This cell size is specific to the resolution achieved in the *K*-band ($1.95 - 2.45\ \mu$m) with SIN-FONI[2] instrument. The results are displayed in Tables 2.3 & 2.4 and Fig. 2.12.

Table 2.3: *Probabilities of detecting a false star (brighter than $K_s = 16.39$), using SINFONI in a $1.28'' \times 1.28''$ region.*

K_s-band magnitude cutoff	Power-law index		
	0.19	0.30	0.35
KLF slope = 0.11			
20.99	0.0510	0.0493	0.0858
24.67	0.0478	0.0722	0.0765
KLF slope = 0.18			
20.99	0.1302	0.1103	0.2897
24.67	0.2224	0.2905	0.4162
KLF slope = 0.25			
20.99	0.5259	0.6160	0.8987
24.67	0.8924	0.9444	0.9518

---

[2]SINFONI is an ESO VLT integral field spectrograph installed at the Cassegrain focus of UT4. It observes in the NIR ($1.1 - 2.45\ \mu$m) assisted by an adaptive optics module.
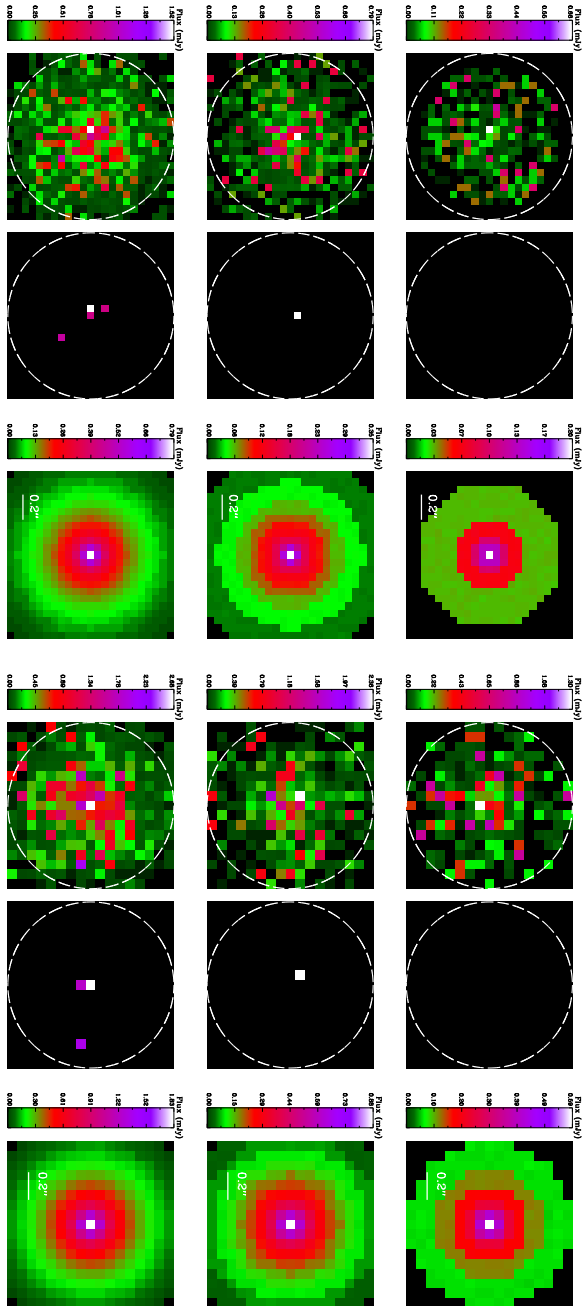
Figure 2.12: *Monte Carlo simulations for two different camera setups that resemble the K$_s$-band for NACO (right) and SINFONI (left) at the VLT.* **Upper** *panel: Snapshot of the simulation for the 0.11 KLF slope, power-law index Γ = 0.3 and 24.67 K$_s$-magnitude cutoff.* **Left***: All stars visible.* **Middle***: Only the detectable blend stars visible.* **Right***: Average of all the 10^4 simulation snapshots for the same setup. Middle & Lower panel: Same as top but for the 0.18 and 0.25 KLF slopes, respectively.*

Table 2.4: *Probabilities of detecting a false star (brighter than $K_s = 16.39$), using SINFONI at the position of Sgr A*. The number of stars contributing to the detected flux of the false star is given in parentheses for each considered case.*

K_s-band magnitude cutoff	Power-law index		
	0.19	0.30	0.35
KLF slope = 0.11			
20.99	0.0250(4)	0.0246(4)	0.0612(5)
24.67	0.0119(8)	0.0214(10)	0.0271(11)
KLF slope = 0.18			
20.99	0.0504(6)	0.0522(6)	0.1502(8)
24.67	0.0491(25)	0.0769(29)	0.1290(35)
KLF slope = 0.25			
20.99	0.1468(10)	0.2507(12)	0.5111(16)
24.67	0.3208(98)	0.4761(115)	0.5193(122)

2.6   Summary and Conclusion

By determining the KLF of the S-star cluster members from infrared imaging, using the distribution of the diffuse background light and the stellar number density counts, we have been able to shed some light on the amount and nature of the stellar and dark mass associated with the cluster of high velocity S-stars in the immediate vicinity of Sgr A*.

The amount of light from the fainter S-cluster members is below the amount of residual light after removing the bright cluster members. One implication could be that both the diffuse light and dark mass are overestimated. However, while NS10 estimate that only a maximum of one third of the diffuse light could be due to residuals from the PSF subtraction, I find that faint stars at or beyond the completeness limit reached in the KLF can account only for about 15% of the background light. Additional light may also originate from accretion processes onto a large number of 10 $M_\odot$ black holes that may reside in the central region, covered by the S-stars. I find that the stellar mass derived from the KLF extrapolation is much smaller than the amount of mass that may be present considering the uncertainties in the orbital motion of the star S2. Higher angular resolution and sensitivity are needed to resolve the background light and analyze its origin.

By investigating the effects of orbital torques due to resonant relaxation, we find that if a significant population of 10 $M_\odot$ black holes is present, with enclosed masses between

10^3 $M_\odot$ and 10^5 $M_\odot$ (see e.g. Freitag *et al.*, 2006), then for trajectories of S2-like stars, contributions from scattering will be important compared to the relativistic or Newtonian peribothron shifts. This clearly shows that observing a single stellar orbit will not be sufficient to put firm limits on the total amount of extended mass and on the importance of relativistic peribothron shift. In this case only the observation of a larger number of stars will allow to sample the statistics of the effect, i.e. the distributions in Fig. 2.9. However, if the distribution of 10 $M_\odot$ black holes is cuspy then this may become even more difficult (and close encounters should be frequent in this region).

In general, the inclusion of star-star perturbations allows us to probe the distribution and composition of mass very close to the SMBH simultaneously, if the astrometric accuracy can be improved by an order of magnitude by using either larger telescopes or interferometers in the NIR.

With measurements and extrapolations of the S-star cluster KLF slope, and number density counts with assumptions on the KLF cutoff magnitude, I can show that the contamination for the members of the cluster, and especially at the position of Sgr A*, by blend stars is fully consistent with measurements. I show that for 8–10 m class telescopes the presence and proper motion of faint stars close to the confusion limit in the region of the S-star cluster is highly contaminated by blend stars. Due to the 2-dimensional velocity dispersion of the stars within the S-star cluster of about 600 km/s the blend stars will last for about 3–4 years before they fade and dissolve. Close to the center, I find the probability of detecting blend stars at any time is about 30–50%. At the central position the change from the appearance of a blend star to the appearance of another may also give the illusion of high proper motions for 8–10 m class telescopes. Such a prime example would be S3, detected close to the position of Sgr A*, which had both a limited lifetime and high proper motion (Eckart and Genzel, 1996; Ghez *et al.*, 1998; Genzel *et al.*, 2000). Blending of sources along the line of sight may also severely contaminate the proper motion measurements of individual stars close to the confusion limit. Only with the help of proper motion measurements over time significantly longer than 3 years one will be able to derive reliable orbital parameters for a single star. Also, spectroscopy may help to resolve blend stars, however, the objects are faint and spectroscopy will be difficult.

These findings clearly demonstrate the necessity of higher angular resolution, astrometric accuracy and point source sensitivity for future investigations of the S-star cluster. They would also greatly improve the derivation of the amount and the compactness of the central mass as well as the determination of relativistic effects in the vicinity of Sagittarius A*.

The work presented in this chapter is published in Sabha, Eckart, Merritt, Zamaninasab, Witzel, García-Marín, Jalali, Valencia-S., Yazici, Buchholz, Shahzamanian, Rauch, Horrobin, and Straubmeier (2012). Also, Eckart *et al.* (2012); Sabha *et al.* (2015).

MID INFRARED MAPPING OF THE CENTRAL CLUSTERS

The Galactic Center is one of the targets planned to be observed with the MIRI instrument aboard the James Webb Space Telescope (JWST). Here I report part of the "pathfinder" observations we obtained with the ground-based instrument VISIR. The value of these new observations lies in the fact that they are the first and only data that cover a large field of view of selected regions within the central tens of parsecs of the Galaxy, with spatial resolutions better than Spitzer survey data. The spectral indices of the compact sources detected in our multi-band observations will aid in the identification of massive young stellar objects, and will allow the tracing of their spatial distribution and concentration. When combined with the current multi-wavelength surveys and future MIRI observations it will enable us to trace and draw a better picture of the past 8 Myr of cluster based star formation in the Galactic Center.

3.1   Introduction & Motivation

In 2018 the *James Webb Space Telescope*[1] (JWST) is expected to be launched and sent on its way to its new permanent home, the second Lagrange point (L2) of the Sun-Earth system. There the telescope shield will effectively prevent the heating of its components from the radiation of the Sun, Earth and Moon. This setup is essential to keep the telescope cold as it is designed to observe faint and distant objects in the infrared. One of the three

---

[1] http://www.jwst.nasa.gov

instruments that will be mounted on JWST is the *Mid-Infrared Instrument* (MIRI) which will provide imaging, spectroscopy and coronagraphy in the 5–18 μm wavelength regime. MIRI is an international (50/50) partnership between JPL (*Jet Propulsion Laboratory*) and a nationally funded consortium of European institutes, working with ESA (*European Space Agency*) and NASA (*National Aeronautics and Space Administration*).

The instrument's main target of interest is observing the red-shifted light of distant galaxies, newly forming stars, and faint objects in the solar system. The high sensitivity of the instrument makes it difficult to observe the bright structures at the Center: the Nuclear Stellar Cluster (NSC), the Arches and Quintuplet cluster as well as some filaments nearby. However, faint objects and filaments within and near these clusters can be observed using the MRS (*Medium Resolution Spectrometer*) integral field units (IFUs) but they require high pointing accuracy and accurate positional information of these targets in order to avoid placing the IFUs on the bright objects. For this reason, large field of view (FOV) high spatial resolution mid-infrared (MIR) observations are required for these regions in order to map the exact positions of the interesting targets.

The Galactic Center (GC) is particularly interesting for studying star formation as the environmental factors there are quite extreme. Even though the cloud density, velocity dispersion, magnetic field strength, and metallicity are all large there (Morris, 1993), stars do form in the Center. In fact, the star formation activity today may be characteristic of the entire history of the central 100 pc (Serabyn and Morris, 1996). For example, a molecular clump has been identified recently (60 pc from Sgr A*) as a progenitor of Arches-like clusters (Longmore *et al.*, 2012). In the central few hundred parsecs one finds three compact, massive and young clusters (see Fig. 1.2 in Chapter 1): the central stellar cluster containing the supermassive black hole (SMBH) Sgr A* and two others located about 30 pc away in projection, the Quintuplet and the Arches cluster (Morris and Serabyn, 1996; Figer *et al.*, 1999c; Serabyn *et al.*, 1998, and references therein).

These clusters, which occupy the low-mass end of the range of "super star clusters" (Ho and Filippenko, 1996), are among the most massive in the Galaxy, accounting for a good fraction of the total star formation near the GC. With the estimated cluster/starburst ages, these three clusters allow us to study the star formation history in clusters over the past 8 Myrs. The Arches cluster covers the past 2-3 Myr, the Quintuplet cluster the past 4-5 Myr, and the central stellar cluster that harbors Sgr A* covers mainly the past 6-8 Myr. Stolte *et al.* (2002, 2008) estimate the Arches cluster's mass to be ~ 10^4 M$_\odot$. It consists of O and WR stars (Nagata *et al.*, 1995; Cotera *et al.*, 1996). The age of the cluster is about 2.5 Myr (Figer *et al.*, 2002). Stellar disk candidates are found as reddened proper motion members with some stellar disk candidates showing CO-bandhead lines in their 2.3 μm emission (Stolte *et al.*, 2008, 2010). Other interesting regions are the Arched Filaments and the Sickle, as they are most likely excited by the nearby young and luminous stars of the Arches and Quintuplet clusters (Simpson *et al.*, 2007).
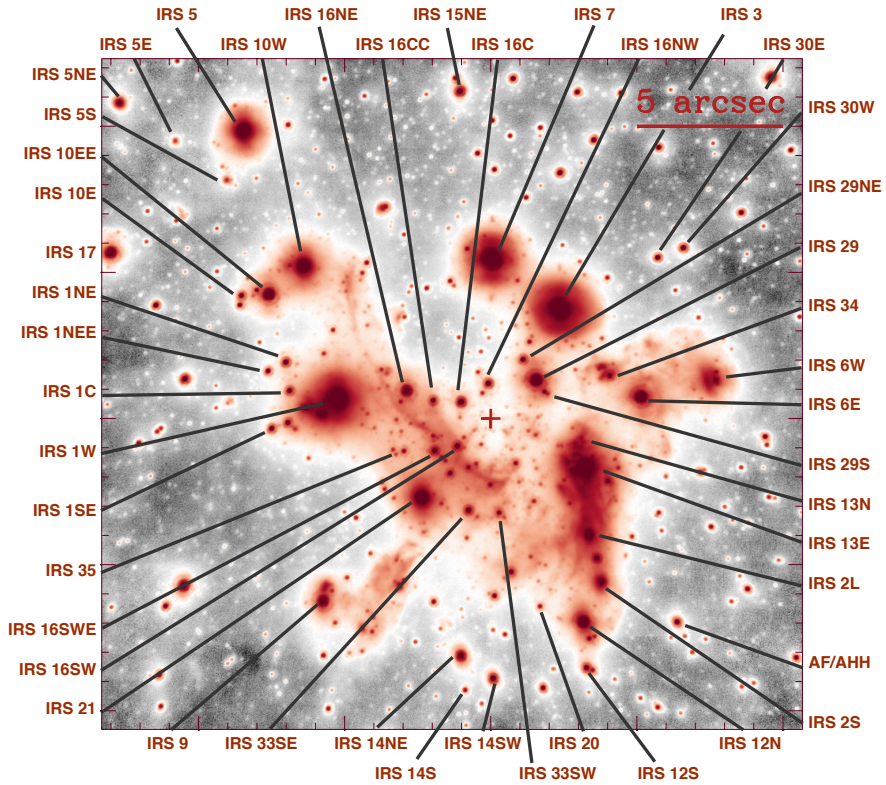
Figure 3.1: *Same as Fig. 1.5, L′-band (3.8 μm) mosaic of the Galactic Center stellar cluster obtained with VLT NaCo in 2012. Most sources are identified based on Viehmann et al. (2005). One arcsec translates to ~0.04 pc for an 8 kpc distance to the GC. The supermassive black hole Sagittarius A* (Sgr A*) position is marked by a cross. North is up and east is to the left.*
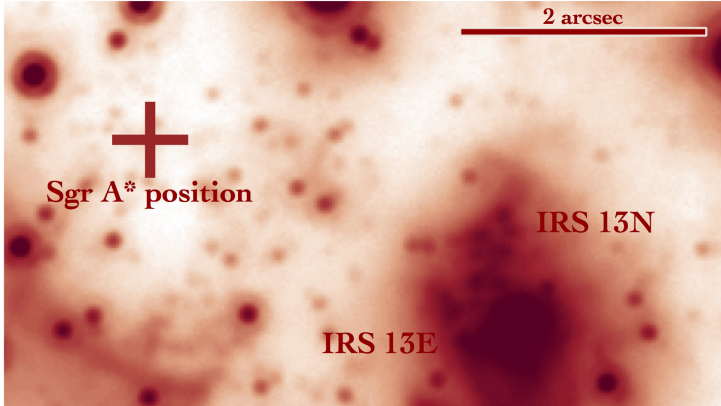
Figure 3.2: *L'-band (3.8 µm) image from the same 2012 data set as Fig. 3.1. IRS 13N & IRS 13E association of stars are labeled. The position of the SMBH, Sgr A*, is marked. North is up and east is to the left.*

There are several lines of observational evidence for the presence of young stars in the NSC. It is, however, still unclear how they came to form there. IRS 16 is one cluster of young (~1 Myr) He-stars (Fig. 3.1). IRS 13E, an extremely dense stellar association located ~3.2" from Sgr A*, is also young and contains several Wolf-Rayet (WR) and O-type stars, about four of which show a common velocity. A distance 0.5" to the north of IRS 13E, there is a complex of extremely red sources referred to as IRS 13N (see Fig. 3.2). It is an association of co-moving sources that are believed to be the best candidates for young (recently formed) stellar objects (YSOs) in the central cluster. Their ages are estimated to be <1 Myr for a co-moving and dynamically young group of Herbig Ae/Be stars, as inferred from photometric and spectroscopic analysis (Eckart *et al.*, 2013, 2004; Mužić *et al.*, 2008). Similarly, the compact mid-infrared (MIR) sources located east of IRS 5 and the northern arm of the mini-spiral are also considered to be young stellar candidates (Perger *et al.*, 2008) and/or low luminosity versions of the brighter bow-shock sources (Tanner *et al.*, 2002, 2005).

This chapter starts with the details of the MIR observations I used. In Sect. 3.3, I describe the data reduction and flux calibration process implemented toward getting the final mosaics. Section 3.4 presents and discusses the results I get from the initial analysis of the data, for both the central stellar cluster and the Quintuplet cluster. I summarize and discuss the implications of my results in Section 3.5.

3.2 Observations

The MIR imaging data used in this work were obtained as part of the larger program ProgId:085.C-0047 designed to map five GC targets in preparation for future MIRI observations (see Sect. 3.1). After performing basic data reduction steps for all the datasets, I

inspected the resulting mosaics and performed an initial point source detection. The sub-set of datasets I report here were the ones that yielded reliable flux density estimates. The remaining sets had either very bad weather conditions during the observations or contained only a few compact sources that were too faint to obtain a reliable estimate of their flux densities.

The observations I report here were performed on the nights of 10th, 11th, and 12th of September 2010 at the ESO VLT, using the MIR camera VISIR (Lagage *et al.*, 2004). We used the *N*-band *PAH*1 filter, with a central wavelength of 8.59 μm and a half-band width of 0.42 μm, and the *NeII$_2$* filter, with a central wavelength of 13.04 μm and a half-band width of 0.22 μm. The pixel scale was 0.127$''$ per pixel (intermediate field, IF) and the observations were designed to cover a $\sim 74'' \times 74''$ region centered on the position of Sgr A*, for the NSC, and on the position of the Pistol Nebula for the Quintuplet cluster. The resulting large field of view (FOV) was obtained from 10 snapshots each with a $\sim 32.5'' \times 32.5''$ FOV (see Fig. 3.3). Six of the snapshots were observed with the standard nodding (east of north, position angle = 270 degrees) and chopping (30$''$ chop throw) technique (see Sect. 1.3). The remaining four snapshots were obtained with a nodding position angle of 90 degrees. The details of the observation were as follows; $NDIT \times DIT \times NCYCLES = 30 \times 0.0625 \times 23$, where $NDIT$ is the total number of stacked images for each chopping position, DIT the detector integration time in seconds and $NCYCLES$ is the number of chopping cycles. The DIMM seeing during the observation was on average $\sim 1''$ for all three nights (see Table 3.1).

Table 3.1: *Details of the VISIR observations used in this work. They are part of the larger program of ESO ProgID 085.C-0047 designed to map compact sources in the GC.*

Observation start in UTC	Target name	Filter used	Central wavelength	DIMM seeing	Photometric standard star
2010-09-11 01:00	Central Stellar Cluster	*PAH*1	8.59 μm	~ 0.85	HD198048
2010-09-12 23:48	Central Stellar Cluster	*NeII$_2$*	13.04 μm	~ 1.12	HD178345
2010-09-10 03:31	Quintuplet Cluster	*PAH*1	8.59 μm	~ 0.85	HD217902
2010-09-11 01:54	Quintuplet Cluster	*NeII$_2$*	13.04 μm	~ 1.16	HD198048
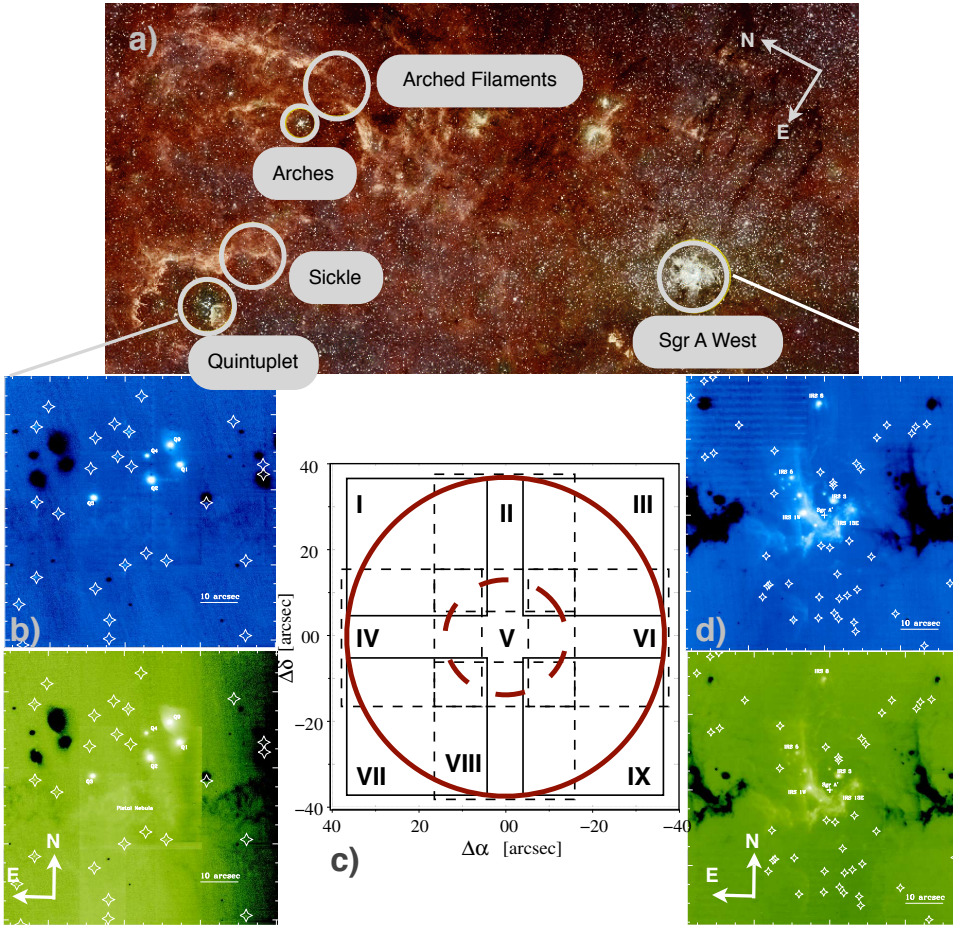
Figure 3.3: a) *HST & Spitzer composite image of the larger Galactic Center region. The dimensions of the figure are about* 300×115 *light years which is equivalent to* 91×34.8 *parsec or* 38.3×14.7 *arcmin. Image credit: Hubble: NASA, ESA and D.Q. Wang (U. Mass, Amherst); SPITZER: NASA, JPL and S. Stolovy (SSC/Caltech).* **b)** *Top:* $\sim 74'' \times 74''$ *mosaic of the Quintuplet cluster obtained with VISIR PAH1 filter (8.59 µm) with compact sources marked with star symbols. Prominent sources are also labeled. Bottom: The same as top but obtained with VISIR NeII$_2$ filter (13.04 µm).* **c)** *The squares I - IX indicate the layout of the 9 snapshots of* $\sim 32.5'' \times 32.5''$ *VISIR FOV that were used to map out circumference of the sources in order to cover the entire region suitable for MIRI science and offset pointing, as it was one of the main goals of our proposal 085.C-0047. The circles indicate the minimum and maximum radius within which the previously identified Spitzer and Chandra sources have to be located.* **d)** *Top:* $\sim 74'' \times 74''$ *mosaic of the central cluster (Sgr A) obtained with VISIR PAH1 filter (8.59 µm) with potential point sources marked with star symbols. Prominent sources are also labeled. Bottom: The same as top but obtained with VISIR NeII$_2$ filter (13.04 µm).*

3.3   Data Reduction

The data reduction process involved sky background subtraction using sky frames observed as part of the chopping and nodding technique, and correcting for dead/bad pixels. The ESO VISIR pipeline could not be used to reduce these datasets as they were observed with "raster mode" to cover a large field of view, which is not supported in the standard pipeline. For that reason, I developed my own data reduction routines using IDL.

Images obtained with VISIR DRS (former Boing) 256 BIB detector suffer from horizontal striping and appearances of ghosts (ESO VISIR manual[2]). The stripes repeat every 16 pixels in the y-direction and appear in most of the images, especially when bright objects are in the FOV. Correcting for these stripes was done by two approaches depending on their contrast. For low-contrast stripes I made use of the Multiresolution (MR) Software[3] implemented within IDL scripts (*del_pattern.pro*). However, for high-contrast stripes one has to first get an image of the repetitive pattern (obtained from the pixels at the end of each row of the science frame), subtract it and then apply the MR-algorithm. The resulting pattern images were then inspected to make sure that the MR-algorithm did not overcorrect and remove any astronomical signal. The resulting images were then combined into a large (FOV$\simeq 73'' \times 73''$) mosaic using *Montage*[4] astronomical tool (Figs. 3.3 & 4.1).

The detections and centroid positions of the compact faint sources were obtained by *find.pro*) from the public IDL Astronomy User's Library and inspected by eye to confirm the detections. The flux calibration of the sources was done with aperture photometry. The zero points for both filters were measured via standard star observations within a maximum of 40 min before or after the GC observations (see Table 3.1). The observations of the standard stars followed the ESO VISIR calibration plan and the zero points were determined using the visir_img_phot algorithm of the ESO Common Pipeline Library (CPL).

I used two aperture sizes, 0.5" and 1" in radius, for extracting the flux densities. Similar to Viehmann *et al.* (2006), the sky contribution was fitted to an annulus situated between radii of 1" and 1.5" (from the center of the aperture) for the 0.5" aperture, and between 1.6" and 2.1" for the 1" apertures. The flux density extraction was done using the algorithm (*aper.pro*) from the public IDL Astronomy User's Library and the resulting values were compared to those obtained by Viehmann *et al.* (2006) for the bright IRS sources in the central cluster. For the same extinction value they use, 1.75 at 8.6 μm, I get a flux density value of 5.17 Jy for IRS 5, very close to their value of 5.11 Jy (using the 1" aperture). Since the aim of the project is to analyze faint compact sources, I report the flux density values as obtained from the smaller aperture size, 0.5". This choice is more suitable since

---

[2]http://www.eso.org/sci/facilities/paranal/instruments/visir/doc/
VLT-MAN-ESO-14300-3514_v85.pdf

[3]www.multiresolution.com

[4]Montage is a toolkit for assembling Flexible Image Transport System (FITS) images into custom mosaics.
http://montage.ipac.caltech.edu/

the sources are compact and some are located close to bright nearby objects within the mini-spiral. I also adopt the more recent values for the extinction reported by Fritz *et al.* (2011), ~ 2.0 and ~ 1.34 for the *PAH*1 and *NeII*$_2$ filters, respectively. The extinction values used for the Quintuplet cluster are ~ 1.82 and ~ 1.65 for the *PAH*1 and *NeII*$_2$ filters, respectively (Moneti *et al.*, 2001).

3.4   Results and Discussion

The stellar disk candidates in the three clusters, e.g. IRS 13N IR-excess sources east of IRS 5 in NSC, can be studied to understand the fate of stellar disks in dense cluster environments. The massive stars in the center of the clusters are the engines which drive these processes and show disks that are highly affected by gravitational drag, by stellar encounters, and evaporation by strong stellar winds and radiation. The interaction of these young stellar disks with the radiation field of the bright cluster members can be probed with NIR/MIR fine structure lines observable with MIRI. The disk properties can be investigated via molecular lines observations and detections of ice features. Ionic lines will help to identify the physical conditions for the Arched filaments and the Sickle and determine whether they are shock features or simple in-situ accumulation features.

Within the central 400 pc × 50 pc about 150 YSOs with a mass of 10–20 $M_\odot$ have been traced down via their infrared spectral energy distribution (SEDs) (Yusef-Zadeh *et al.*, 2009, with *Spitzer*). YSOs can be bright around 10 μm due to their infrared excess in dust emission. Their existence implies a recent star formation peak only ~ 10^5 yrs ago. The VISIR data provide a database for a sensitive and systematic search for class I candidates near the Center. Our data gives a census of disk candidates as already found for Arches (Stolte *et al.*, 2010) and IRS 13N (Eckart *et al.*, 2013, 2004; Mužić *et al.*, 2008), but now at larger distances from the cluster centers. One aim is to show how frequent they are in the field, and whether there is an increased density of these candidates towards the central stellar cluster and towards the nuclei of the Arches and the Quintuplet.

The Central Stellar Cluster

Figure 3.4 shows the two *N*-band (8.59 μm and 13.04 μm) mosaics of the central stellar cluster (~ $73'' \times 73''$). Visible in both mosaics are the mini-spiral arms of ionized gas and dust, Sgr A West, which feed the SMBH at the center of the image. Several bright infrared sources such as IRS 8, IRS 5, IRS 3 and IRS 1W can be identified and are labeled (see also Fig. 3.3). The darker regions in the mosaics (left and right of the central cluster) are residues from the sky subtraction applied via the chopping/nodding observing method of VISIR (see Chapter 1).

The newly detected compact sources, in addition to known objects, are marked with star symbols. The known sources, e.g. IRS 5, were analyzed for comparison with the previ-

ous analysis of Viehmann *et al.* (2006) who studied several dusty objects within and close to the mini-spiral. The new mosaics, however, cover a larger FOV and hence contain new detections. The position of Sgr A* in the MIR images was determined relative to prominent sources, like IRS 16NW, IRS 7 or IRS 29 and compared to the position obtained by Schödel *et al.* (2007). Noticeable is the lack of detections to the east and west of the cluster due to the negative images of the cluster lying in these regions.

A Census of Compact Sources

The detection of compact sources was done using the 8.59 μm mosaic. The flux density values were extracted and then compared to the values obtained for the same positions at the longer wavelength, 13.04 μm, image. About 90 sources were analyzed but only 77 had reliable flux density measurements in both bands. Consequently, spectral index values were calculated as follows:

$$\alpha = \frac{\log(F_{13.04}/F_{8.59})}{\log(8.59/13.04)}. \tag{3.1}$$

Table 3.2 lists the sources that had reliable detections in both wavelengths. Listed in the table are their offset position (in arcsec) from the location of Sgr A*, the flux density values at both wavelengths with their uncertainties and the estimated spectral index. The previously known sources are designated by their name in the last column of the table. Sources labeled as "contaminated" refer to the ones that had an unreliable background subtraction, due to the fact that the corresponding sky annulus includes counts from other nearby sources. The flux density values reported for the extended sources were obtained using the same aperture size, 0.5", as the compact ones. The aperture was positioned on the region of highest pixel counts.

Most of the newly detected faint sources show an increase in flux density towards longer wavelengths. Based on previous classifications of the MIR objects in the same region by Viehmann *et al.* (2006), most of these new faint dusty objects are consistent with trends observed for bow-shock sources (Fig. 3.5). As one can see in Fig. 3.6 when one separates the objects based on the apparent morphology most of the newly detected faint objects show a sharper increase of flux towards longer wavelengths. This is in agreement with Viehmann *et al.* (2006) where they report a similar trend for the low-luminous bow shock sources. However, we would like to note that one cannot conclusively classify any of those objects only based on observations taken at two wavelengths. Our observations were only limited to two bands since the primary goal was to provide a high spatial resolution and deep map of the region as pioneer target selection for future MIRI observations.

I have successfully identified several faint potentially interesting targets (see the next chapter for detailed analysis of one object) and accurately mapped the position of the bright sources in order to avoid them in selecting FOVs for future MIRI observations. Figure 3.7 shows a spectral index map of 77 sources, in offsets from the position of Sgr A*,
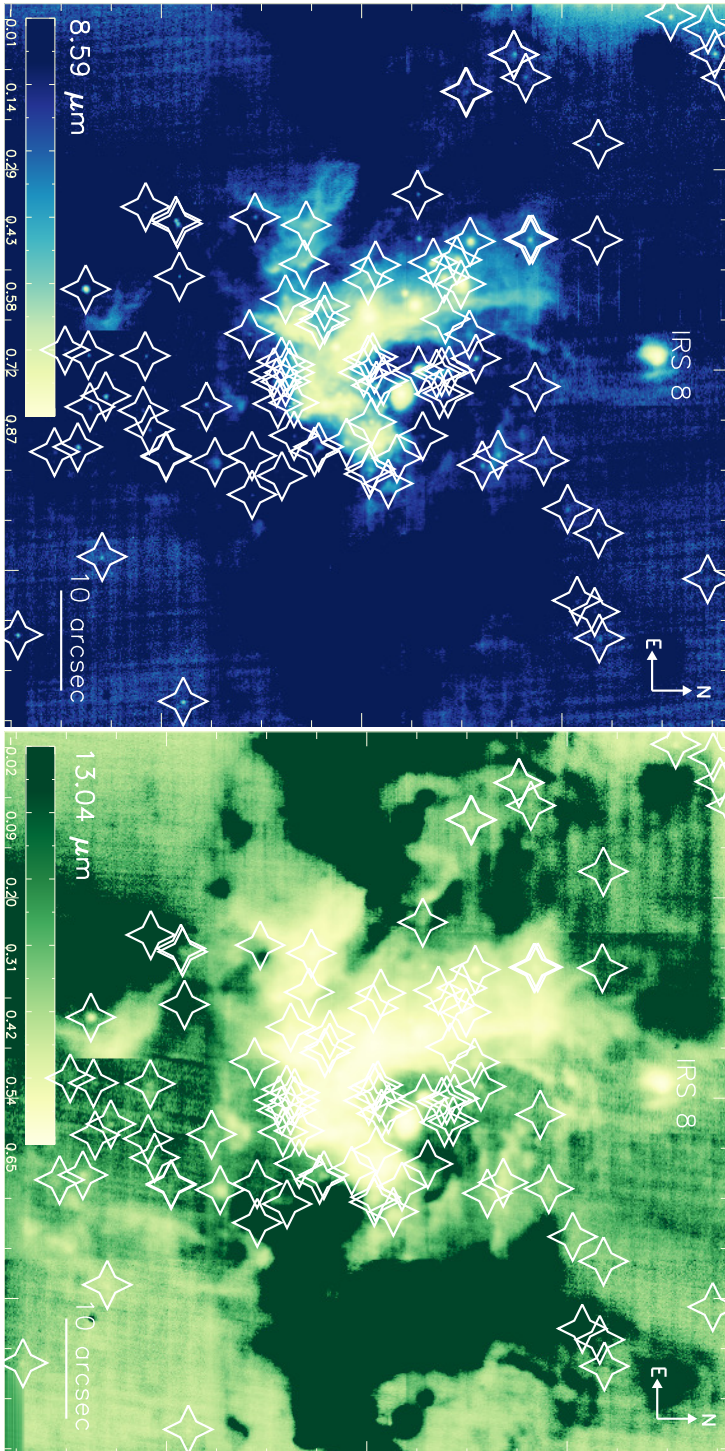
Figure 3.4: *Left: PAH1 (8.59 μm) mosaic of the central stellar cluster where the positions of the detected compact and known sources have been marked with star symbols. Right: same as the left mosaic but in NeII (13.04 μm) filter. The detection of the sources have been made using the PAH1 filter. The numbers on the colorbars are in Jy pixel^{-1}.*
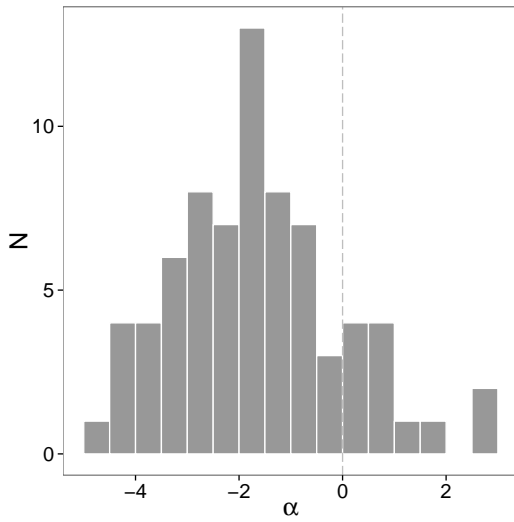
Figure 3.5: *Histogram of spectral index values for compact sources in the central cluster.*
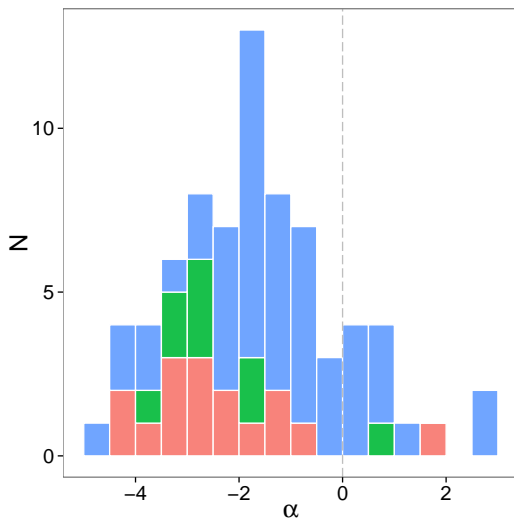
Figure 3.6: *Similar to the Fig. 3.5. Here blue represents compact sources, green are the objects which show extended morphologies and pink indicates the sources whose flux measurements are contaminated by uncertainty in the sky subtraction in at least one band.*
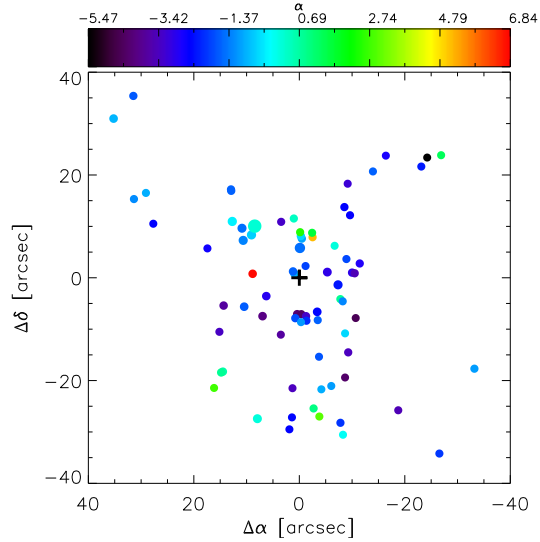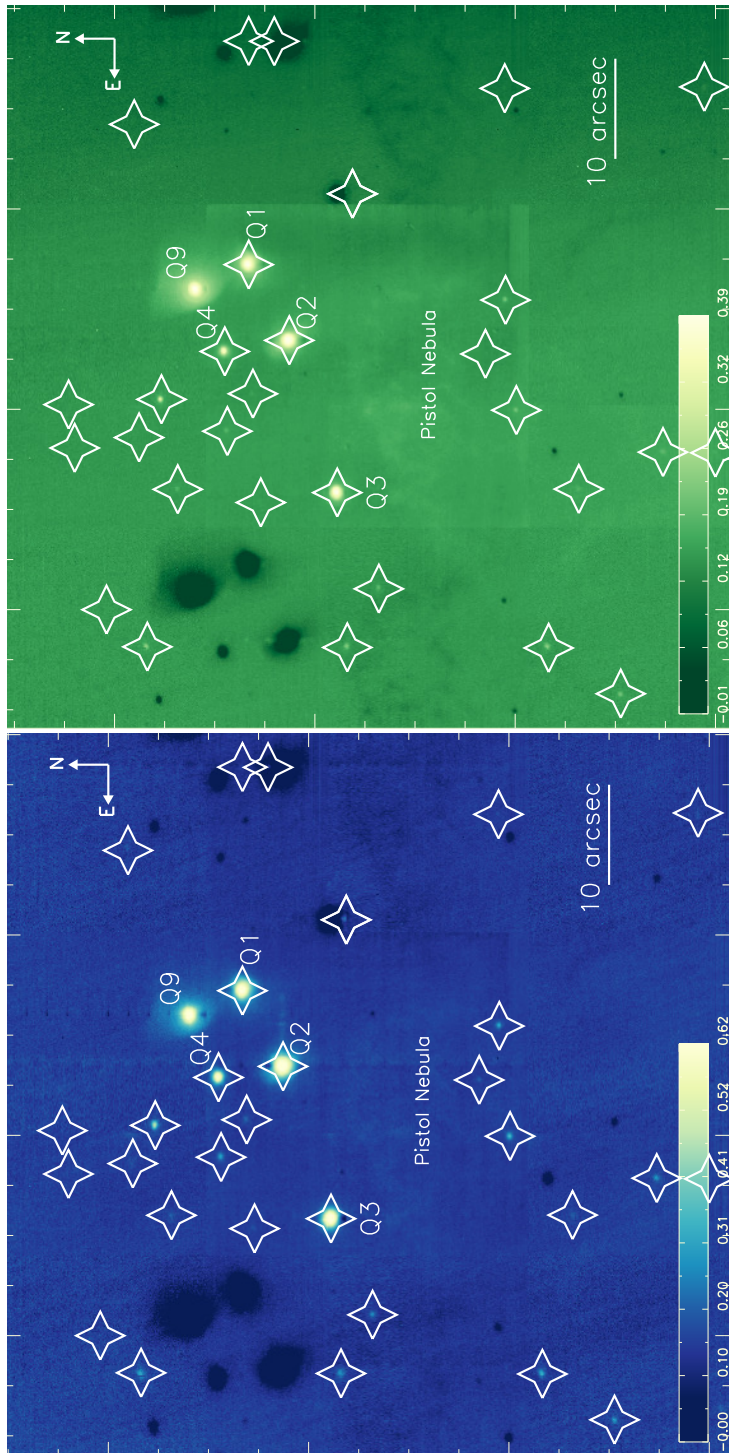
Figure 3.7: *Spectral index map of the 77 sources listed in Table 3.2. The color of each source indicates its spectral index, α. The size of each symbol is proportional to the flux obtained at PAH1-band, 8.59 μm of the corresponding source. The position of Sgr A* is indicated by a cross.*

which are listed in Table 3.2. The color of each source indicates its spectral index, α. The size of each symbol is proportional to the flux obtained at *PAH*1-band, 8.59 μm of the corresponding source.
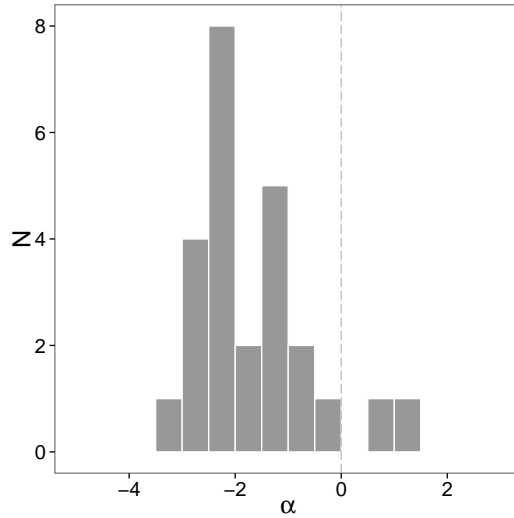
The Quintuplet Cluster

Figure 3.8, similar to 3.4, shows the two *N*-band (8.59 μm and 13.04 μm) mosaics of the Quintuplet cluster ($\sim 73'' \times 73''$). Visible in both mosaics are the five luminous near-infrared (NIR) dusty carbon WR stars (Moneti *et al.*, 2001), that give Quintuplet its name. The age of the cluster is estimated to be $\sim 4 \pm 1$ Myr (Figer *et al.*, 1999b,c). The pistol nebula can be seen as well, especially in the longer wavelength. It is believed to have been ejected from the pistol star several thousand years ago (Figer *et al.*, 1999a). The darker regions in the mosaics (left and right of the Q-stars) are residues from the sky subtraction applied via the chopping/nodding observing method of VISIR (see Chapter 1).

The detected compact sources, in addition to known sources, are marked with star symbols. The known sources, e.g. Q3, were analyzed for comparison with the previous analysis of Moneti *et al.* (2001). These new mosaics, however, cover a larger FOV and hence contain new sources. Noticeable is the lack of detections to the east and west of the cluster due to the negative images of the cluster lying in these regions. The detection of the compact sources was done using the 8.59 μm mosaic. The flux density values were extracted and then compared to the values obtained for the same positions from the longer wavelength, 13.04 μm, image. About 31 sources were analyzed but only 26 gave reliable flux density values in both bands. Consequently, spectral index values were calculated using Eq. (3.1). Table 3.3 lists the sources that had reliable detections in both wavelengths.

Figure 3.8: *Left: PAH1 (8.59 µm) mosaic of the Quintuplet cluster where the positions of the detected compact and known sources have been marked with star symbols. Right: same as the the left mosaic but in NeII (13.04 µm) filter. The detection of the sources have been made using the PAH1 filter. The numbers on the colorbars are in Jy pixel^{-1}.*

Figure 3.9: *Histogram of spectral index values for compact sources in the Quintuplet cluster.*
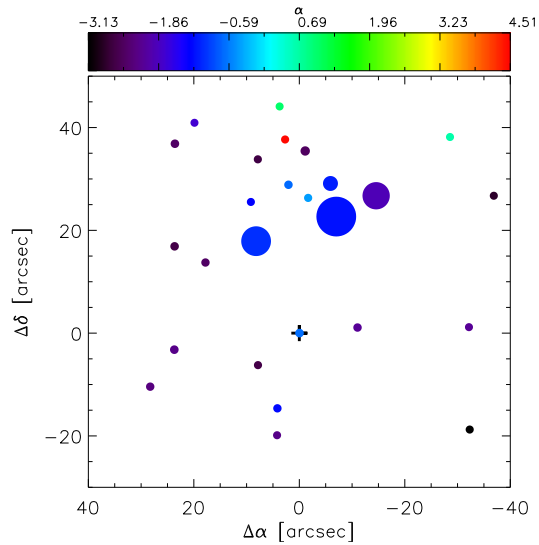
Figure 3.10: *Spectral index map of the 26 sources listed in Table 3.3. The color of each indicates its spectral index, α. The size of each symbol is proportional to the flux obtained at PAH1-band, 8.59 μm of the corresponding source. The position of the pistol star is indicated by a cross.*

Listed in the table are their positions in offset in arcsec from the position of the pistol star, the flux density values at both wavelengths with their uncertainties and the calculated spectral index. The known sources are designated by their name in the last column of the table.

Similar to the NSC, most sources appear to have negative spectral index, α, values (Fig. 3.9). As noted before, this is in agreement with the previous reports of increasing flux towards longer wavelengths for the known low-luminous bow shock sources Viehmann *et al.* (2006). Figure 3.10 shows a spectral index map of the 26 sources, in offsets from the position of the pistol star, listed in Table 3.3. The color of each source indicates its spectral index, α. The size of each symbol is proportional to the flux obtained at $PAH1$-band, 8.59 μm of the corresponding source.

3.5   Summary

Some dynamical processes at the GC - like existence and kinematics of young stars within 0.1 pc from Sgr A* - are well explained by the presence of IMBHs (intermediate-mass black holes 10^2–10^5 $M_\odot$). In the immediate surroundings of higher mass concentrations (the central cluster itself as well as dense stellar clusters like Arches and Quintuplet) the space density of IMBHs is likely increased with respect to the field and these objects can be searched for and isolated against luminous young stars. IMBHs are likely to sink towards the cluster centers due to gravitational friction (Portegies Zwart *et al.*, 2006). Nayakshin and Sunyaev (2007) find the total luminosity of stellar mass remnant cusps to be in some cases comparable to that of the central SMBH at low gas densities, as is likely the case in the GC. Individual IMBHs and stellar mass remnants will be bright around 10 μm due to steep spectrum synchrotron radiation that may occur during accretion. The spectral indices of the point sources detected from the data, using both MIR filters 8.59 μm and 13.04 μm, will aid in the identification of such candidates. If combined with follow up (i.e. different epochs of observations) the currently studied mosaics will prove to be a unique asset to determine the variability of the faint sources and measure possible proper motions for applicable ones. In addition, these sources can be compared with the higher frequency archival data (e.g. NaCo, *Spitzer*'s and *Chandra*'s already detected sources) to identify possible counterparts.

A full analysis of the detected sources in terms of flux densities and accurate positions will be presented and made available in an upcoming paper (Sabha *et al.* 2015b, in prep.).

The MIR data presented here are the first and only data that cover a large FOV $\sim$ $74'' \times 74''$ in the GC region, which is essential in scheduling future MIRI JWST observing campaigns. Although the primary goal of our observations was to obtain a deep and accurate MIR map of the important fields in the GC region (in which we successfully located all bright sources with high accuracy and identified empty fields for future MIRI calibrations),

however, several new faint objects emerged from my analysis. While the combination of the two available bands enables us to acquire some insight on these newly detected dusty objects, only dedicated multi-frequency studies of each individual source would enable us to draw conclusions about it in order to get a better picture of the nature and distribution of such faint sources inside prominent GC star clusters. In the following section, I present such a follow up study focusing on one of the newly detected MIR objects whose morphology resembles a bow shock at a distance of 0.68 pc from the central supermassive black hole.

Table 3.2: *List of the compact and some of the known MIR objects detected in the NSC. Positions are the offset from Sgr A* (in arcsec) and observed fluxes at PAH1 and NeII filters are reported in mJy.*

Detected source	$\Delta\alpha$ (arcsec)	$\Delta\delta$ (arcsec)	$F_{8.59}$ (mJy)	$\pm$ (mJy)	$F_{13.04}$ (mJy)	$\pm$ (mJy)	α	$\pm$	
1	0.93	0.79	185.18	19.76	264.83	65.11	-0.86	0.11	
2	1.19	1.23	193.27	15.02	372.76	42.20	-1.57	0.06	
3	-1.18	2.29	26.48	12.25	57.92	23.00	-1.88	0.25	
4	-5.31	1.10	399.42	44.81	1389.71	228.76	-2.99	0.08	contaminated
5	-0.11	5.80	1355.61	37.00	2506.66	51.02	-1.47	0.01	IRS7
6	0.42	-7.07	151.72	15.46	896.61	51.30	-4.26	0.05	faint
7	-0.38	-7.09	115.86	15.53	715.48	36.89	-4.36	0.06	contaminated
8	6.26	-3.57	259.66	22.58	865.81	46.60	-2.89	0.04	extended
9	-3.39	-6.63	324.15	18.30	902.59	31.46	-2.45	0.03	contaminated
10	-7.34	-1.37	540.93	23.35	1413.30	89.52	-2.30	0.03	contaminated
11	-1.28	-7.47	113.38	13.24	455.53	22.81	-3.33	0.05	contaminated
12	-0.47	7.62	159.88	12.99	234.48	17.34	-0.92	0.05	IRS7/tail3
13	0.76	-7.86	155.87	18.58	322.67	26.93	-1.74	0.06	contaminated
14	-0.29	8.12	149.68	13.15	181.19	15.09	-0.46	0.05	IRS7/tail2
15	-2.51	7.89	75.41	10.11	8.60	10.10	5.20	0.49	contaminated
16	-1.35	-8.36	98.33	10.53	238.08	18.35	-2.12	0.06	
17	-0.32	-8.64	26.75	7.25	42.05	33.51	-1.08	0.35	contaminated
18	-7.79	-4.15	84.49	11.22	59.50	27.32	0.84	0.20	extended
19	-0.15	8.86	77.16	10.82	26.65	13.78	2.55	0.22	IRS7/tail1
20	8.85	0.77	237.75	24.54	13.68	64.42	6.84	1.97	contaminated
21	-3.49	-8.24	47.40	7.37	90.81	11.06	-1.56	0.08	edge
22	-2.43	8.75	58.81	8.77	29.32	9.52	1.67	0.15	contaminated
23	-6.69	6.22	31.25	6.80	28.97	20.16	0.18	0.30	faint
24	-8.23	-4.58	45.21	8.35	75.11	22.83	-1.22	0.15	contaminated
25	-8.93	3.64	59.76	8.58	127.43	15.08	-1.81	0.08	extended
26	-10.01	1.00	169.51	14.30	591.56	39.89	-2.99	0.05	extended
27	6.97	-7.47	279.80	24.46	1511.44	163.06	-4.04	0.06	contaminated
28	-10.50	0.88	106.35	13.21	460.99	48.39	-3.51	0.07	contaminated
29	3.44	10.88	75.90	10.64	300.39	34.63	-3.30	0.08	extended
30	1.04	11.53	88.02	10.10	74.16	12.77	0.41	0.09	
31	3.51	-11.07	27.65	8.50	133.42	19.26	-3.77	0.14	
32	-11.46	2.78	114.09	11.21	367.58	22.85	-2.80	0.05	extended
33	10.45	-5.63	298.56	24.68	582.91	76.61	-1.60	0.06	extended
34	9.07	8.34	599.17	30.30	760.86	62.39	-0.57	0.04	contaminated
35	10.64	7.28	549.21	27.44	929.80	62.06	-1.26	0.03	IRS5/extended
36	8.46	10.05	4620.82	73.01	4090.20	136.06	0.29	0.02	IRS5
37	-10.69	-7.84	12.89	4.07	84.55	14.88	-4.51	0.15	faint
38	-8.67	-10.82	14.13	4.17	17.55	6.59	-0.52	0.20	faint

Table 3.2: *continued.*

Detected source	$\Delta\alpha$ (arcsec)	$\Delta\delta$ (arcsec)	$F_{8.59}$ (mJy)	± (mJy)	$F_{13.04}$ (mJy)	± (mJy)	α	±	
39	10.87	9.64	510.11	24.82	942.23	37.28	-1.47	0.03	IRS5/5E
40	14.35	-5.41	216.61	19.23	1035.76	57.89	-3.75	0.04	extended
41	-9.61	12.17	58.34	8.59	169.19	15.94	-2.55	0.07	contaminated
42	-3.73	-15.37	30.55	6.55	62.51	15.29	-1.72	0.14	edge
43	-8.55	13.75	132.73	12.08	376.97	28.04	-2.50	0.05	contaminated
44	12.71	10.96	618.06	25.24	685.50	35.10	-0.25	0.03	IRS5/5NE
45	-9.27	-14.52	107.70	10.80	447.74	22.36	-3.41	0.05	extended
46	17.42	5.71	38.80	7.41	116.07	16.21	-2.63	0.10	
47	15.15	-10.52	52.67	14.45	212.53	68.09	-3.34	0.18	contaminated
48	-9.17	18.30	37.35	7.09	140.45	14.00	-3.17	0.09	contaminated
49	-8.67	-19.41	8.07	4.46	48.83	9.87	-4.31	0.25	
50	12.92	16.92	123.02	11.48	236.57	18.15	-1.57	0.05	edge
51	1.30	-21.49	27.12	6.00	112.24	13.38	-3.40	0.10	
52	12.95	17.20	113.59	11.12	220.13	19.32	-1.59	0.05	
53	-6.06	-21.06	34.75	6.52	53.86	10.35	-1.05	0.11	
54	-4.18	-21.70	19.87	5.51	28.77	8.77	-0.89	0.17	
55	14.49	-18.26	162.31	13.66	124.31	22.82	0.64	0.08	
56	14.82	-18.43	151.59	13.33	105.51	22.81	0.87	0.10	
57	-13.96	20.69	43.70	7.23	83.62	17.28	-1.55	0.11	
58	-2.71	-25.43	90.78	10.12	60.00	11.92	0.99	0.10	
59	16.17	-21.44	28.47	6.61	8.94	9.51	2.77	0.45	
60	1.40	-27.17	24.68	5.82	68.70	10.25	-2.45	0.12	
61	-3.80	-27.00	39.76	7.01	11.28	8.59	3.02	0.33	
62	7.95	-27.42	476.60	22.30	444.30	29.25	0.17	0.03	
63	-16.41	23.76	11.14	5.34	34.79	9.15	-2.73	0.23	
64	-7.80	-28.22	90.99	10.07	208.07	16.10	-1.98	0.06	
65	1.88	-29.49	18.78	5.28	52.73	10.38	-2.47	0.14	
66	27.69	10.52	37.24	7.30	105.22	14.03	-2.49	0.10	
67	-8.28	-30.54	31.03	6.30	31.69	7.85	-0.05	0.13	
68	-23.13	21.64	40.37	7.91	103.70	22.73	-2.26	0.12	
69	-18.76	-25.78	39.21	7.40	170.01	17.27	-3.51	0.09	
70	29.08	16.51	51.93	8.75	74.79	13.02	-0.87	0.10	
71	-24.24	23.39	6.45	4.87	63.25	17.06	-5.47	0.33	
72	31.36	15.32	74.45	9.58	122.28	16.65	-1.19	0.08	
73	-26.89	23.85	38.85	7.74	21.72	15.56	1.39	0.31	
74	-33.20	-17.69	88.19	10.38	137.21	15.43	-1.06	0.07	
75	-26.56	-34.20	55.71	8.31	125.21	17.77	-1.94	0.09	
76	35.22	30.98	292.70	27.58	407.24	40.10	-0.79	0.06	
77	31.47	35.38	134.35	13.51	270.07	36.19	-1.67	0.07	

Table 3.3: *Similar to Table 3.2 for the sources in the Quintuplet cluster. Positions are the offset from the position of the pistol star (in arcsec).*

Detected source	$\Delta\alpha$ (arcsec)	$\Delta\delta$ (arcsec)	$F_{8.59}$ (mJy)	± (mJy)	$F_{13.04}$ (mJy)	± (mJy)	α	±	
1	0.00	0.00	126.81	11.34	166.64	15.40	-0.65	0.05	pistol star
2	7.84	-6.23	30.25	5.84	91.26	11.74	-2.65	0.10	
3	-11.03	1.09	94.46	9.80	229.65	16.05	-2.13	0.05	
4	4.16	-14.63	78.38	9.04	131.18	13.16	-1.23	0.06	
5	8.19	17.89	7932.36	89.60	12070.48	110.59	-1.01	0.01	Q3
6	4.22	-19.87	12.48	4.11	31.66	8.09	-2.23	0.17	
7	17.80	13.74	76.08	9.17	212.97	17.35	-2.47	0.06	
8	-7.01	22.68	13463.83	117.20	22174.71	154.71	-1.20	0.00	Q2
9	23.70	-3.22	130.52	11.74	328.92	20.30	-2.21	0.05	
10	-1.67	26.31	38.74	6.39	45.17	8.57	-0.37	0.10	
11	9.18	25.52	16.57	4.30	28.45	6.31	-1.29	0.14	
12	2.06	28.86	97.70	10.00	130.44	12.03	-0.69	0.06	
13	23.65	16.89	114.12	11.04	344.57	20.81	-2.65	0.05	
14	-5.90	29.12	1835.36	42.93	2902.18	54.32	-1.10	0.01	Q4
15	28.27	-10.42	84.49	9.75	218.50	17.85	-2.28	0.06	
16	-14.56	26.73	6733.51	82.57	14941.14	126.84	-1.91	0.01	Q1
17	-32.17	1.17	10.22	3.82	24.89	9.40	-2.13	0.22	
18	7.86	33.82	35.46	6.29	108.15	11.90	-2.67	0.09	
19	-1.12	35.44	299.94	17.50	851.53	29.90	-2.50	0.03	
20	-32.31	-18.76	19.64	5.14	72.64	11.39	-3.13	0.13	
21	2.69	37.68	25.51	5.47	3.89	6.36	4.51	0.69	
22	23.59	36.85	120.98	11.49	337.89	20.91	-2.46	0.05	
23	3.74	44.10	9.97	3.84	6.47	6.45	1.04	0.45	
24	19.88	40.93	6.40	4.34	13.16	10.27	-1.73	0.43	
25	-36.88	26.73	15.21	4.87	49.23	11.26	-2.81	0.16	
26	-28.57	38.16	19.02	5.37	14.33	11.09	0.68	0.34	

NEW MIR BOW SHOCK SOURCE AT THE GALACTIC CENTER

I find a convex-like mid-infrared feature at a distance of 0.68 pc ($17''$) from the position of the supermassive black hole, Sgr A*, at the center of the nuclear stellar cluster. This feature resembles a stellar bow shock with a symmetry axis pointing toward the Center. I discuss the possible nature of this feature and the implications of its alignment with other dusty comet-like objects inside the central parsec. If it is indeed a stellar bow shock, the estimates I get for the velocity of an external wind, ∼ 500–1000 km s^{-1}, hint toward a collimated outflow, either from the disk of mass-losing GC stars or the position of the SMBH Sgr A*. The latter argument supports the claims of equatorial outflows that have been found in extragalactic nuclei.

4.1 Introduction

Several studies discuss whether the Galactic Center (GC) black hole can be considered a member of the Low Luminosity Active Galactic Nuclei (LLAGN) class (Contini, 2011; Ho, 2008). For instance, Contini (2011) find that the GC is comparable to faint LLAGN in its radio and far-infrared continuum and line emission ([OI] 63 μm & 145 μm, [NII] 122 μm, [CII] 158 μm). Ho (2008), on the other hand, consider the short duty cycle of the black hole accretion to be responsible for most AGN spending their life in a low state. This leads to modest luminosities for most of the AGN population. Hence, one has to take into account alternative mechanisms and not rely only on the absolute luminosity of an AGN to define the nuclear activity. Strong similarities present themselves when comparing the

continuum spectra from radio to X-ray of the Galactic Center to that of some LLAGNs. Observations of these galaxies suggest theoretical models of radiatively inefficient accretion flows (RIAF) where the luminosities are $\leq 10^{-7} L_{\text{Edd}}$, and when $L_{\text{bol}}/L_{\text{Edd}} \leq 10^{-3}$ the broad line region (BLR) disappears and a temporarily existing disk becomes very probable (Laor, 2003; Nicastro, 2000; Xu and Cao, 2007).

As of yet, observations have not been able to either confirm or deny the existence of an outflow/jet emanating from the center of the Galaxy, where the supermassive black hole (SMBH) is located. However, there are hints of past AGN-like activity of the black hole as evident by the detected X-ray light echo off the Sgr B2 giant molecular cloud. This allows an estimate to be made of a higher luminosity for Sgr A* by about few 10^5 times a few hundred years ago (Sunyaev *et al.*, 1993; Koyama *et al.*, 1996; Revnivtsev *et al.*, 2004; Muno *et al.*, 2007; Ponti *et al.*, 2010, see (Fryer *et al.*, 2006) for an alternative explanation for the echo). Another indication of such activity is argued by Silk *et al.* (2012): the presence of OB hypervelocity stars (HVS; 300 to 1000 km s^{-1} away from the Center) are believed to be caused by the interactions of an AGN jet from the central black hole with a dense molecular cloud.

The underluminosity of the source makes it difficult to distinguish among the different physical processes responsible for its variable emission from the radio up to the X-rays. No optical wavelength information can be obtained from the GC due to the line-of-sight extinction of $\sim$ 30 magnitudes (Becklin and Neugebauer, 1968; Becklin *et al.*, 1978; Rieke and Lebofsky, 1985; Rieke *et al.*, 1989). Analysis of the radio–mm regime emission points toward a synchrotron process and a radiatively inefficient, advection-dominated accretion flow (e.g. Markoff *et al.*, 2001; Narayan and McClintock, 2008; Yuan, 2011). Highly resolved radio observations using the very long baseline interferometry (VLBI) technique show that the source associated with the SMBH is compact (Doeleman *et al.*, 2008) which supports the no-jet hypothesis. However, Markoff *et al.* (2007) use the spectrum and morphology of Sgr A* across all observable wavelengths and derive constraints on the inclination and position angles of a bi-polar putative jet. Recent VLBA 7 mm observations of the radio source Sgr A* show its morphology to be consistent with emission from a jet or an accretion disk (Bower *et al.*, 2014). They model the source by an elliptical Gaussian with the major-axis position angle of 95° east of north. The multi-wavelength observations of Bower *et al.* (2014) suggest that not all X-ray and near infrared (NIR) flares have a radio counterpart. They interpret this by attributing the high energy flares to electron excitation rather than an enhanced accretion onto the SMBH.

There have been several structures observed in the radio, infrared or the X-ray regime, which are within a few parsecs of the position of the SMBH. These structures have been interpreted as evidence of interaction regions between a jet/outflow emanating from the black hole position, and the interstellar medium. The most recent of these reports favoring an outflow direction (semi-) parallel to the Galactic plane i.e. the NE or SW direction are

(i) the presence of NIR filamentary structures and bow-shock-shaped features, in addition to the mini-cavity (Mužić *et al.*, 2007, 2010); (ii) a linear feature in the radio cm-maps of the GC and a number of weak blobs along its direction (Yusef-Zadeh *et al.*, 2012a); (iii) an earlier finding of a NIR bubble of hot gas engulfed within the mini-spiral to the south-west of the SMBH (Eckart *et al.*, 1992). The evidences supporting a NW/SE as an alternative direction are (i) a NIR linear feature (Eckart *et al.*, 2006); (ii) gamma-ray bubbles and linear gamma-ray features along opposite directions from the Center (Su *et al.*, 2010; Su and Finkbeiner, 2012); (iii) a linear X-ray feature, G359.944-0.052, pointing to the position of Sgr A* Muno *et al.* (2008); (iv) the same X-ray feature supported by the presence of a radio shock front on the Eastern Arm of the mini-spiral (Li *et al.*, 2013b).

The Galactic Center has been observed in the near-infrared intensively. These observations have allowed accurate investigations of the stellar population of the nuclear star cluster (NSC, Schödel *et al.*, 2009; Buchholz *et al.*, 2009; Do *et al.*, 2009; Bartko *et al.*, 2010, and several others) and provided the first compelling evidence for the existence of a SMBH via orbital fitting of the high velocity star S2 (Schödel *et al.*, 2002; Ghez *et al.*, 2003). However, GC observations in the mid-infrared (MIR) regime, using ground-based telescopes, have been less extensive and were mostly concentrated on the inner parsec of the cluster. These studies were dedicated to examine dusty structures associated with the mini-spiral, especially the northern and eastern arm, and parts of the western arc, as well as several bright circumstellar dusty sources Moultaka *et al.* (2005, 2009); Viehmann *et al.* (2006). Several bow shocks -caused by the interaction of a stellar wind with in-falling material of the mini-spiral- were also found, e.g. IRS 1W, 5, 10W, 21 and the very bright IRS 8 (Tanner *et al.*, 2002, 2005; Rauch *et al.*, 2013; Sanchez-Bermudez *et al.*, 2014). Irons *et al.* (2012) use NeII emission to study the kinematics of the ionized gas in the Sgr A west (mini-spiral). They explain the structure by an one-armed spiral density wave that may be caused by the precession of elliptical orbits in the potential of the black hole and the central cluster.

In this chapter I investigate the presence of a convex-like mid-infrared feature at a distance of 0.68 pc ($17''$) from the position of the SMBH, Sgr A*, at the center of the NSC. This feature resembles a stellar bow shock with a symmetry axis pointing toward the Center. I discuss the possible nature of this feature and the implications of its alignment with other dusty comet-like objects inside the central parsec. In Section 4.2 I present the results from the data reduction analysis of the previous chapter, and relate them to other mentions of the source in the literature. I then discuss the bow-shock scenario of the feature and the possible nature of the external wind that may cause it. I summarize and discuss the implications of my results in Section 4.3. I adopt a distance to the Galactic Center of 8 kpc, where 1 arcsec translates to 0.04 pc projected distance.
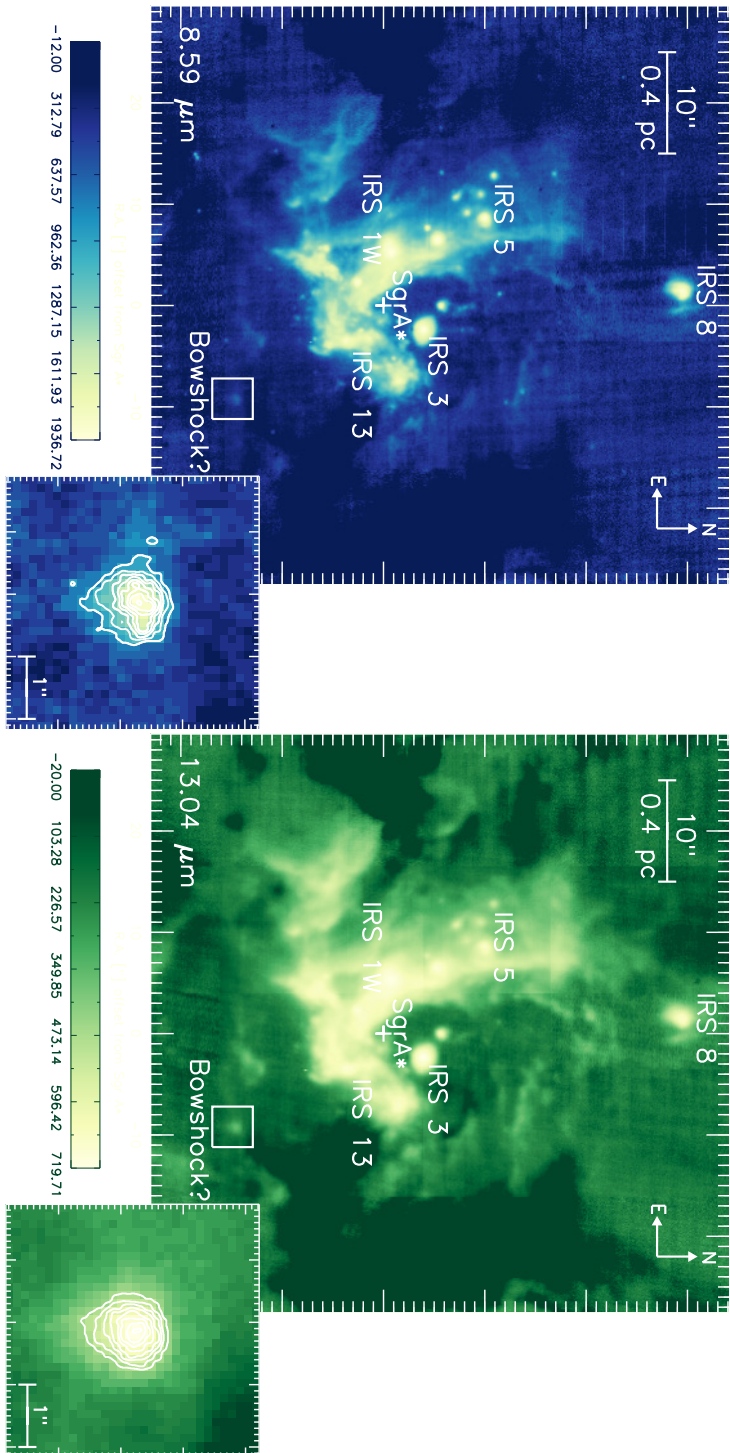
Figure 4.1: *Left: PAH1 (8.59 μm) mosaic of the central stellar cluster where the position of Sgr A* is marked and several IRS sources are labeled. The inset shows a zoomed image of the feature X24 -as called by Zhao et al. (2009). Right: same as the the left mosaic but in NeII (13.04 μm) filter. The numbers on the colorbars are in digital counts. The contour levels were produced by resampling the fits files 20 times and are at 95%, 90%, 80%, 70%, 60%, 50%, 40%, 30% of the maximum flux value for each image.*

4.2 Results

Figure 4.1 shows two *N*-band (8.59 μm and 13.04 μm) mosaics of the central stellar cluster ($\sim 73'' \times 73''$). The details of the observation and data reduction have been described in Sect. 3.2 & 3.3 of the previous chapter. Visible in both mosaics is the mini-spiral arms of ionized gas, Sgr A West, which feed the SMBH at the center of the image. Several bright infrared sources such as IRS 8, IRS 5, IRS 3 and IRS 1W can be identified and are labeled. A very faint bow-shock-like feature is noticeable at a distance of $\sim 17''$ (0.68 parsec) from Sgr A* in the south-west direction (PA $\simeq 212°$ east of north). The feature is marked with a box and the inset is zoomed to the bottom right corner to show the details of its morphology, the convex shape. The darker regions in the mosaics (left and right of the central cluster) are residues from the sky subtraction applied via the chopping/nodding observing method of VISIR (see Chapter 1).

The contours overlaid on the bottom right squares of Fig. 4.1 were produced by resampling (rebinning) the fits files 20 times. The minimum value for the contours were chosen to be the 2 σ of the noise of the image inset, as estimated from the Gaussian fit of the distribution of pixels (see description of Fig. 4.2). The position of this feature, with respect to the position of Sgr A*, interestingly coincides with several previously reported features to the south west of the SMBH (Mužić *et al.*, 2010). Below I review the properties of the source from the literature, and lay the grounds for my interpretation of its nature.
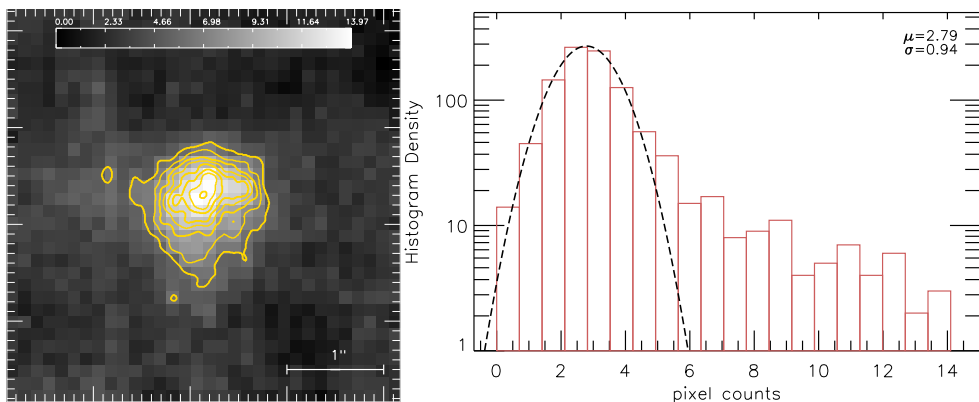
Figure 4.2: *The left panel, same as the inset of Fig. 4.1, shows the X24 feature in the PAH*1 *(8.59 μm) filter. The contours (in yellow) are plotted above 2-σ of the noise component estimated from the Gaussian fit to the image histogram shown in the right panel.*

The Extended Source X24

Zhao *et al.* (2009) identify an unresolved extended source in their 3.6 cm Very Large Array (VLA) multi-epoch archive observations. The source is located at $\Delta\alpha = -9.180'' \pm 0.005''$ and $\Delta\delta = -14.680'' \pm 0.010''$, with respect to the position of Sgr A*. They refer to it as X24

and associate it with the infrared source MP-09-14.4 from Genzel *et al.* (2000). They report a proper motion of the source of $\mu_\alpha = -3.5 \pm 0.6$ mas yr^{-1}and $\mu_\delta = -5.4 \pm 1.3$ mas yr^{-1}, which corresponds to $\nu_t = 244 \pm 43$ km s^{-1}(position angle$= -147° \pm 9°$ measured from north to east), and a line of sight velocity of -18 ± 8 km s^{-1}. X24 is at the same position in projection as our feature and has a similar shape as can be seen from their Figure 6 (see also their Figures 2 & 12).

In our resolved MIR images, the source appears with a convex-like morphology in its north-east corner (the part closest to the position of Sgr A*). The radio proper motion (as measured by Zhao *et al.*, 2009) indicates that X24 moves through the GC medium in the opposite direction, i.e. south-westward from Sgr A*, which hints toward an external wind blowing from the north-east direction that may be considered responsible for the observed shape. Considering the magnitude of the transverse velocity on the plane of the sky, this means that the external wind should be faster than ≈ 250 km s^{-1}to cause the convex-like shape. Otherwise, the apparent proper motion could be explained by the apparent change of the emission centroid of the source if the source experiences slight variations in the measured flux density across its extended shape. The source is bright as well in the Paschen$_\alpha$ (Pa$_\alpha$) emission studied in (Wang *et al.*, 2010, their Figure 4a). Pa$_\alpha$ emission from warm ionized gas is used to trace massive stars and their environments. It is caused by Lyman continuum radiation from the stars which ionizes the gas in the stellar winds and the surrounding circum-stellar material and ISM.

Irons *et al.* (2012) detect the source in their *NeII* spectroscopic observations. Inspecting the publicly available reduced data cube[1] X24 has a $V_{\rm LSR} \simeq -24$ km s^{-1}(see Fig. 4.3). The feature cannot be fitted in their density wave model by which they explain the mini-spiral structure (Figure 6 in Irons *et al.*, 2012), and thus it is most probably independent from the structure of the nearby western arc. The extended Pa$_\alpha$ emission, the detection in MIR due to the presence of dust, dominated by Polycyclic Aromatic Hydrocarbon (PAH) emission, and having evidence for ionized gas from the *NeII* spectroscopic and imaging observations all point to a peculiar nature of the source. Its convex-like morphology and location adds to its importance for it is aligned with the same direction of earlier claims for an outflow/jet from Sgr A*.

X24 is faint (~ 0.22 Jy) and still it appears to have the morphology of a bow shock with the tip pointing toward the center of the cluster. To investigate whether the shape we see is real or just random noise, I plot the histogram of the pixel value distribution. While the noise has a Gaussian profile, the science signal contributes a power-law component to the histogram. Figure 4.2 shows the shape of X24 traced by the yellow contours which I have plotted above the noise level of the image. The histogram of the pixel distribution of the part of the mosaic where our source is located is shown on the right panel of Fig. 4.2 and is

---

[1]http://iopscience.iop.org/0004-637X/771/1/75/suppdata/apj475593_fits.tar.gz
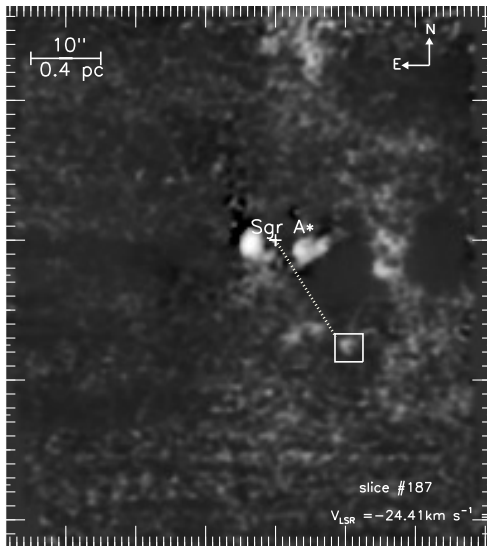
Figure 4.3: *Slice of the MIR NeII data cube taken from Irons et al. (2012). The slice is taken at a $V_{LSR} \simeq -24.41$ km s^{-1} where the emission from the feature X24, marked by a square, is most prominent.*

fitted with a Gaussian profile. The median and σ of the fit are used to determine the minimum value (2.79 + 0.94 counts) for the contour plot shown on the left panel of the same figure (Fig. 4.2). The shape traced by the contours supports my stellar bow shock interpretation. Investigating the intensity profile along different axes dissecting X24 indicates that the symmetry axis of the potential bow shock points toward the center of the cluster, at an angle $\sim 225°$ east of north (see Fig. 4.4).

In the following section I investigate the possibility of the source to be a stellar bow shock caused by the interaction of a "supersonic" stellar wind with the surrounding medium.

Stellar Bow Shock Scenario

In order to find a stellar counterpart for our bow-shock candidate, I overlaid the VISIR image on an older mosaic in the K_s-band (2.2 μm) taken in 2006 Schödel *et al.* (2009). Figure 4.5 shows at least two potential candidates located, in projection, at the position of X24. I then compare with the list of K-band (2.18 μm) stars from Buchholz *et al.* (2009) (online table *typelist.dat*) and K_s-band (2.2 μm) Schödel *et al.* (2009) (online table *tableb1.dat*). From Fig. 4.6 (also, see Fig. 4.5) I find the best stellar candidates, designated hereafter by Bu09 for sources Buchholz *et al.* (2009) and Sc09 for Schödel *et al.* (2009), to be star Bu09#1211 in Buchholz *et al.* (2009) (no counterpart in Schödel *et al.*, 2009), star Bu09#153 (Sc09#4712) and star Bu09#184 (Sc09#4728). Star Bu09#38 (Sc09#4392) is the brightest with a K-mag of 10.8, however, its location makes the association with the extended feature X24 to be less probable. The remaining stars closeby are very faint and hence are excluded from consideration.
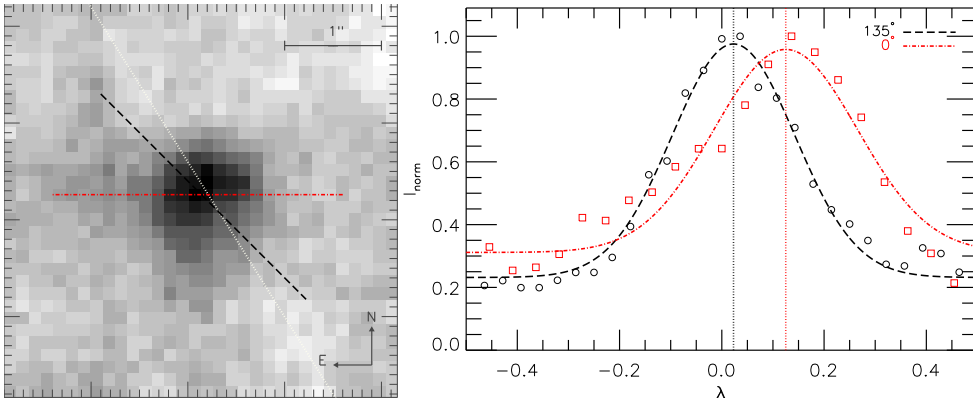
Figure 4.4: *The left panel shows that the feature is symmetric along an axis with an angle 212° east of north (black dashed line). The white dotted line represents the line passing through the center of the cluster, the position of Sgr A*. The black dashed line in the right panel shows the best Gaussian fit to the intensity profile along a path perpendicular to the axis plotted on the image of the source with similar color (black circles). Here λ represents the normalized width of the feature. Similarly, the red dashed-dotted line shows the best Gaussian profile along a path perpendicular to the red line. The offset between the two profiles indicate a quantified measure for deviation from circular symmetry (i.e. a simple point source) which is also evident from the apparent shape of the source.*
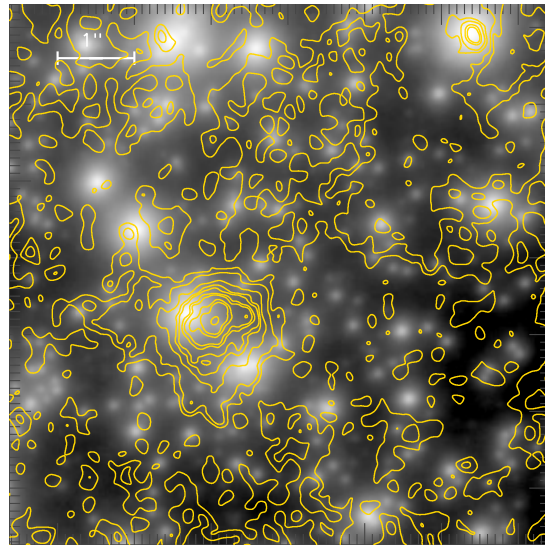
Figure 4.5: *Overlay of VISIR contours of the source X24 and surroundings on a NaCo K_s-band mosaic. The image spans ~ 7″×7″, a larger FOV than Fig. 4.6. North is up and east is to the left.*

Considering that the *K*-band positions in both publications have been based on data taken around the spring of 2004 with a systematic uncertainty of 0.1″ the stars I mentioned appear coincident with or close to the center of the MIR source in projection. This motivated me to study these three stars and investigate whether they could be responsible for the observed shape of X24. Below I address the case for each star individually:
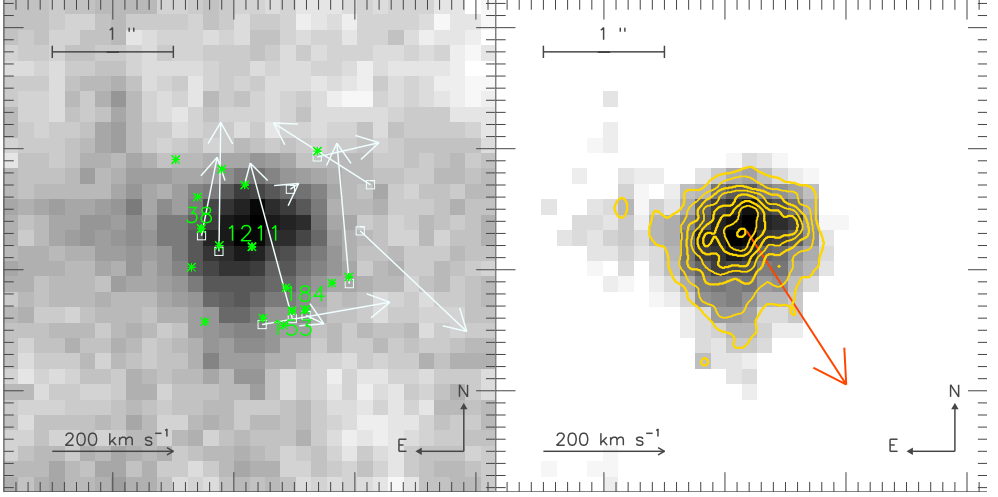
Figure 4.6: *The left panel shows that the feature as the VISIR image with the stars taken from Buchholz et al. (2009) plotted as green stars. The stellar candidates for the bow shock star are labeled with their sequence numbers for easier comparison with the text. The star that have measured proper motion in Schödel et al. (2009) are shown as white arrows. The right panel shows the X24 feature with contours (similar to Fig. 4.1). Also shown on the right panel, as a red arrow, is the proper motion measurement of X24 as obtained by Zhao et al. (2009).*

Star A

With a K-mag =14.7 ($RA_{off} = -9.15''$, $Dec_{off} = -14.81''$) it is classified as a late-type K giant (Star Bu09#1211 in Buchholz *et al.*, 2009). I could not find any reported proper motion measurement for this star. Late-type K giants have typical stellar luminosities of $L_\star = 10^{(2...5)}$ $L_\odot$ and typical stellar wind-loss rates of $\dot{M}_w = 10^{(-10...-7)}$ $M_\odot$ yr^{-1}. I derive the stellar wind velocity v_w using the following (adapted from Reimers, 1975; Suzuki, 2007)

$$\dot{M}_w \simeq 4 \times 10^{-13} \eta_R \frac{L_\star R_\star}{M_\star} \, M_\odot/\text{yr} \tag{4.1}$$

$$v_{esc}^2 = \frac{M_\star}{R_\star} v_{esc\odot}^2 \tag{4.2}$$

$$\dot{M}_w \simeq 4 \times 10^{-13} \eta_R \frac{L_\star v_{esc\odot}^2}{v_{esc}^2} \, M_\odot/\text{yr} \tag{4.3}$$

$$v_{esc} \simeq \left[4 \times 10^{-13} \eta_R \frac{L_\star}{\dot{M}_w} \right]^{1/2} v_{esc\odot}, \tag{4.4}$$

where $L_\star$, $R_\star$ and $M_\star$ are the stellar luminosity in $L_\odot$, radius in $R_\odot$ and mass in $M_\odot$, respectively. η_R is a proportional coefficient of an order of unity ($\frac{1}{3} < \eta_R < 3$) based on a dimensional analysis of stellar wind energetics. v_{esc} is the star escape velocity with typical

values of $0.16 < \frac{v_w}{v_{esc}} < 0.8$. Assuming $v_w = 0.5 v_{esc}$ and $\eta_R = 1$ one gets:

$$v_w = 0.5 \left[4 \times 10^{-13} \frac{L_\star}{\dot{M}_w} \right]^{1/2} \times 617 \, \text{km s}^{-1}, \tag{4.5}$$

which gives a stellar wind velocity.

Using the bow shock solutions derived by Wilkin (1996) for an isotropic stellar wind;

$$R_\circ = \sqrt{\frac{\dot{M}_w v_w}{4\pi \rho_{amb} v_\star^2}} \tag{4.6}$$

with $R_\circ$ being the stand-off distance, $\dot{M}_w$ the wind mass-loss rate, v_w the terminal wind velocity, ρ_{amb} the ambient medium density and $v_\star$ as the velocity of the star causing the shock. Using the formula derived in (Tanner *et al.*, 2005, page 747) to account for the units, the previous equation becomes:

$$R_\circ = 1.74 \times 10^{19} \sqrt{\frac{\dot{M}_w v_w}{\mu_H n_H v_{rel}^2}} \tag{4.7}$$

with $R_\circ$ being the stand-off distance in cm, $\dot{M}_w$ the wind mass-loss rate in units of $10^{-6} \, M_\odot \, \text{yr}^{-1}$, v_w the terminal wind velocity in $10^8 \, \text{cm s}^{-1}$, μ_H the mean molecular weight of Hydrogen, n_H number density of the gas in cm^{-3} and v_{rel} as the velocity of the star relative to the surrounding medium in units of $10^6 \, \text{cm s}^{-1}$. I use a value of $20 \, \text{cm}^{-3}$ for the number density of the ambient medium. This value is lower than $n_H = 26 \, \text{cm}^{-3}$ estimated by Baganoff *et al.* (2003) since X24 located in a less dense region than close to the black hole.

To derive the relative velocity for a range of stand-off distances and a range of stellar-wind velocities, I re-arrange Eq. (4.7) to become

$$v_{rel} = \frac{1.74 \times 10^{19}}{R_\circ} \sqrt{\frac{\dot{M}_w v_w}{\mu_H n_H}} \quad . \tag{4.8}$$

The results are shown in Fig. 4.7. From Fig. 4.6, $R_\circ$ is approximately $0.5''$, which leads to a range of relative velocities between the star and the surrounding medium of $v_{rel} \approx (3 - 103) \, \text{km s}^{-1}$.

Star B

With a K-mag of 11.9 ($RA_{off} = -9.48$, $Dec_{off} = -15.34$) it is classified as a late-type M giant (Star Bu09#153 in Buchholz *et al.*, 2009). The star has a K_s magnitude of 12.46 ± 0.15 (Star Sc09#4712 in Schödel *et al.*, 2009) due to an improved extinction value used in that work. The reported right ascension and declination proper motions are $RA_{pm} =$
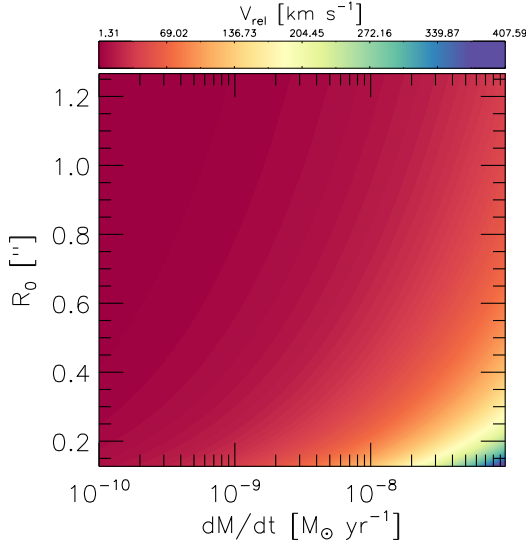
Figure 4.7: *Relative velocity between a star and the medium for a late-type K-giant, star A, for a range of stand-off distances (R_0) and stellar mass-loss rates ($\frac{dM}{dt}$).*
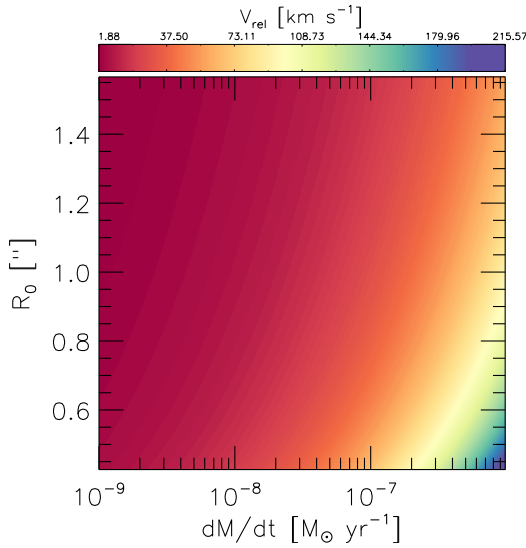
Figure 4.8: *Relative velocity between a star and the medium for a late-type M-giant, star B, for a range stand-off distances (R_0) and stellar mass-loss rates ($\frac{dM}{dt}$).*

57.9 ± 8.3 km s^{-1} and Dec$_{pm}$ = 213.9 ± 20.2 km s^{-1}, respectively (see Fig. 4.6). Late-type M giants have typical stellar luminosities of $L_\star = 10^{(2...5)}$ $L_\odot$ and typical stellar wind-loss rates of $\dot{M}_w = 10^{(-9...-6)}$ $M_\odot$ yr^{-1}. To calculate the stellar wind velocity I use the approach I described in the case of star A and show the results in Fig. 4.8. For $R_\circ$ of 1.2", I get a range of relative velocities between the star and the surrounding medium of $v_{rel} \approx 2 - 77$ km s^{-1}.

Star C

With a K-mag of 12.3 (RA_{off} = −9.59, Dec_{off} = −15.33) it is classified as a early-type O supergiant (Star Bu09#184 in Buchholz *et al.*, 2009). The star has a K_s magnitude of 12.79 ± 0.14 (Star Sc09#4728 in Schödel *et al.*, 2009) due to an improved extinction value used in that work. The reported right ascension and declination proper motions are RA_{pm} = −24.5 ± 11.3 km s^{-1} and Dec_{pm} = −11.6 ± 14.8 km s^{-1}, respectively (see Fig. 4.6).

Following Lamers and Cassinelli (1999), the stellar wind parameters of O and B galactic stars can be described by:

$$\log(\dot{M}_w v_w R_\star^{0.5}) = -1.37 + 2.07\log(L_\star/10^6),\qquad(4.9)$$

where $\dot{M}_w$ is in $M_\odot$ yr^{-1}, v_w in km s^{-1}, $R_\star$ in $R_\odot$, and $L_\star$ in $L_\odot$. Early-type O supergiants have typical stellar luminosities of $L_\star = 10^{(5.8)}$ $L_\odot$ (Weidner and Vink, 2010; Bouret *et al.*, 2012) and typical stellar radii ∼ 25 $R_\odot$ (from *Allen's Astrophysical Quantities*). Using these typical values, one gets $\dot{M}_w v_w \simeq 3.29 \times 10^{-3}$ $M_\odot$ yr^{-1} km s^{-1}.

This star is located further away from the X24, hence I choose a range for $R_\circ$ (stand-off distance) between 0.4″ to 1.6″, similar to star B. The resulting relative velocity, according to Eq. (4.8), is v_{rel} = 365 − 1339 km s^{-1}. At a stand-off distance ∼ 1.2″, the relative velocity is about 476 km s^{-1}.

Star D (Bu09#184), as evident from Fig. 4.6, seems to be moving away from the Center, almost to the west of the feature X24. However, the measured velocities are small and the source can be considered stationary.

Nature of the External Wind

Considering the above three cases, star B has the highest proper motion velocities (∼ 220 km s^{-1}, to the north-east), but it gives a low relative velocity. Star C, on the other hand, yields a high relative velocity. Assuming that the stellar counterpart of X24 has the same proper motion as measured in radio band Zhao *et al.* (2009) and considering that they report a proper motion south-westward from Sgr A*, the external wind velocity ranges (considering the different classes of stellar counterpart) from ∼ 250 to 1600 km s^{-1}. For the more likely scenario of an early-type O supergiant counterpart the plausible estimate for the external wind speed ranges ∼ 500–1000 km s^{-1}.

In Fig. 4.9 I compare the position of our N-band bow-shock candidate with other sources of interest in the field. Mužić *et al.* (2007) reported two bow shock features X3 and X7 (marked on Fig. 4.9 and zoomed on the upper-right side of the figure) that were detected in their L'-band (3.8 μm) mosaics. The two sources are located within few arcseconds from Sgr A* to its south-west, in the same direction as X24. They were later analyzed in detail in Mužić *et al.* (2010) taking into account their observed morphologies at

Figure 4.9: *The same as Fig. 4.1 plotted with the PAH1 filter. Marked on the map are the bow shock sources X3 and X7, also zoomed to the upper-right corner, along with our feature X24 to the SW of Sgr A* (zoomed to the bottom-right). Indicated on the figure as a dotted line is the proposed direction for the radio jet of Yusef-Zadeh et al. (2012a) while the one by Li et al. (2013b) is shown as a dot-dashed line. The solid line shows the orientation of Sgr A* system as theorized by Zamaninasab et al. (2011). The contours on the bottom right are of the same parameters as in Fig. 4.1.*

3.8 μm, proper motions and types of their stellar counterparts detected at 2.2 μm. Both sources can be explained using a stellar bow shock model caused by a partially-collimated outflow coming from the direction of Sgr A*, at a distance of 0.8″ for X7. Another observational evidence supporting the same outflow/jet direction as Mužić *et al.* (2010) is reported by Yusef-Zadeh *et al.* (2012a) in the radio regime. They use radio continuum images at 8.4 GHz and detect a faint continuous linear structure coinciding with weak radio blobs along an angle of ∼ 60° from the galactic plane, indicated on Fig. 4.9 by a dotted line. From the theoretical point of view, Zamaninasab *et al.* (2011) use a ray-tracing GR code to analyze the NIR polarized lightcurves from the black hole associated with Sgr A*. They find the orientation of the Sgr A* system to be $\theta = 50°^{+30°}_{-20°}$, which I indicate on Fig. 4.9 by a solid line.

Table 4.1: *List of known bright bow-shock sources in the Galactic Center with their positions in arcsec offset from Sgr A* and where they are analyzed in the literature. The positions have been reported from the latest publication.*

Bow-shock source	$\Delta\alpha$ (arcsec)	$\Delta\delta$ (arcsec)	studied in
IRS 1W	5.26″	0.61″	Tanner *et al.* (2005); Buchholz *et al.* (2011) Sanchez-Bermudez *et al.* (2014)
IRS 5	8.62″	9.83″	Tanner *et al.* (2005); Sanchez-Bermudez *et al.* (2014)
IRS 8	1.11″	29.09″	Tanner *et al.* (2005); Geballe *et al.* (2006) Rauch *et al.* (2013)
IRS 10W	6.50″	5.15″	Tanner *et al.* (2005); Sanchez-Bermudez *et al.* (2014)
IRS 21	2.35″	−2.69″	Tanner *et al.* (2005); Buchholz *et al.* (2011) Sanchez-Bermudez *et al.* (2014)
unknown	3.4″	2.9″	Clénet *et al.* (2004)
X3	−2.5″	−2.3″	Mužić *et al.* (2010)
X7	−0.5″	−0.5″	Mužić *et al.* (2010)
X24	−9.18″	−14.68″	this work

Most bow shocks in the Center are found in the mini-spiral northern arm where they

interact mainly with the ionized gas there. Table 4.1 lists all the known bow shocks in the GC. The location of our potential bow shock at a distance of $\sim 17''$ (0.68 parsec) from Sgr A* makes it instead experience the combined ram pressure of the stellar winds of about two dozen GC WR-stars. The combined isotropic wind of all these stars is estimated to be of $v_w = 1000$ km s^{-1}and mass-loss rate $\sim 3 \times 10^{-3}$ $M_\odot$ yr^{-1}(Fryer *et al.*, 2007). I follow the same approach as Mužić *et al.* (2010) in their Sect. 7.3 to estimate the terminal velocity of the wind at $17''$. I use their values for the wind velocity and mass-loss rate ($\dot{M}_w = 10^{-3}$ $M_\odot$ yr^{-1}and $v_w = 750$ km s^{-1}) in the equation $n_H v_s^2 \approx 1.7 \times 10^9 \times (d[''])^{-2}$ cm^{-3} km^2 s^{-2}. With $n_H = 26$ cm^{-3}, the resulting velocity is $v_s = 475$ km s^{-1}at a distance $d = 17''$. This matches the lower-limit values I get for the external wind.

Crocker *et al.* (2011) estimate the total kinetic power of such massive stars winds at the Center to be 1.3×10^{39} erg yr^{-1}. They assume a wind speed of 700 km s^{-1}and a $\Delta \dot{M}_w \simeq 0.01$ $M_\odot$ yr^{-1}considering that about half of the Center's massive stars are located outside the three stellar clusters, the nuclear cluster, the Quintuplet and Arches clusters, as pointed out by Wang *et al.* (2010) using Pa α emission.

While our source, X24, is located at a distance far enough from the Center to experience the combined wind of all GC stars, X3 and X7 of Mužić *et al.* (2010) are much closer, at $\sim 5''$ and $1''$ respectively. Their positions lie within the outward-bound wind component of the accreting matter that never reaches the SMBH (Shcherbakov and Baganoff, 2010; Eckart *et al.*, 2014). The rms of the stellar wind at $\sim 17''$, the distance of our source to Sgr A*, is lower and of the order of few hundred km s^{-1}(Fig. 3 in Shcherbakov and Baganoff, 2010).

4.3 Summary and Conclusion

Li, Ostriker, and Sunyaev (2013a) find that in the case of a low inflow rate of the accreting matter into a SMBH, viscous forces can drive an equatorial outflow that propagates out beyond the Bondi radius ($1.5''$ for Sgr A*). Such an outflow has been detected in NGC 5929 (Riffel *et al.*, 2014). Taking the equatorial outflows concept and in the light of the recent claim of detecting a parsec-scale jet from Sgr A* by (Li *et al.*, 2013b, see note in Sect. 4.1), our feature, along with X3 and X7, interestingly lie in a direction perpendicular to that jet. Morris *et al.* (2014) discuss several filaments detected in the radio with the newly improved Very Large Array[2] (VLA) within few parsec from the SMBH roughly to its south and north, they are denoted as the Southern and Northern Curls. They are believed to be ordered magnetic field structures illuminated along its length by synchrotron emission. The line connecting the tips of both curls hint toward a collimated outflow of plasma from the position of Sgr A*.

Several observational arguments support the presence of an outflow originating from the inner portions of the GC (Eckart *et al.*, 1992; Mužić *et al.*, 2007, 2010; Su *et al.*, 2010;

---

[2]http://www.vla.nrao.edu

Markoff, 2010; Crocker *et al.*, 2011). The alignment of our feature with two previously found bow-shock sources (marked by X7 and X3 in Fig. 4.9; see Mužić *et al.*, 2010) and the mini-cavity may imply that all four features are produced by the same mechanism/event. All of these objects are aligned perpendicular to the plane of young mass-losing stars very close to the central SMBH. We estimate the velocity of a collimated flow that can cause such features, either from the disk of stars or the position of Sgr A*, to be $\sim$ 500–1000 km s^{-1}. It is comparable with the estimates for the asymptotic speed of the nuclear star cluster's wind ($\sim$ 700 km s^{-1}). Our value is slightly lower than the speed reported in Mužić *et al.* (2010), a possible indicator of mass loading between $\sim$ 0.06 pc and $\sim$ 0.68 pc.

Although, by any astronomical standards, Sgr A* is not an active black hole, there is, however, a growing body of evidence for the presence of an outflow from the material accreting onto the SMBH (Wang *et al.*, 2013), even indications for a jet (Yusef-Zadeh *et al.*, 2012a; Li *et al.*, 2013b) with the evidence pointing to different position angles for the flow. The interaction of such an outflow with the ISM and the wind of massive stars would produce signatures similar to our observations. The lack of a larger number of similar objects in the field can be explained either by the short life span of massive stars and/or the intermittent nature of the responsible mechanism.

The work presented in this chapter has been partly published in Sabha, Zamaninasab, Eckart, and Moser (2014) and will be fully presented in an upcoming paper (Sabha *et al.* 2015b, in prep.).

FINAL REMARKS

In this thesis I first investigate the impact of stellar scattering on the trajectory of high velocity stars orbiting very close to the Galactic supermassive black hole. It is shown that the so-called resonant relaxation effect caused by the accumulative perturbation of the stars on each other can cause a significant impact on their orbits. For the case of the star S2, orbital fitting allows for a dark mass enclosed within its orbit and surrounding the black hole ($\sim 10^3$ $M_\odot$ to 10^5 $M_\odot$). If the mass contains a significant population of 10 $M_\odot$ black holes (see e.g. Freitag *et al.*, 2006), then the impact of resonant relaxation would compete with the known relativistic or Newtonian peribothron shifts. Since this is a plausible scenario, any attempt aiming at measuring such relativistic peribothron shifts would be upset by the aforementioned degeneracy. While this may be considered bad news for any trial relying on a single orbit, this degeneracy could be resolved by simultaneous observations of a larger number of stars. One must note that the effect of resonant relaxation highly depends on the granularity and radial distribution of the enclosed dark mass around the black hole. Hence it can be used to probe the number and mass of the perturbers.

The above discussion emphasizes the importance of obtaining a better constraint on the amount and structure/composition of the dark mass surrounding the Central black hole. I show that the combined light of the fainter S-cluster members (their number can be approximated by extrapolating the observed K_s-band luminosity function for the faint members) can only account for up to one third of the diffuse residual flux density that I measure after the PSF subtraction. However, with the current angular resolution and sensitivity one can not rule out the possibility of a non-stellar origin of the additional background light. It may originate from the accretion of matter onto a number of ~10 $M_\odot$ black
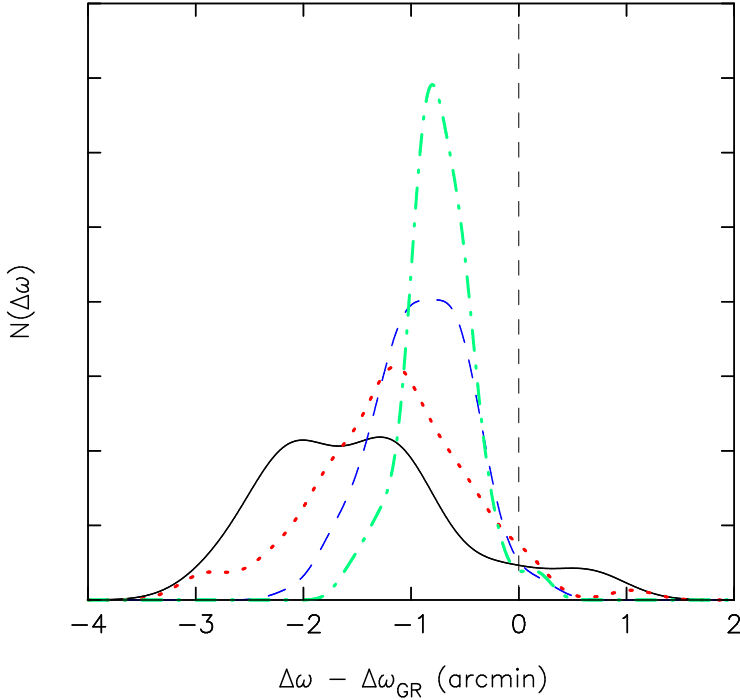
Figure 5.1: *Same as Fig. 2.9, the average value of S2's argument of peribothron shift increases with increasing mass and number of the perturbers as predicted by resonant relaxation effect.*

holes. In the future, such uncertainty will only be resolved with higher angular resolution and more sensitive future observations.

On a related subject, I simulate how frequently a random line-of-sight association of several faint stars can resemble a false detection, a so-called blend star. In these simulations, I make use of the known radial distribution of stars in the cluster and their mass function and estimate that such blend stars would dissolve after about 3 years due to their proper motion. For example, in Sabha *et al.* (2010) I reported three stars that were either previously not known, or misidentified with previously known members of the cluster (one of them is S62, as pointed out in Dodds-Eden *et al.*, 2011). In addition, there are other reports of similar incidents, the case of the star S3 which was identified in the *K*-band in the early epochs 1992 (Eckart and Genzel, 1996), 1995 (Ghez *et al.*, 1998) and lost after about 3 years in 1996/7 Ghez *et al.* (1998); Genzel *et al.* (2000).

While upcoming 30 m class telescopes (e.g. ELT, TMT, JWST) promise images of the region with higher angular resolution and greater sensitivity, near future observations taking advantage of interferometric techniques (e.g. LINC-NIRVANA and GRAVITY experiments) can provide a significant boost in angular resolution, enough to probe some faint stellar
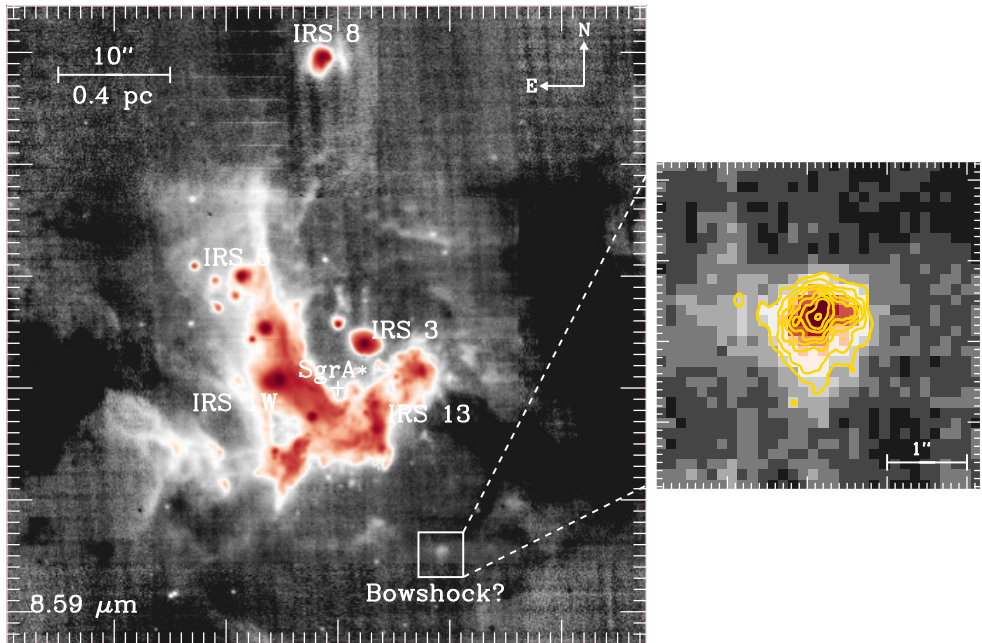
Figure 5.2: *The bow shock candidate X24 might probe the dark outflow originating from the vicinity of the supermassive black hole.*

objects or resolve potential "blend stars".

Parts of this thesis are dedicated to the analysis of the mid-infrared VISIR observations of the Galactic Center. The observations presented here are part of a bigger program, ESO ProgId:085.C-0047, designed to map five GC targets in preparation for future MIRI observations. Since the Galactic Center is a fairly crowded field, it is essential to plan each observing run delicately in order to avoid bright sources in the field of view that would saturate the sensitive detectors of MIRI. My results are the first mid-infrared observations with large FOV and high angular resolution of the region, and can provide critical information for planning future MIRI JWST observations. In addition to mapping the empty regions, these observations spot several new compact dusty objects in the nuclear star cluster and the Quintuplet. A comparison between the two available wavelengths provides some basic insight on these newly found objects. However, the information extracted from these two bands provides a still inconclusive picture.

I present a detailed analysis of one of these newly found objects in the last chapter. This source resembles a bow-shock morphology with its axis aligned with a position angle of 212° east of north. Interestingly, this source could be cross-identified with a curious object with similar morphology in radio maps of the same region. This source is also aligned

with two other bow-shock like objects and the mini-cavity (argued to be a shock front inside the mini-spiral region). Such alignment may imply that all four features are produced by the same mechanism/event, e.g. a collimated outflow. I estimate the velocity of such an outflow originating from the vicinity of Sgr A* to be ~500 – 1000 km s^{-1}, which is comparable with both the asymptotic estimates for the nuclear star cluster's wind (~ 700 km s^{-1}) and the mechanical power of a dark flow originating from the supermassive black hole itself.

A full multi-wavelength investigation of this source (and similar newly found objects) might shed some light on the recent history of star formation in the very center of our Galaxy. Similar investigations also have the potential to probe dark outflows in the region. Although these powerful flows might play a significant role in star formation processes or even the formation of larger scale galactic structures, they remain extremely difficult to probe. Future observations and more studies promise a better understanding of these phenomena.

BIBLIOGRAPHY

Alexander, T. (2005). Stellar processes near the massive black hole in the Galactic center [review article]. *Phys. Rep.*, **419**, 65–142.

Alexander, T. (2007). Stellar Relaxation Processes Near the Galactic Massive Black Hole. *arXiv e-prints:0708.0688*.

Alexander, T. and Hopman, C. (2009). Strong Mass Segregation Around a Massive Black Hole. *ApJ*, **697**, 1861–1869.

Antonini, F., Capuzzo-Dolcetta, R., Mastrobuono-Battisti, A., and Merritt, D. (2012). Dissipationless Formation and Evolution of the Milky Way Nuclear Star Cluster. *ApJ*, **750**, 111.

Baganoff, F. K., Bautz, M. W., Brandt, W. N., Chartas, G., Feigelson, E. D., Garmire, G. P., Maeda, Y., Morris, M., Ricker, G. R., Townsley, L. K., and Walter, F. (2001). Rapid X-ray flaring from the direction of the supermassive black hole at the Galactic Centre. *Nature*, **413**, 45–48.

Baganoff, F. K., Maeda, Y., Morris, M., Bautz, M. W., Brandt, W. N., Cui, W., Doty, J. P., Feigelson, E. D., Garmire, G. P., Pravdo, S. H., Ricker, G. R., and Townsley, L. K. (2003). Chandra X-Ray Spectroscopic Imaging of Sagittarius A* and the Central Parsec of the Galaxy. *ApJ*, **591**, 891–915.

Bahcall, J. N. and Wolf, R. A. (1976). Star distribution around a massive black hole in a globular cluster. *ApJ*, **209**, 214–232.

Bahcall, J. N. and Wolf, R. A. (1977). The star distribution around a massive black hole in a globular cluster. II Unequal star masses. *ApJ*, **216**, 883–907.

Bartko, H., Martins, F., Trippe, S., Fritz, T. K., Genzel, R., Ott, T., Eisenhauer, F., Gillessen, S., Paumard, T., Alexander, T., Dodds-Eden, K., Gerhard, O., Levin, Y., Mascetti, L., Nayakshin, S., Perets, H. B., Perrin, G., Pfuhl, O., Reid, M. J., Rouan, D., Zilka, M., and Sternberg, A. (2010). An Extremely Top-Heavy Initial Mass Function in the Galactic Center Stellar Disks. *ApJ*, **708**, 834–840.

Baumgardt, H., Gualandris, A., and Portegies Zwart, S. (2006). Ejection of hypervelocity stars from the Galactic Centre by intermediate-mass black holes. *MNRAS*, **372**, 174–182.

Becklin, E. E. and Neugebauer, G. (1968). Infrared Observations of the Galactic Center. *ApJ*, **151**, 145.

Becklin, E. E., Neugebauer, G., Willner, S. P., and Matthews, K. (1978). Infrared observations of the galactic center. IV - The interstellar extinction. *ApJ*, **220**, 831–835.

Blum, R. D., Sellgren, K., and Depoy, D. L. (1996). JHKL Photometry and the K-Band Luminosity Function at the Galactic Center. *ApJ*, **470**, 864–+.

Bouret, J.-C., Hillier, D. J., Lanz, T., and Fullerton, A. W. (2012). Properties of Galactic early-type O-supergiants. A combined FUV-UV and optical analysis. *A&A*, **544**, A67.

Bower, G. C., Markoff, S., Brunthaler, A., Law, C., Falcke, H., Maitra, D., Clavel, M., Goldwurm, A., Morris, M. R., Witzel, G., Meyer, L., and Ghez, A. M. (2014). The Intrinsic Two-dimensional Size of Sagittarius A*. *ApJ*, **790**, 1.

Buchholz, R. M., Schödel, R., and Eckart, A. (2009). Composition of the galactic center star cluster. Population analysis from adaptive optics narrow band spectral energy distributions. *A&A*, **499**, 483–501.

Buchholz, R. M., Witzel, G., Schödel, R., Eckart, A., Bremer, M., and Mužić, K. (2011). Adaptive-optics assisted near-infrared polarization measurements of sources in the Galactic center. *A&A*, **534**, A117.

Carollo, D., Beers, T. C., Lee, Y. S., Chiba, M., Norris, J. E., Wilhelm, R., Sivarani, T., Marsteller, B., Munn, J. A., Bailer-Jones, C. A. L., Fiorentin, P. R., and York, D. G. (2007). Two stellar components in the halo of the Milky Way. *Nature*, **450**, 1020–1025.

Chandrasekhar, S. (1943). Dynamical Friction. I. General Considerations: the Coefficient of Dynamical Friction. *ApJ*, **97**, 255.

Clénet, Y., Rouan, D., Gendron, E., Lacombe, F., Lagrange, A.-M., Mouillet, D., Magnard, Y., Rousset, G., Fusco, T., Montri, J., Genzel, R., Schödel, R., Ott, T., Eckart, A., Marco, O., and Tacconi-Garman, L. (2004). The infrared L'-band view of the Galactic Center with NAOS-CONICA at VLT. *A&A*, **417**, L15–L19.

Contini, M. (2011). The low-luminosity active galactic nucleus in the centre of the Galaxy. *MNRAS*, **418**, 1935–1947.

Cotera, A. S., Erickson, E. F., Colgan, S. W. J., Simpson, J. P., Allen, D. A., and Burton, M. G. (1996). The Discovery of Hot Stars near the Galactic Center Thermal Radio Filaments. *ApJ*, **461**, 750.

Crocker, R. M., Jones, D. I., Aharonian, F., Law, C. J., Melia, F., Oka, T., and Ott, J. (2011). Wild at Heart: the particle astrophysics of the Galactic Centre. *MNRAS*, **413**, 763–788.

Dale, J. E., Davies, M. B., Church, R. P., and Freitag, M. (2009). Red giant stellar collisions in the Galactic Centre. *MNRAS*, **393**, 1016–1033.

Degenaar, N., Reynolds, M. T., Miller, J. M., Kennea, J. A., and Wijnands, R. (2013). Large Flare from Sgr A* Detected by Swift. *The Astronomer's Telegram*, **5006**, 1.

Do, T., Ghez, A. M., Morris, M. R., Lu, J. R., Matthews, K., Yelda, S., and Larkin, J. (2009). High Angular Resolution Integral-Field Spectroscopy of the Galaxy's Nuclear Cluster: A Missing Stellar Cusp? *ApJ*, **703**, 1323–1337.

Dodds-Eden, K., Gillessen, S., Fritz, T. K., Eisenhauer, F., Trippe, S., Genzel, R., Ott, T., Bartko, H., Pfuhl, O., Bower, G., Goldwurm, A., Porquet, D., Trap, G., and Yusef-Zadeh, F. (2011). The Two States of Sgr A* in the Near-infrared: Bright Episodic Flares on Top of Low-level Continuous Variability. *ApJ*, **728**, 37–+.

Doeleman, S. S., Weintroub, J., Rogers, A. E. E., Plambeck, R., Freund, R., Tilanus, R. P. J., Friberg, P., Ziurys, L. M., Moran, J. M., Corey, B., Young, K. H., Smythe, D. L., Titus, M., Marrone, D. P., Cappallo, R. J., Bock, D. C.-J., Bower, G. C., Chamberlin, R., Davis, G. R., Krichbaum, T. P., Lamb, J., Maness, H., Niell, A. E., Roy, A., Strittmatter, P., Werthimer, D., Whitney, A. R., and Woody, D. (2008). Event-horizon-scale structure in the supermassive black hole candidate at the Galactic Centre. *Nature*, **455**, 78–80.

Dressler, A., Faber, S. M., Burstein, D., Davies, R. L., Lynden-Bell, D., Terlevich, R. J., and Wegner, G. (1987). Spectroscopy and photometry of elliptical galaxies - A large-scale streaming motion in the local universe. *ApJ*, **313**, L37–L42.

Duric, N. (2004). *Advanced astrophysics*.

Eatough, R. P., Falcke, H., Karuppusamy, R., Lee, K. J., Champion, D. J., Keane, E. F., Desvignes, G., Schnitzeler, D. H. F. M., Spitler, L. G., Kramer, M., Klein, B., Bassa, C., Bower, G. C., Brunthaler, A., Cognard, I., Deller, A. T., Demorest, P. B., Freire, P. C. C., Kraus, A., Lyne, A. G., Noutsos, A., Stappers, B., and Wex, N. (2013). A strong magnetic field around the supermassive black hole at the centre of the Galaxy. *Nature*, **501**, 391–394.

Eckart, A. and Genzel, R. (1996). Observations of stellar proper motions near the Galactic Centre. *Nature*, **383**, 415–417.

Eckart, A., Genzel, R., Krabbe, A., Hofmann, R., van der Werf, P. P., and Drapatz, S. (1992). Spatially resolved near-infrared emission and a bubble of hot gas in the central active region of the Galaxy. *Nature*, **355**, 526–529.

Eckart, A., Baganoff, F. K., Morris, M., Bautz, M. W., Brandt, W. N., Garmire, G. P., Genzel, R., Ott, T., Ricker, G. R., Straubmeier, C., Viehmann, T., Schödel, R., Bower, G. C., and Goldston, J. E. (2004). First simultaneous NIR/X-ray detection of a flare from Sgr A*. *A&A*, **427**, 1–11.

Eckart, A., Schödel, R., Meyer, L., Trippe, S., Ott, T., and Genzel, R. (2006). Polarimetry of near-infrared flares from Sagittarius A*. *A&A*, **455**, 1–10.

Eckart, A., Sabha, N., Witzel, G., Straubmeier, C., Shahzamanian, B., Valencia-S., M., García-Marín, M., Horrobin, M., Moser, L., Zuther, J., Fischer, S., Rauch, C., Rost, S., Iserlohe, C., Yazici, S., Smajic, S., Wiest, M., Araujo-Hauck, C., and Wank, I. (2012). Beating the confusion limit: the necessity of high angular resolution for probing the physics of Sagittarius A* and its environment: opportunities for LINC-NIRVANA (LBT), GRAVITY (VLTI) and and METIS (E-ELT). In *Society of Photo-Optical Instrumentation Engineers (SPIE) Conference Series*, volume 8445 of *Society of Photo-Optical Instrumentation Engineers (SPIE) Conference Series*.

Eckart, A., Mužić, K., Yazici, S., Sabha, N., Shahzamanian, B., Witzel, G., Moser, L., Garcia-Marin, M., Valencia-S., M., Jalali, B., Bremer, M., Straubmeier, C., Rauch, C., Buchholz, R., Kunneriath, D., and Moultaka, J. (2013). Near-infrared proper motions and spectroscopy of infrared excess sources at the Galactic center. *A&A*, **551**, A18.

Eckart, A., Horrobin, M., Britzen, S., Zamaninasab, M., Mužić, K., Sabha, N., Shahzamanian, B., Yazici, S., Moser, L., García-Marin, M., Valencia-S., M., Borkar, A., Bursa, M., Karssen, G., Karas, V., Zajaček, M., Bronfman, L., Finger, R., Jalali, B., Vitale, M., Rauch, C., Kunneriath, D., Moultaka, J., Straubmeier, C., Rashed, Y. E., Markakis, K., and Zensus, A. (2014). The infrared K-band identification of the DSO/G2 source from VLT and Keck data. In L. O. Sjouwerman, C. C. Lang, and J. Ott, editors, *IAU Symposium*, volume 303 of *IAU Symposium*, pages 269–273.

Eilon, E., Kupi, G., and Alexander, T. (2009). The Efficiency of Resonant Relaxation Around a Massive Black Hole. *ApJ*, **698**, 641–647.

Eisenhauer, F., Genzel, R., Alexander, T., Abuter, R., Paumard, T., Ott, T., Gilbert, A., Gillessen, S., Horrobin, M., Trippe, S., Bonnet, H., Dumas, C., Hubin, N., Kaufer, A., Kissler-Patig, M., Monnet, G., Ströbele, S., Szeifert, T., Eckart, A., Schödel, R., and Zucker, S. (2005). SINFONI in the Galactic Center: Young Stars and Infrared Flares in the Central Light-Month. *ApJ*, **628**, 246–259.

Figer, D. F., Morris, M., Geballe, T. R., Rich, R. M., Serabyn, E., McLean, I. S., Puetter, R. C., and Yahil, A. (1999a). High-Resolution Infrared Imaging and Spectroscopy of the Pistol Nebula: Evidence for Ejection. *ApJ*, **525**, 759–771.

Figer, D. F., Kim, S. S., Morris, M., Serabyn, E., Rich, R. M., and McLean, I. S. (1999b). Hubble Space Telescope/NICMOS Observations of Massive Stellar Clusters near the Galactic Center. *ApJ*, **525**, 750–758.

Figer, D. F., McLean, I. S., and Morris, M. (1999c). Massive Stars in the Quintuplet Cluster. *ApJ*, **514**, 202–220.

Figer, D. F., Najarro, F., Gilmore, D., Morris, M., Kim, S. S., Serabyn, E., McLean, I. S., Gilbert, A. M., Graham, J. R., Larkin, J. E., Levenson, N. A., and Teplitz, H. I. (2002). Massive Stars in the Arches Cluster. *ApJ*, **581**, 258–275.

Finkbeiner, A. (2012). Galaxy formation: The new Milky Way. *Nature*, **490**, 24–27.

Freitag, M. (2008). Stellar Collisions in Young Clusters: Formation of (Very) Massive Stars? In H. Beuther, H. Linz, & T. Henning, editor, *Massive Star Formation: Observations Confront Theory*, volume 387 of *Astronomical Society of the Pacific Conference Series*, page 247.

Freitag, M., Amaro-Seoane, P., and Kalogera, V. (2006). Stellar Remnants in Galactic Nuclei: Mass Segregation. *ApJ*, **649**, 91–117.

Fried, D. L. (1966). Optical Resolution Through a Randomly Inhomogeneous Medium for Very Long and Very Short Exposures. *Journal of the Optical Society of America (1917-1983)*, **56**, 1372.

Fritz, T. K., Gillessen, S., Dodds-Eden, K., Martins, F., Bartko, H., Genzel, R., Paumard, T., Ott, T., Pfuhl, O., Trippe, S., Eisenhauer, F., and Gratadour, D. (2010). GC-IRS13E – A Puzzling Association of Three Early-type Stars. *ApJ*, **721**, 395–411.

Fritz, T. K., Gillessen, S., Dodds-Eden, K., Lutz, D., Genzel, R., Raab, W., Ott, T., Pfuhl, O., Eisenhauer, F., and Yusef-Zadeh, F. (2011). Line Derived Infrared Extinction toward the Galactic Center. *ApJ*, **737**, 73.

Fryer, C. L., Rockefeller, G., Hungerford, A., and Melia, F. (2006). The Sgr B2 X-Ray Echo of the Galactic Center Supernova Explosion that Produced Sgr A East. *ApJ*, **638**, 786–796.

Fryer, C. L., Liu, S., Rockefeller, G., Hungerford, A., and Belanger, G. (2007). Probing the Density in the Galactic Center Region: Wind-blown Bubbles and High-Energy Proton Constraints. *ApJ*, **659**, 389–406.

Fujii, M., Iwasawa, M., Funato, Y., and Makino, J. (2009). Trojan Stars in the Galactic Center. *ApJ*, **695**, 1421–1429.

Fujii, M., Iwasawa, M., Funato, Y., and Makino, J. (2010). The Origin of S-stars and a Young Stellar Disk: Distribution of Debris Stars of a Sinking Star Cluster. *ApJ*, **716**, L80–L84.

Geballe, T. R., Najarro, F., Rigaut, F., and Roy, J.-R. (2006). The K-Band Spectrum of the Hot Star in IRS 8: An Outsider in the Galactic Center? *ApJ*, **652**, 370–375.

Genzel, R., Thatte, N., Krabbe, A., Kroker, H., and Tacconi-Garman, L. E. (1996). The Dark Mass Concentration in the Central Parsec of the Milky Way. *ApJ*, **472**, 153–+.

Genzel, R., Pichon, C., Eckart, A., Gerhard, O. E., and Ott, T. (2000). Stellar dynamics in the Galactic Centre: proper motions and anisotropy. *MNRAS*, **317**, 348–374.

Genzel, R., Schödel, R., Ott, T., Eisenhauer, F., Hofmann, R., Lehnert, M., Eckart, A., Alexander, T., Sternberg, A., Lenzen, R., Clénet, Y., Lacombe, F., Rouan, D., Renzini, A., and Tacconi-Garman, L. E. (2003). The Stellar Cusp around the Supermassive Black Hole in the Galactic Center. *ApJ*, **594**, 812–832.

Ghez, A. M., Klein, B. L., Morris, M., and Becklin, E. E. (1998). High Proper-Motion Stars in the Vicinity of Sagittarius A*: Evidence for a Supermassive Black Hole at the Center of Our Galaxy. *ApJ*, **509**, 678–686.

Ghez, A. M., Duchêne, G., Matthews, K., Hornstein, S. D., Tanner, A., Larkin, J., Morris, M., Becklin, E. E., Salim, S., Kremenek, T., Thompson, D., Soifer, B. T., Neugebauer, G., and McLean, I. (2003). The First Measurement of Spectral Lines in a Short-Period Star Bound to the Galaxy's Central Black Hole: A Paradox of Youth. *ApJ*, **586**, L127–L131.

Gillessen, S., Eisenhauer, F., Trippe, S., Alexander, T., Genzel, R., Martins, F., and Ott, T. (2009a). Monitoring Stellar Orbits Around the Massive Black Hole in the Galactic Center. *ApJ*, **692**, 1075–1109.

Gillessen, S., Eisenhauer, F., Fritz, T. K., Bartko, H., Dodds-Eden, K., Pfuhl, O., Ott, T., and Genzel, R. (2009b). The Orbit of the Star S2 Around SGR A* from Very Large Telescope and Keck Data. *ApJ*, **707**, L114–L117.

Gillessen, S., Genzel, R., Fritz, T. K., Quataert, E., Alig, C., Burkert, A., Cuadra, J., Eisenhauer, F., Pfuhl, O., Dodds-Eden, K., Gammie, C. F., and Ott, T. (2012). A gas cloud on its way towards the supermassive black hole at the Galactic Centre. *Nature*, **481**, 51–54.

Gould, A. and Quillen, A. C. (2003). Sagittarius A* Companion S0-2: A Probe of Very High Mass Star Formation. *ApJ*, **592**, 935–940.

Gualandris, A., Gillessen, S., and Merritt, D. (2010). The Galactic Centre star S2 as a dynamical probe for intermediate-mass black holes. *MNRAS*, **409**, 1146–1154.

Guesten, R., Genzel, R., Wright, M. C. H., Jaffe, D. T., Stutzki, J., and Harris, A. I. (1987). Aperture synthesis observations of the circumnuclear ring in the Galactic center. *ApJ*, **318**, 124–138.

Hansen, B. M. S. and Milosavljević, M. (2003). The Need for a Second Black Hole at the Galactic Center. *ApJ*, **593**, L77–L80.

Herrnstein, R. M. and Ho, P. T. P. (2002). Hot Molecular Gas in the Galactic Center. *ApJ*, **579**, L83–L86.

Ho, L. C. (2008). Nuclear Activity in Nearby Galaxies. *ARA&A*, **46**, 475–539.

Ho, L. C. and Filippenko, A. V. (1996). Dynamical Evidence for Massive, Young Globular Clusters in NGC 1569. *ApJ*, **466**, L83.

Hopman, C. and Alexander, T. (2006a). Resonant Relaxation near a Massive Black Hole: The Stellar Distribution and Gravitational Wave Sources. *ApJ*, **645**, 1152–1163.

Hopman, C. and Alexander, T. (2006b). The Effect of Mass Segregation on Gravitational Wave Sources near Massive Black Holes. *ApJ*, **645**, L133–L136.

Irons, W. T., Lacy, J. H., and Richter, M. J. (2012). Ionized Gas in the Galactic Center: New Observations and Interpretation. *ApJ*, **755**, 90.

Jackson, J. M., Geis, N., Genzel, R., Harris, A. I., Madden, S., Poglitsch, A., Stacey, G. J., and Townes, C. H. (1993). Neutral gas in the central 2 parsecs of the Galaxy. *ApJ*, **402**, 173–184.

Jalali, B., Pelupessy, F. I., Eckart, A., Portegies Zwart, S., Sabha, N., Borkar, A., Moultaka, J., Mužić, K., and Moser, L. (2014). Star formation in the vicinity of nuclear black holes: young stellar objects close to Sgr A*. *MNRAS*, **444**, 1205–1220.

Kennea, J. A., Krimm, H., Barthelmy, S., Gehrels, N., Markwardt, C., Cummings, J., Marshall, F., Sakamoto, T., Degenaar, N., Reynolds, M. T., Miller, J. M., and Kouveliotou, C. (2013). Swift/BAT detection of an SGR-like flare from near Sgr A*. *The Astronomer's Telegram*, **5009**, 1.

Kim, S. S., Figer, D. F., and Morris, M. (2004). Dynamical Friction on Galactic Center Star Clusters with an Intermediate-Mass Black Hole. *ApJ*, **607**, L123–L126.

Kocsis, B. and Tremaine, S. (2011). Resonant relaxation and the warp of the stellar disc in the Galactic Centre. *MNRAS*, **412**, 187–207.

Koyama, K., Maeda, Y., Sonobe, T., Takeshima, T., Tanaka, Y., and Yamauchi, S. (1996). ASCA View of Our Galactic Center: Remains of Past Activities in X-Rays? *PASJ*, **48**, 249–255.

Krabbe, A., Genzel, R., Eckart, A., Najarro, F., Lutz, D., Cameron, M., Kroker, H., Tacconi-Garman, L. E., Thatte, N., Weitzel, L., Drapatz, S., Geballe, T., Sternberg, A., and Kudritzki, R. (1995). The Nuclear Cluster of the Milky Way: Star Formation and Velocity Dispersion in the Central 0.5 Parsec. *ApJ*, **447**, L95+.

Lagage, P. O., Pel, J. W., Authier, M., Belorgey, J., Claret, A., Doucet, C., Dubreuil, D., Durand, G., Elswijk, E., Girardot, P., Käufl, H. U., Kroes, G., Lortholary, M., Lussignol, Y., Marchesi, M., Pantin, E., Peletier, R., Pirard, J.-F., Pragt, J., Rio, Y., Schoenmaker, T., Siebenmorgen, R., Silber, A., Smette, A., Sterzik, M., and Veyssiere, C. (2004). Successful Commissioning of VISIR: The Mid-Infrared VLT Instrument. *Msngr*, **117**, 12–16.

Lamers, H. J. G. L. M. and Cassinelli, J. P. (1999). *Introduction to Stellar Winds*.

Laor, A. (2003). On the Nature of Low-Luminosity Narrow-Line Active Galactic Nuclei. *ApJ*, **590**, 86–94.

LaRosa, T. N., Kassim, N. E., Lazio, T. J. W., and Hyman, S. D. (2000). A Wide-Field 90 Centimeter VLA Image of the Galactic Center Region. *AJ*, **119**, 207–240.

Lau, R. M., Herter, T. L., Morris, M. R., Becklin, E. E., and Adams, J. D. (2013). SOFIA/FORCAST Imaging of the Circumnuclear Ring at the Galactic Center. *ApJ*, **775**, 37.

Levin, Y., Wu, A., and Thommes, E. (2005). Intermediate-Mass Black Hole(s) and Stellar Orbits in the Galactic Center. *ApJ*, **635**, 341–348.

Li, J., Ostriker, J., and Sunyaev, R. (2013a). Rotating Accretion Flows: From Infinity to the Black Hole. *ApJ*, **767**, 105.

Li, Z., Morris, M. R., and Baganoff, F. K. (2013b). Evidence for a Parsec-scale Jet from the Galactic Center Black Hole: Interaction with Local Gas. *ApJ*, **779**, 154.

Lightman, A. P. and Shapiro, S. L. (1977). The distribution and consumption rate of stars around a massive, collapsed object. *ApJ*, **211**, 244–262.

Löckmann, U., Baumgardt, H., and Kroupa, P. (2009). Influence of a stellar cusp on the dynamics of young stellar discs and the origin of the S-stars in the Galactic Centre. *MNRAS*, **398**, 429–437.

Longmore, S. N., Rathborne, J., Bastian, N., Alves, J., Ascenso, J., Bally, J., Testi, L., Longmore, A., Battersby, C., Bressert, E., Purcell, C., Walsh, A., Jackson, J., Foster, J., Molinari, S., Meingast, S., Amorim, A., Lima, J., Marques, R., Moitinho, A., Pinhao, J., Rebordao, J., and Santos, F. D. (2012). G0.253 + 0.016: A Molecular Cloud Progenitor of an Arches-like Cluster. *ApJ*, **746**, 117.

Madigan, A.-M., Levin, Y., and Hopman, C. (2009). A New Secular Instability of Eccentric Stellar Disks around Supermassive Black Holes, with Application to the Galactic Center. *ApJ*, **697**, L44–L48.

Maeda, Y., Baganoff, F. K., Feigelson, E. D., Morris, M., Bautz, M. W., Brandt, W. N., Burrows, D. N., Doty, J. P, Garmire, G. P, Pravdo, S. H., Ricker, G. R., and Townsley, L. K. (2002). A Chandra Study of Sagittarius A East: A Supernova Remnant Regulating the Activity of Our Galactic Center? *ApJ*, **570**, 671–687.

Maíz Apellániz, J. and Úbeda, L. (2005). Numerical Biases on Initial Mass Function Determinations Created by Binning. *ApJ*, **629**, 873–880.

Markoff, S. (2010). Revelations in our own backyard: Chandra's unique Galactic Center discoveries. *Proceedings of the National Academy of Science*, **107**, 7196–7201.

Markoff, S., Falcke, H., Yuan, F., and Biermann, P. L. (2001). The Nature of the 10 kilosecond X-ray flare in Sgr A*. *A&A*, **379**, L13–L16.

Markoff, S., Bower, G. C., and Falcke, H. (2007). How to hide large-scale outflows: size constraints on the jets of Sgr A*. *MNRAS*, **379**, 1519–1532.

Martins, F., Genzel, R., Hillier, D. J., Eisenhauer, F., Paumard, T., Gillessen, S., Ott, T., and Trippe, S. (2007). Stellar and wind properties of massive stars in the central parsec of the Galaxy. *A&A*, **468**, 233–254.

Martins, F., Gillessen, S., Eisenhauer, F., Genzel, R., Ott, T., and Trippe, S. (2008). On the Nature of the Fast-Moving Star S2 in the Galactic Center. *ApJ*, **672**, L119–L122.

Merritt, D. (2010). The Distribution of Stars and Stellar Remnants at the Galactic Center. *ApJ*, **718**, 739–761.

Merritt, D. (2012). *Black Holes and the Dynamics of Galactic Nuclei*. Princeton University Press.

Merritt, D., Gualandris, A., and Mikkola, S. (2009). Explaining the Orbits of the Galactic Center S-Stars. *ApJ*, **693**, L35–L38.

Merritt, D., Alexander, T., Mikkola, S., and Will, C. M. (2010). Testing properties of the Galactic center black hole using stellar orbits. *Phys. Rev. D*, **81**(6), 062002.

Moneti, A., Stolovy, S., Blommaert, J. A. D. L., Figer, D. F., and Najarro, F. (2001). Mid-infrared imaging and spectroscopy of the enigmatic cocoon stars in the Quintuplet Cluster. *A&A*, **366**, 106–120.

Mori, K., Gotthelf, E. V., Zhang, S., An, H., Baganoff, F. K., Barrière, N. M., Beloborodov, A. M., Boggs, S. E., Christensen, F. E., Craig, W. W., Dufour, F., Grefenstette, B. W., Hailey, C. J., Harrison, F. A., Hong, J., Kaspi, V. M., Kennea, J. A., Madsen, K. K., Markwardt, C. B., Nynka, M., Stern, D., Tomsick, J. A., and Zhang, W. W. (2013). NuSTAR Discovery of a 3.76 s Transient Magnetar Near Sagittarius A*. *ApJ*, **770**, L23.

Morris, M. (1993). Massive star formation near the Galactic center and the fate of the stellar remnants. *ApJ*, **408**, 496–506.

Morris, M. and Serabyn, E. (1996). The Galactic Center Environment. *ARA&A*, **34**, 645–702.

Morris, M. R., Zhao, J.-H., and Goss, W. M. (2014). Nonthermal filamentary radio features within 20 pc of the Galactic center. In L. O. Sjouwerman, C. C. Lang, and J. Ott, editors, *IAU Symposium*, volume 303 of *IAU Symposium*, pages 369–373.

Mouawad, N., Eckart, A., Pfalzner, S., Schödel, R., Moultaka, J., and Spurzem, R. (2005). Weighing the cusp at the Galactic Centre. *Astronomische Nachrichten*, **326**, 83–95.

Moultaka, J., Eckart, A., Schödel, R., Viehmann, T., and Najarro, F. (2005). VLT L-band mapping of the Galactic center IRS 3-IRS 13 region. Evidence for new Wolf-Rayet type stars. *A&A*, **443**, 163–173.

Moultaka, J., Eckart, A., and Schödel, R. (2009). M-band Spectra of Dust-embedded Sources at the Galactic Center. *ApJ*, **703**, 1635–1647.

Muno, M. P., Baganoff, F. K., Brandt, W. N., Park, S., and Morris, M. R. (2007). Discovery of Variable Iron Fluorescence from Reflection Nebulae in the Galactic Center. *ApJ*, **656**, L69–L72.

Muno, M. P., Baganoff, F. K., Brandt, W. N., Morris, M. R., and Starck, J.-L. (2008). A Catalog of Diffuse X-Ray-emitting Features within 20 pc of Sagittarius A*: Twenty Pulsar Wind Nebulae? *ApJ*, **673**, 251–263.

Murphy, B. W., Cohn, H. N., and Durisen, R. H. (1991). Dynamical and luminosity evolution of active galactic nuclei - Models with a mass spectrum. *ApJ*, **370**, 60–77.

Mužić, K., Eckart, A., Schödel, R., Meyer, L., and Zensus, A. (2007). First proper motions of thin dust filaments at the Galactic center. *A&A*, **469**, 993–1002.

Mužić, K., Schödel, R., Eckart, A., Meyer, L., and Zensus, A. (2008). IRS 13N: a new comoving group of sources at the Galactic center. *A&A*, **482**, 173–178.

Mužić, K., Eckart, A., Schödel, R., Buchholz, R., Zamaninasab, M., and Witzel, G. (2010). Comet-shaped sources at the Galactic center. Evidence of a wind from the central 0.2 pc. *A&A*, **521**, A13.

Nagata, T., Woodward, C. E., Shure, M., and Kobayashi, N. (1995). Object 17: Another cluster of emission-line stars near the galactic center. *AJ*, **109**, 1676–1681.

Narayan, R. and McClintock, J. E. (2008). Advection-dominated accretion and the black hole event horizon. *NewAR*, **51**, 733–751.

Nayakshin, S. and Sunyaev, R. (2007). X-rays from cusps of compact remnants near galactic centres. *MNRAS*, **377**, 1647–1651.

Nicastro, F. (2000). Broad Emission Line Regions in Active Galactic Nuclei: The Link with the Accretion Power. *ApJ*, **530**, L65–L68.

Paumard, T., Genzel, R., Martins, F., Nayakshin, S., Beloborodov, A. M., Levin, Y., Trippe, S., Eisenhauer, F., Ott, T., Gillessen, S., Abuter, R., Cuadra, J., Alexander, T., and Sternberg, A. (2006). The Two Young Star Disks in the Central Parsec of the Galaxy: Properties, Dynamics, and Formation. *ApJ*, **643**, 1011–1035.

Perets, H. B. and Gualandris, A. (2010). Dynamical Constraints on the Origin of the Young B-stars in the Galactic Center. *ApJ*, **719**, 220–228.

Perets, H. B., Hopman, C., and Alexander, T. (2007). Massive Perturber-driven Interactions between Stars and a Massive Black Hole. *ApJ*, **656**, 709–720.

Perets, H. B., Gualandris, A., Kupi, G., Merritt, D., and Alexander, T. (2009). Dynamical Evolution of the Young Stars in the Galactic Center: N-body Simulations of the S-Stars. *ApJ*, **702**, 884–889.

Perger, M., Moultaka, J., Eckart, A., Viehmann, T., Schödel, R., and Muzic, K. (2008). Compact mid-IR sources east of Galactic Center source IRS5. *A&A*, **478**, 127–135.

Phifer, K., Do, T., Meyer, L., Ghez, A. M., Witzel, G., Yelda, S., Boehle, A., Lu, J. R., Morris, M. R., Becklin, E. E., and Matthews, K. (2013). Keck Observations of the Galactic Center Source G2: Gas Cloud or Star? *ApJ*, **773**, L13.

Ponti, G., Terrier, R., Goldwurm, A., Belanger, G., and Trap, G. (2010). Discovery of a Superluminal Fe K Echo at the Galactic Center: The Glorious Past of Sgr A* Preserved by Molecular Clouds. *ApJ*, **714**, 732–747.

Ponti, G., Morris, M. R., Terrier, R., and Goldwurm, A. (2013). Traces of Past Activity in the Galactic Centre. In D. F. Torres and O. Reimer, editors, *Cosmic Rays in Star-Forming Environments*, volume 34 of *Advances in Solid State Physics*, page 331.

Portegies Zwart, S. F., Baumgardt, H., McMillan, S. L. W., Makino, J., Hut, P., and Ebisuzaki, T. (2006). The Ecology of Star Clusters and Intermediate-Mass Black Holes in the Galactic Bulge. *ApJ*, **641**, 319–326.

Preto, M. and Amaro-Seoane, P. (2010). On Strong Mass Segregation Around a Massive Black Hole: Implications for Lower-Frequency Gravitational-Wave Astrophysics. *ApJ*, **708**, L42–L46.

Rauch, C., Mužić, K., Eckart, A., Buchholz, R. M., García-Marín, M., Sabha, N., Straubmeier, C., Valencia-S., M., and Yazici, S. (2013). A peek behind the dusty curtain: K_S-band polarization photometry and bow shock models of the Galactic center source IRS 8. *A&A*, **551**, A35.

Rauch, K. P. and Tremaine, S. (1996). Resonant relaxation in stellar systems. *New Ast.*, **1**, 149–170.

Rea, N., Esposito, P., Pons, J. A., Turolla, R., Torres, D. F., Israel, G. L., Possenti, A., Burgay, M., Viganò, D., Papitto, A., Perna, R., Stella, L., Ponti, G., Baganoff, F. K., Haggard, D., Camero-Arranz, A., Zane, S., Minter, A., Mereghetti, S., Tiengo, A., Schödel, R., Feroci, M., Mignani, R., and Götz, D. (2013). A Strongly Magnetized Pulsar within the Grasp of the Milky Way's Supermassive Black Hole. *ApJ*, **775**, L34.

Reimers, D. (1975). Circumstellar absorption lines and mass loss from red giants. *Memoires of the Societe Royale des Sciences de Liege*, **8**, 369–382.

Revnivtsev, M. G., Churazov, E. M., Sazonov, S. Y., Sunyaev, R. A., Lutovinov, A. A., Gilfanov, M. R., Vikhlinin, A. A., Shtykovsky, P. E., and Pavlinsky, M. N. (2004). Hard X-ray view of the past activity of Sgr A* in a natural Compton mirror. *A&A*, **425**, L49–L52.

Rieke, G. H. and Lebofsky, M. J. (1985). The interstellar extinction law from 1 to 13 microns. *ApJ*, **288**, 618–621.

Rieke, G. H., Rieke, M. J., and Paul, A. E. (1989). Origin of the excitation of the galactic center. *ApJ*, **336**, 752–761.

Riffel, R. A., Storchi-Bergmann, T., and Riffel, R. (2014). An Outflow Perpendicular to the Radio Jet in the Seyfert Nucleus of NGC 5929. *ApJ*, **780**, L24.

Rubilar, G. F. and Eckart, A. (2001). Periastron shifts of stellar orbits near the Galactic Center. *A&A*, **374**, 95–104.

Sabha, N., Witzel, G., Eckart, A., Buchholz, R. M., Bremer, M., Gießübel, R., García-Marín, M., Kunneriath, D., Muzic, K., Schödel, R., Straubmeier, C., Zamaninasab, M., and Zernickel, A. (2010). The extreme luminosity states of Sagittarius A*. *A&A*, **512**, A2.

Sabha, N., Witzel, G., Eckart, A., Zamaninasab, M., Schödel, R., Zernickel, A., García-Marín, M., Kunneriath, D., Moultaka, J., Mužić, K., and Straubmeier, C. (2011). The Low Luminosity State of Sagittarius A*. In M. R. Morris, Q. D. Wang, & F. Yuan, editor, *Astronomical Society of the Pacific Conference Series*, volume 439 of *Astronomical Society of the Pacific Conference Series*, page 313.

Sabha, N., Eckart, A., Merritt, D., Zamaninasab, M., Witzel, G., García-Marín, M., Jalali, B., Valencia-S., M., Yazici, S., Buchholz, R., Shahzamanian, B., Rauch, C., Horrobin, M., and Straubmeier, C. (2012). The S-star cluster at the center of the Milky Way. On the nature of diffuse NIR emission in the inner tenth of a parsec. *A&A*, **545**, A70.

Sabha, N., Zamaninasab, M., Eckart, A., and Moser, L. (2014). A new MIR bow shock source in the Galactic center. In L. O. Sjouwerman, C. C. Lang, and J. Ott, editors, *IAU Symposium*, volume 303 of *IAU Symposium*, pages 150–152.

Sabha, N., Eckart, A., Merritt, D., and Zamaninasab, M. (2015). Nature of the Diffuse Near-Infrared Emission in the Innermost Arcsecond of the Galactic Center. In K. Rosquist, editor, *Thirteenth Marcel Grossmann Meeting: On Recent Developments in Theoretical and Experimental General Relativity, Astrophysics and Relativistic Field Theories*, pages 1715–1717.

Salaris, M. and Cassisi, S. (2005). *Evolution of Stars and Stellar Populations*.

Sanchez-Bermudez, J., Schödel, R., Alberdi, A., Muzić, K., Hummel, C. A., and Pott, J.-U. (2014). Properties of bow-shock sources at the Galactic center. *A&A*, **567**, A21.

Sazonov, S., Sunyaev, R., and Revnivtsev, M. (2011). Coronal radiation of a cusp of spun-up stars and the X-ray luminosity of Sgr A*. *MNRAS*, page 1987.

Schödel, R., Ott, T., Genzel, R., Hofmann, R., Lehnert, M., Eckart, A., Mouawad, N., Alexander, T., Reid, M. J., Lenzen, R., Hartung, M., Lacombe, F., Rouan, D., Gendron, E., Rousset, G., Lagrange, A., Brandner, W., Ageorges, N., Lidman, C., Moorwood, A. F. M., Spyromilio, J., Hubin, N., and Menten, K. M. (2002). A star in a 15.2-year orbit around the supermassive black hole at the centre of the Milky Way. *Nature*, **419**, 694–696.

Schödel, R., Eckart, A., Alexander, T., Merritt, D., Genzel, R., Sternberg, A., Meyer, L., Kul, F., Moultaka, J., Ott, T., and Straubmeier, C. (2007). The structure of the nuclear stellar cluster of the Milky Way. *A&A*, **469**, 125–146.

Schödel, R., Merritt, D., and Eckart, A. (2009). The nuclear star cluster of the Milky Way: proper motions and mass. *A&A*, **502**, 91–111.

Schödel, R., Najarro, F., Muzic, K., and Eckart, A. (2010). Peering through the veil: near-infrared photometry and extinction for the Galactic nuclear star cluster. Accurate near infrared H, Ks, and L' photometry and the near-infrared extinction-law toward the central parsec of the Galaxy. *A&A*, **511**, A18.

Serabyn, E. and Morris, M. (1996). Sustained star formation in the central stellar cluster of the Milky Way. *Nature*, **382**, 602–604.

Serabyn, E., Shupe, D., and Figer, D. F. (1998). An extraordinary cluster of massive stars near the centre of the Milky Way. *Nature*, **394**, 448–451.

Shcherbakov, R. V. and Baganoff, F. K. (2010). Inflow-Outflow Model with Conduction and Self-consistent Feeding for Sgr A*. *ApJ*, **716**, 504–509.

Silk, J., Antonuccio-Delogu, V., Dubois, Y., Gaibler, V., Haas, M. R., Khochfar, S., and Krause, M. (2012). Jet interactions with a giant molecular cloud in the Galactic centre and ejection of hypervelocity stars. *A&A*, **545**, L11.

Simpson, J. P., Colgan, S. W. J., Cotera, A. S., Erickson, E. F., Hollenbach, D. J., Kaufman, M. J., and Rubin, R. H. (2007). Spitzer IRS Observations of the Galactic Center: Shocked Gas in the Radio Arc Bubble. *ApJ*, **670**, 1115–1131.

Sohn, S. T., Anderson, J., and van der Marel, R. P. (2012). The M31 Velocity Vector. I. Hubble Space Telescope Proper-motion Measurements. *ApJ*, **753**, 7.

Stolte, A., Grebel, E. K., Brandner, W., and Figer, D. F. (2002). The mass function of the Arches cluster from Gemini adaptive optics data. *A&A*, **394**, 459–478.

Stolte, A., Ghez, A. M., Morris, M., Lu, J. R., Brandner, W., and Matthews, K. (2008). The Proper Motion of the Arches Cluster with Keck Laser-Guide Star Adaptive Optics. *ApJ*, **675**, 1278–1292.

Stolte, A., Morris, M. R., Ghez, A. M., Do, T., Lu, J. R., Wright, S. A., Ballard, C., Mills, E., and Matthews, K. (2010). Disks in the Arches Cluster—Survival in a Starburst Environment. *ApJ*, **718**, 810–831.

Su, M. and Finkbeiner, D. P. (2012). Evidence for Gamma-Ray Jets in the Milky Way. *ApJ*, **753**, 61.

Su, M., Slatyer, T. R., and Finkbeiner, D. P. (2010). Giant Gamma-ray Bubbles from Fermi-LAT: Active Galactic Nucleus Activity or Bipolar Galactic Wind? *ApJ*, **724**, 1044–1082.

Sunyaev, R. A., Markevitch, M., and Pavlinsky, M. (1993). The center of the Galaxy in the recent past - A view from GRANAT. *ApJ*, **407**, 606–610.

Suzuki, T. K. (2007). Structured Red Giant Winds with Magnetized Hot Bubbles and the Corona/Cool Wind Dividing Line. *ApJ*, **659**, 1592–1610.

Tanner, A., Ghez, A. M., Morris, M., Becklin, E. E., Cotera, A., Ressler, M., Werner, M., and Wizinowich, P. (2002). Spatially Resolved Observations of the Galactic Center Source IRS 21. *ApJ*, **575**, 860–870.

Tanner, A., Ghez, A. M., Morris, M. R., and Christou, J. C. (2005). Stellar Bow Shocks in the Northern Arm of the Galactic Center: More Members and Kinematics of the Massive Star Population. *ApJ*, **624**, 742–750.

Tanner, A., Figer, D. F., Najarro, F., Kudritzki, R. P., Gilmore, D., Morris, M., Becklin, E. E., McLean, I. S., Gilbert, A. M., Graham, J. R., Larkin, J. E., Levenson, N. A., and Teplitz, H. I. (2006). High Spectral Resolution Observations of the Massive Stars in the Galactic Center. *ApJ*, **641**, 891–904.

Timmes, F. X., Woosley, S. E., and Weaver, T. A. (1996). The Neutron Star and Black Hole Initial Mass Function. *ApJ*, **457**, 834–+.

Tully, R. B., Courtois, H., Hoffman, Y., and Pomarède, D. (2014). The Laniakea supercluster of galaxies. *Nature*, **513**, 71–73.

van der Marel, R. P., Fardal, M., Besla, G., Beaton, R. L., Sohn, S. T., Anderson, J., Brown, T., and Guhathakurta, P. (2012a). The M31 Velocity Vector. II. Radial Orbit toward the Milky Way and Implied Local Group Mass. *ApJ*, **753**, 8.

van der Marel, R. P., Besla, G., Cox, T. J., Sohn, S. T., and Anderson, J. (2012b). The M31 Velocity Vector. III. Future Milky Way M31-M33 Orbital Evolution, Merging, and Fate of the Sun. *ApJ*, **753**, 9.

Viehmann, T., Eckart, A., Schödel, R., Moultaka, J., Straubmeier, C., and Pott, J.-U. (2005). L- and M-band imaging observations of the Galactic Center region. *A&A*, **433**, 117–125.

Viehmann, T., Eckart, A., Schödel, R., Pott, J.-U., and Moultaka, J. (2006). Dusty Sources at the Galactic Center the N- and Q-Band Views with VISIR. *ApJ*, **642**, 861–867.

Wang, Q. D., Dong, H., Cotera, A., Stolovy, S., Morris, M., Lang, C. C., Muno, M. P., Schneider, G., and Calzetti, D. (2010). HST/NICMOS Paschen-α Survey of the Galactic Centre: Overview. *MNRAS*, **402**, 895–902.

Wang, Q. D., Nowak, M. A., Markoff, S. B., Baganoff, F. K., Nayakshin, S., Yuan, F., Cuadra, J., Davis, J., Dexter, J., Fabian, A. C., Grosso, N., Haggard, D., Houck, J., Ji, L., Li, Z., Neilsen, J., Porquet, D., Ripple, F., and Shcherbakov, R. V. (2013). Dissecting X-ray–Emitting Gas Around the Center of Our Galaxy. *Science*, **341**, 981–983.

Weidner, C. and Vink, J. S. (2010). The masses, and the mass discrepancy of O-type stars. *A&A*, **524**, A98.

Wilkin, F. P. (1996). Exact Analytic Solutions for Stellar Wind Bow Shocks. *ApJ*, **459**, L31.

Witzel, G., Eckart, A., Bremer, M., Zamaninasab, M., Shahzamanian, B., Valencia-S., M., Schödel, R., Karas, V., Lenzen, R., Marchili, N., Sabha, N., Garcia-Marin, M., Buchholz, R. M., Kunneriath, D., and Straubmeier, C. (2012). Source-intrinsic Near-infrared Properties of Sgr A*: Total Intensity Measurements. *ApJS*, **203**, 18.

Wright, M. C. H., Coil, A. L., McGary, R. S., Ho, P. T. P., and Harris, A. I. (2001). Molecular Tracers of the Central 12 Parsecs of the Galactic Center. *ApJ*, **551**, 254–268.

Xu, Y. and Cao, X.-W. (2007). Evidence of the Link between Broad Emission Line Regions and Accretion Disks in Active Galactic Nuclei. *Chinese J. Astron. Astrophys.*, **7**, 63–70.

Yuan, F. (2011). Accretion and Ejection in Sgr A*. In M. R. Morris, Q. D. Wang, and F. Yuan, editors, *The Galactic Center: a Window to the Nuclear Environment of Disk Galaxies*, volume 439 of *Astronomical Society of the Pacific Conference Series*, page 346.

Yusef-Zadeh, F. and Morris, M. (1987). Structural details of the Sagittarius A complex - Evidence for a large-scale poloidal magnetic field in the Galactic center region. *ApJ*, **320**, 545–561.

Yusef-Zadeh, F., Roberts, D. A., and Biretta, J. (1998). Proper Motions of Ionized Gas at the Galactic Center: Evidence for Unbound Orbiting Gas. *ApJ*, **499**, L159+.

Yusef-Zadeh, F., Hewitt, J. W., Arendt, R. G., Whitney, B., Rieke, G., Wardle, M., Hinz, J. L., Stolovy, S., Lang, C. C., Burton, M. G., and Ramirez, S. (2009). Star Formation in the Central 400 pc of the Milky Way: Evidence for a Population of Massive Young Stellar Objects. *ApJ*, **702**, 178–225.

Yusef-Zadeh, F., Arendt, R., Bushouse, H., Cotton, W., Haggard, D., Pound, M. W., Roberts, D. A., Royster, M., and Wardle, M. (2012a). A 3 pc Scale Jet-driven Outflow from Sgr A*. *ApJ*, **758**, L11.

Yusef-Zadeh, F., Bushouse, H., and Wardle, M. (2012b). Hubble Space Telescope Observations of the Stellar Distribution near Sgr A*. *ApJ*, **744**, 24.

Zamaninasab, M., Eckart, A., Dovčiak, M., Karas, V., Schödel, R., Witzel, G., Sabha, N., García-Marín, M., Kunneriath, D., Mužić, K., Straubmeier, C., Valencia-S, M., and Zensus, J. A. (2011). Near-infrared polarimetry as a tool for testing properties of accreting supermassive black holes. *MNRAS*, **413**, 322–332.

Zamaninasab, M., Clausen-Brown, E., Savolainen, T., and Tchekhovskoy, A. (2014). Dynamically important magnetic fields near accreting supermassive black holes. *Nature*, **510**, 126–128.

Zhao, J.-H., Morris, M. R., Goss, W. M., and An, T. (2009). Dynamics of Ionized Gas at the Galactic Center: Very Large Array Observations of the Three-dimensional Velocity Field and Location of the Ionized Streams in Sagittarius A West. *ApJ*, **699**, 186–214.

Zucker, S., Alexander, T., Gillessen, S., Eisenhauer, F., and Genzel, R. (2006). Probing Post-Newtonian Physics near the Galactic Black Hole with Stellar Redshift Measurements. *ApJ*, **639**, L21–L24.

Zylka, R., Mezger, P. G., Ward-Thompson, D., Duschl, W. J., and Lesch, H. (1995). Anatomy of the Sagittarius A complex. 4: SGR A* and the Central Cavity revisited. *A&A*, **297**, 83–97.

LIST OF FIGURES

LIST OF TABLES

LIST OF ACRONYMS

A_K	Extinction in K-band
AGB	Asymptotic Giant Branch
AGN	Active Galactic Nucleus
AO	Adaptive Optics
BH	Black Hole
CND	Circumnuclear Disk
CONICA	High Resolution IR Camera and Spectrometer
ESA	European Space Agency
ESO	European Southern Observatory
ESO CPL	ESO - Common Pipeline Library
FOV	Field of View
FWHM	Full Width at Half Maximum
FIR	Far Infrared
GC	Galactic Center
GTO	Guaranteed Time Observation
HST	Hubble Space Telescope
IF	Integral Field
IFU	Integral Field Unit
IMF	Initial Mass Function
IMBH	Intermidiate Mass Black Hole
IR	InfraRed
IRAS	The Infrared Astronomical Satellite
ISM	Inter Stellar Medium
JPL	Jet Propulsion Laboratory
JWST	The James Webb Space Telescope
KLF	K-band Luminosity Function
kpc	kilo parsecs
LLAGN	Low Luminosity AGN
mas	milli arcsecond
MIR	Mid-Infrared
MIRI	The Mid-Infrared Instrument
mpc	mega parsecs

MW	Milky Way
NaCo	Nasmyth Adaptive Optics System (NAOS) Near-Infrared Imager and Spectrograph (CONICA)
NASA	National Aeronautics and Space Administration
NIR	Near-Infrared
NS10	New Star 10
NSC	Nuclear Star Cluster
ONC	Orion Nebula Cluster
PA	Polarization Angle
PAH	Polycyclic Aromatic Hydrocarbon
pc	parsec
PSF	Point Spread Function
RC/HB	Red Clump / Horizontal Branch
RIAF	Radiatively Inefficient Accretion Flow
RR	Resonant Relaxation
S/N	Signal to Noise ratio
SED	Spectral Energy Distribution
Sgr A*	Sagittarius A*
SMBH	Supermassive Black Hole
SPH	Smooth Particle Hydrodynamics
VISIR	VLT Imager and Spectrometer for mid-Infrared
VLA	Very Large Array
VLT	Very Large Telescope
VLTI	Very Large Telescope Interferometer
YSO	Young Stellar Object
WR	Wolf-Rayet
ZAMS	Zero-Age Main Sequence star

ACKNOWLEDGEMENTS

I conclude this dissertation by expressing my gratitude to all the people who helped me during the past years, both in and outside of science, and without whom my study and work would have been much more difficult and less enjoyable.

To my supervisor, Prof. Andreas Eckart: Thank you for all the support and advice, and for keeping your door open to any discussions and questions I have, no matter how trivial they may seem. Thanks to my PhD thesis committee members: Prof. Andreas Eckart, Prof. Peter Schneider, Prof. Yaping Shao, Dr. Macarena Garcia-Marin and Dr. Christian Straubmeier.

I am grateful to Prof. David Merritt for performing the N-body simulation addressed in Chapter 2 and for the help in writing/interpreting the results. To Rainer Schöedel for the help with the MIR pattern removal, and for showing interest in my work! To Jihane Moultaka for sending me on my first observing trip to Paranal. To Koraljka Muzic, for answering my emails promptly whenever I needed help in data reduction. Thanks to all the ESO staff who have helped me during my three trips to Paranal, and also for the time when I had to observe remotely via Skype. To the PH1 secretaries: Thanks for the occasional chats and for making all the bureaucratic issues much easier. To Dr. Petra Neubauer-Guenther: for the nice chats and all the help regarding BCGS matters. This work was partially supported by the Bonn Cologne Graduate School (BCGS) for Physics and Astronomy, the German Deutsche Forschungsgemeinschaft, DFG, via grant SFB 956, and the International Max Planck Research School (IMPRS) for Astronomy and Astrophysics at the MPIfR and the Universities of Bonn and Cologne.

A big thanks goes to all who have read and commented on my dissertation, either as a whole or only some parts of it: Mohammad Zamaninasab, Eric Clausen-Brown, Senol Yazici, Behrang Jalali, Lydia Moser, Devaky Kunneriath, Mariangela Vitale, Macarena Garcia-Marin and Banafsheh Shahzamanian. A dedicated thank you to Senol, Lydia and Semir Smajic for writing the German abstract on such a short notice.

To *ae*group: Thank you for the wonderful working atmosphere, for the friendly chats over lunch or in the corridors, for all the birthday/submission/no-occasion cakes, for the random outings, for the technical support and the occasional German translations.

ERKLÄRUNG

Ich versichere, daß ich die von mir vorgelegte Dissertation selbständig angefertigt, die benutzten Quellen und Hilfsmittel vollständig angegeben und die Stellen der Arbeit – einschließlich Tabellen, Karten und Abbildungen –, die anderen Werken im Wortlaut oder dem Sinn nach entnommen sind, in jedem Einzelfall als Entlehnung kenntlich gemacht habe; daß diese Dissertation noch keiner anderen Fakultät oder Universität zur Prüfung vorgelegen hat; daß sie – abgesehen von unten angegebenen Teilpublikationen – noch nicht veröffentlicht worden ist sowie, daß ich eine solche Veröffentlichung vor Abschluß des Promotionsverfahrens nicht vornehmen werde. Die Bestimmungen dieser Promotionsordnung sind mir bekannt. Die von mir vorgelegte Dissertation ist von Prof. Dr. Andreas Eckart betreut worden.

Köln, 19.10.2014

Teilpublikationen

Sabha, N., Eckart, A., Merritt, D., Zamaninasab, M., Witzel, G., García-Marín, M., Jalali, B., Valencia-S., M., Yazici, S., Buchholz, R., Shahzamanian, B., Rauch, C., Horrobin, M., and Straubmeier, C. (2012). The S-star cluster at the center of the Milky Way. On the nature of diffuse NIR emission in the inner tenth of a parsec. *A&A*, **545**, A70.

Sabha, N., Witzel, G., Eckart, A., Buchholz, R. M., Bremer, M., Gießübel, R., García-Marín, M., Kunneriath, D., Muzic, K., Schödel, R., Straubmeier, C., Zamaninasab, M., and Zernickel, A. (2010). The extreme luminosity states of Sagittarius A*. *A&A*, **512**, A2.

Sabha, N., Eckart, A., Merritt, D., and Zamaninasab, M. (2015). Nature of the Diffuse Near-Infrared Emission in the Innermost Arcsecond of the Galactic Center. In K. Rosquist, editor, *Thirteenth Marcel Grossmann Meeting: On Recent Developments in Theoretical and Experimental General Relativity, Astrophysics and Relativistic Field Theories*, pages 1715–1717.

Sabha, N., Zamaninasab, M., Eckart, A., and Moser, L. (2014). A new MIR bow shock source in the Galactic center. In L. O. Sjouwerman, C. C. Lang, and J. Ott, editors, *IAU Symposium*, volume 303 of *IAU Symposium*, pages 150–152.

Sabha, N., Witzel, G., Eckart, A., Zamaninasab, M., Schödel, R., Zernickel, A., García-Marín, M., Kunneriath, D., Moultaka, J., Mužić, K., and Straubmeier, C. (2011). The Low Luminosity State of Sagittarius A*. In M. R. Morris, Q. D. Wang, & F. Yuan, editor, *Astronomical Society of the Pacific Conference Series*, volume 439 of *Astronomical Society of the Pacific Conference Series*, page 313.

Eckart, A., Sabha, N., Witzel, G., Straubmeier, C., Shahzamanian, B., Valencia-S., M., García-Marín, M., Horrobin, M., Moser, L., Zuther, J., Fischer, S., Rauch, C., Rost, S., Iserlohe, C., Yazici, S., Smajic, S., Wiest, M., Araujo-Hauck, C., and Wank, I. (2012). Beating the confusion limit: the necessity of high angular resolution for probing the physics of Sagittarius A* and its environment: opportunities for LINC-NIRVANA (LBT), GRAVITY (VLTI) and and METIS (E-ELT). In *Society of Photo-Optical Instrumentation Engineers (SPIE) Conference Series*, volume 8445 of *Society of Photo-Optical Instrumentation Engineers (SPIE) Conference Series*.

Rauch, C., Mužić, K., Eckart, A., Buchholz, R. M., García-Marín, M., Sabha, N., Straubmeier, C., Valencia-S., M., and Yazici, S. (2013). A peek behind the dusty curtain: K_S-band polarization photometry and bow shock models of the Galactic center source IRS 8. *A&A*, **551**, A35.

Weitere Publikationen

Eckart, A., Zamaninasab, M., Straubmeier, C., Fischer, S., Araujo-Hauck, C., Garcia-Marin, M., Wiest, M., Witzel, G., Buchholz, R. M., Sabha, N., Muzic, K., Eisenhauer, F., Paumard, T., Yazici, S., Perrin, G., Brandner, W., Perraut, K., Amorim, A., and Schöller, M. (2010). Signatures of strong gravity with GRAVITY. In *Society of Photo-Optical Instrumentation Engineers (SPIE) Conference Series*, volume 7734 of *Society of Photo-Optical Instrumentation Engineers (SPIE) Conference Series*.

Eckart, A., Zamaninasab, M., Sabha, N., García-Marín, M., Kunneriath, D., Straubmeier, C., Muzic, K., Witzel, G., Bremer, M., Valencia-Schneider, M., Karas, V., Dovciak, M., Morris, M. R., Baganoff, F., Schödel, R., Moultaka, J., Buchholz, R. M., Duschl, W., and Zensus, A. (2011). Coordinated Multi-Wavelength Observations of Variable Emission from the Galactic Center. In M. R. Morris, Q. D. Wang, and F. Yuan, editors, *The Galactic Center: a Window to the Nuclear Environment of Disk Galaxies*, volume 439 of *Astronomical Society of the Pacific Conference Series*, page 294.

Eckart, A., García-Marín, M., Vogel, S. N., Teuben, P., Morris, M. R., Baganoff, F., Dexter, J., Schödel, R., Witzel, G., Valencia-S, M., Karas, V., Kunneriath, D., Bremer, M., Straubmeier, C., Moser, L., Sabha, N., Buchholz, R., Zamaninasab, M., Mužić, K., Moultaka, J., and Zensus, J. A. (2012c). Flare emission from Sagittarius A*. *Journal of Physics Conference Series*, **372**(1), 012022.

Eckart, A., García-Marín, M., Vogel, S. N., Teuben, P., Morris, M. R., Baganoff, F., Dexter, J., Schödel, R., Witzel, G., Valencia-S., M., Karas, V., Kunneriath, D., Straubmeier, C., Moser, L., Sabha, N., Buchholz, R., Zamaninasab, M., Mužić, K., Moultaka, J., and Zensus, J. A. (2012d). Millimeter to X-ray flares from Sagittarius A*. *A&A*, **537**, A52.

Eckart, A., Britzen, S., Horrobin, M., Zamaninasab, M., Muzic, K., Sabha, N., Shahzamanian, B., Yazici, S., Moser, L., Zuther, J., Garcia-Marin, M., Valencia-S., M., Bursa, M., Karssen, G., Karas, V., Jalali, B., Vitale, M., Bremer, M., Fischer, S., Smajic, S., Rauch, C., Kunneriath, D., Moultaka, J., Straubmeier, C., Rashed, Y. E., Iserlohe, C., Busch, G., Markakis, K., Borkar, A., and Zensus, A. J. (2012e). The Galactic Center as a pradigm for low-luminosity nuclei? What can be learned from SgrA* for the central engine and conditions of star formation in nuclei of Seyfert galaxies and low luminosity nearby QSOs; The K-band identification of the DSO/G2 source from VLT and Keck data. In *Proceedings of Nuclei of Seyfert galaxies and QSOs - Central engine & conditions of star formation (Seyfert 2012). 6-8 November, 2012. Max-Planck-Insitut für Radioastronomie (MPIfR), Bonn, Germany. Online at <A href="http://pos.sissa.it/cgi-bin/reader/conf.cgi?confid=169"> http://pos.sissa.it/cgi-bin/reader/conf.cgi?confid=169</A>, id.4.*

Eckart, A., Mužić, K., Yazici, S., Sabha, N., Shahzamanian, B., Witzel, G., Moser, L., Garcia-Marin, M., Valencia-S., M., Jalali, B., Bremer, M., Straubmeier, C., Rauch, C., Buchholz, R., Kunneriath, D., and Moultaka, J. (2013). Near-infrared proper motions and spectroscopy of infrared excess sources at the Galactic center. *A&A*, **551**, A18.

Eckart, A., Mužić, K., Yazici, S., Sabha, N., Shahzamanian, B., Witzel, G., Moser, L., Garcia-Marin, M., Valencia-S., M., Jalali, B., Bremer, M., Straubmeier, C., Rauch, C., Buchholz, R., Kunneriath, D., and Moultaka, J. (2013c). The broad band spectral properties of SgrA* . The fate of the dusty object approaching the center. *Mem. Soc. Astron. Italiana*, **84**, 618.

Eckart, A., Horrobin, M., Britzen, S., Zamaninasab, M., Mužić, K., Sabha, N., Shahzamanian, B., Yazici, S., Moser, L., García-Marin, M., Valencia-S., M., Borkar, A., Bursa, M., Karssen, G., Karas, V., Zajaček, M., Bronfman, L., Finger, R., Jalali, B., Vitale, M., Rauch, C., Kunneriath, D., Moultaka, J., Straubmeier, C., Rashed, Y. E., Markakis, K., and Zensus, A. (2014). The infrared K-band identification of the DSO/G2 source from VLT and Keck data. In L. O. Sjouwerman, C. C. Lang, and J. Ott, editors, *IAU Symposium*, volume 303 of *IAU Symposium*, pages 269–273.

García-Marín, M., Eckart, A., Weiss, A., Witzel, G., Bremer, M., Zamaninasab, M., Morris, M. R., Schödel, R., Kunneriath, D., Nishiyama, S., Baganoff, F., Dovčiak, M., Sabha, N., Duschl, W. J., Moultaka, J., Karas, V., Najarro, F., Mužić, K., Straubmeier, C., Vogel, S. N., Krips, M., and Wiesemeyer, H. (2011a). Extended Submillimeter Emission of the Galactic Center and Near-infrared/submillimeter Variability of Its Supermassive Black Hole. *ApJ*, **738**, 158.

García-Marín, M., Eckart, A., Weiss, A., Witzel, G., Bremer, M., Zamaninasab, M., Schödel, R., Kunneriath, D., Sabha, N., Baganoff, F., Dovvciak, M., Duschl, W. J., Moultaka, J., Karas, V., Najarro, F., Mužić, K., Straubmeier, C., Vogel, S. N., Krips, M., and Wiesemeyer, H. (2011b). Sub-Millimeter View of the Galactic Center. In M. R. Morris, Q. D. Wang, and F. Yuan, editors, *The Galactic Center: a Window to the Nuclear Environment of Disk Galaxies*, volume 439 of *Astronomical Society of the Pacific Conference Series*, page 315.

Jalali, B., Pelupessy, F. I., Eckart, A., Portegies Zwart, S., Sabha, N., Borkar, A., Moultaka, J., Mužić, K., and Moser, L. (2014). Star formation in the vicinity of nuclear black holes: young stellar objects close to Sgr A*. *MNRAS*, **444**, 1205–1220.

Jalali, B., Pelupessy, F. I., Eckart, A., Portegies Zwart, S., Sabha, N., Borkar, A., Moultaka, J., Mužić, K., and Moser, L. (2014c). Young stellar objects close to Sgr A*. In L. O. Sjouwerman, C. C. Lang, and J. Ott, editors, *IAU Symposium*, volume 303 of *IAU Symposium*, pages 144–146.

Kunneriath, D., Witzel, G., Eckart, A., Zamaninasab, M., Gießübel, R., Schödel, R., Baganoff, F. K., Morris, M. R., Dovčiak, M., Duschl, W. J., García-Marín, M., Karas, V., König, S., Krichbaum, T. P., Krips, M., Lu, R.-S., Mauerhan, J., Moultaka, J., Mužić, K., Sabha, N., Najarro, F., Pott, J.-U., Schuster, K. F., Sjouwerman, L. O., Straubmeier, C., Thum, C., Vogel, S. N., Teuben, P., Weiss, A., Wiesemeyer, H., and Zensus, J. A. (2010). Coordinated NIR/mm observations of flare emission from Sagittarius A*. *A&A*, **517**, A46.

Kunneriath, D., Eckart, A., Zamaninasab, M., Witzel, G., Valencia-S, M., Sabha, N., and García-Marín, M. (2011a). Flare emission from Sagittarius A*. *Mem. Soc. Astron. Italiana*, **82**, 91.

Kunneriath, D., Eckart, A., Zamaninasab, M., Witzel, G., Schödel, R., García-Marín, M., König, S., Krichbaum, T. P., Lu, R., Moultaka, J., Mužić, K., Sabha, N., Sjouwerman, L. O., Straubmeier, C., Vogel, S. N., Teuben, P., and Zensus, J. A. (2011b). The Galactic Centre in the Millimeter Regime: Observations with CARMA. In M. R. Morris, Q. D. Wang, and F. Yuan, editors, *The Galactic Center: a Window to the Nuclear Environment of Disk Galaxies*, volume 439 of *Astronomical Society of the Pacific Conference Series*, page 327.

Moser, L., Eckart, A., Borkar, A., García-Marin, M., Kunneriath, D., Jalali, B., Sabha, N., Shahzamanian, B., Valencia-S., M., Zamaninasab, M., Bronfman, L., and Finger, R. (2014). Sgr A West in the light of molecules: cold and dense gas east of the circumnuclear disk. In L. O. Sjouwerman, C. C. Lang, and J. Ott, editors, *IAU Symposium*, volume 303 of *IAU Symposium*, pages 86–88.

Moultaka, J., Eckart, A., and Sabha, N. (2012). L- and M-band views of the central parsec. In *Proceedings of Nuclei of Seyfert galaxies and QSOs - Central engine & conditions of star formation (Seyfert 2012). 6-8 November, 2012. Max-Planck-Insitut für Radioastronomie (MPIfR), Bonn, Germany. Online at <A href="http://pos.sissa.it/cgi-bin/reader/conf.cgi?confid=169"> http://pos.sissa.it/cgi-bin/reader/conf.cgi?confid=169</A>, id.70.*

Moultaka, J., Eckart, A., Mužić, K., and Sabha, N. (2014). A 3-D mid-infrared view of the central parsec. In L. O. Sjouwerman, C. C. Lang, and J. Ott, editors, *IAU Symposium*, volume 303 of *IAU Symposium*, pages 199–201.

Shahzamanian, B., Eckart, A., Witzel, G., Sabha, N., and Zamaninasab, M. (2012). Polarized NIR observations of Sagittarius A*. In *Proceedings of Nuclei of Seyfert galaxies and QSOs - Central engine & conditions of star formation (Seyfert 2012). 6-8 November, 2012. Max-Planck-Insitut für Radioastronomie (MPIfR), Bonn, Germany. Online at <A href="http://pos.sissa.it/cgi-bin/reader/conf.cgi?confid=169"> http://pos.sissa.it/cgi-bin/reader/conf.cgi?confid=169</A>, id.74.*

Shahzamanian, B., Eckart, A., Zamaninasab, M., Witzel, G., and Sabha, N. (2014). Observations of NIR polarized light from Sagittarius A*. In L. O. Sjouwerman, C. C. Lang, and J. Ott, editors, *IAU Symposium*, volume 303 of *IAU Symposium*, pages 283–287.

Witzel, G., Eckart, A., Buchholz, R. M., Zamaninasab, M., Lenzen, R., Schödel, R., Araujo, C., Sabha, N., Bremer, M., Karas, V., Straubmeier, C., and Muzic, K. (2011). The instrumental polarization of the Nasmyth focus polarimetric differential imager NAOS/CONICA (NACO) at the VLT. Implications for time-resolved polarimetric measurements of Sagittarius A*. *A&A*, **525**, A130.

Witzel, G., Eckart, A., Bremer, M., Zamaninasab, M., Shahzamanian, B., Valencia-S., M., Schödel, R., Karas, V., Lenzen, R., Marchili, N., Sabha, N., Garcia-Marin, M., Buchholz, R. M., Kunneriath, D., and Straubmeier, C. (2012). Source-intrinsic Near-infrared Properties of Sgr A*: Total Intensity Measurements. *ApJS*, **203**, 18.

Zamaninasab, M., Eckart, A., Witzel, G., Dovciak, M., Karas, V., Schödel, R., Gießübel, R., Bremer, M., García-Marín, M., Kunneriath, D., Mužić, K., Nishiyama, S., Sabha, N., Straubmeier, C., and Zensus, A. (2010). Near infrared flares of Sagittarius A*. Importance of near infrared polarimetry. *A&A*, **510**, A3.

Zamaninasab, M., Eckart, A., Dovčiak, M., Karas, V., Schödel, R., Witzel, G., Sabha, N., García-Marín, M., Kunneriath, D., Mužić, K., Straubmeier, C., Valencia-S, M., and Zensus, J. A. (2011a). Near-infrared polarimetry as a tool for testing properties of accreting supermassive black holes. *MNRAS*, **413**, 322–332.

Zamaninasab, M., Witzel, G., Eckart, A., Sabha, N., Dovciak, M., Karas, V., Schödel, R., García-Marín, M., Kunneriath, D., Nishiyama, S., Straubmeier, C., Valencia-Schneider, M., and Zensus, A. (2011c). Near Infrared Polarimetry as a Tool for Testing the Properties of Radiation from Sagittarius A*. In M. R. Morris, Q. D. Wang, and F. Yuan, editors, *The Galactic Center: a Window to the Nuclear Environment of Disk Galaxies*, volume 439 of *Astronomical Society of the Pacific Conference Series*, page 323.

Lebenslauf

Persönliche Angaben

Name:	Nadeen Bassam Izzat Sabha
Anschrift:	I. Physikalisches Institut, Universität zu Köln
	Zülpicher Str. 77, 50937 Köln
Email:	sabha@ph1.uni-koeln.de
Geburtsdatum und -ort:	17.06.1981 in Amman, Jordanien
Staatsangehörigkeit:	Jordanisch

Ausbildung und Berufserfahrung

Seit Oct. 2010	Promotionstudentin an der Universität zu Köln und dem Max-Planck-Institut für Radioastronomie wiss. Betreuer: Prof. Dr. Andreas Eckart
2008 - 2010	Master der Physik an der Universität zu Köln, Köln, Deutschland wiss. Betreuer: Prof. Dr. Andreas Eckart Titel: „The Extreme Luminosity States of Sagittarius A*"
2006 - 2008	Praktikumsbetreuung an der Amman Academy High School Amman, Jordanien
2004 - 2008	Graduate studies in Physik an der University of Jordan Amman, Jordanien
1999 - 2003	Bachelor der Physik an der Jordan University of Science and Technology Irbid, Jordanien
1997 - 1999	Rosary Sisters High School Akaba, Jordanien

Stipendium und Auszeichnungen

2008- 2013	Stipendium der *Bonn-Cologne Graduate School (BCGS) of Physics and Astronomy*
2011	DAAD-Preis für hervorragende Leistungen ausländischer Studierender an Deutschen Hochschulen